Short-Pulse Laser-Plasma Interactions

A thesis submitted in partial fulfilment of the requirements
for the degree of Doctor of Philosophy by

Stuart Campbell Rae

Lincoln College, University of Oxford

Michaelmas Term 1991

Short-Pulse Laser-Plasma Interactions

A thesis submitted in partial fulfilment of the requirements
for the degree of Doctor of Philosophy by

Stuart Campbell Rae

Lincoln College, University of Oxford

Michaelmas Term 1991

Abstract

This thesis deals with several theoretical aspects of the interaction of an intense femtosecond laser pulse with a plasma. A mechanism for the enhancement of the collisional absorption of light at high intensities is described, involving the direct excitation of collective modes of the plasma, and the importance of this mechanism for a solid-density laser-produced plasma is studied under a range of conditions. An intensity-dependent collision rate is used in a numerical calculation of the reflectivity of a steep-gradient plasma, such as might be produced by an intense femtosecond laser pulse, and the conditions required to maximize absorption at high intensities are determined. The relative contributions of field-induced ionization and collisional ionization in laser-produced plasmas are studied, and it is shown that the behaviour of a gaseous plasma is almost solely governed by the field-induced process. A model is developed to simulate the propagation of an intense femtosecond laser pulse through an initially neutral gas, and this model is used to make predictions about spectral modifications to the laser pulse. Under certain conditions the spectrum is significantly broadened and suffers an overall blue shift. Quantitative fitting of theoretical spectra to experimental results in the literature is attempted, but is complicated by associated defocusing effects in the plasma. Field-induced ionization can produce a gaseous plasma which is significantly colder, for the same degree of ionization, than a plasma produced by collisional ionization. One possible application for a cold highly-ionized plasma is in a recombination x-ray laser, and the propagation model allows the calculation of the plasma temperature, which is a crucial parameter in assessing the feasibility of such schemes.

Contents

Acknowledgements

Many people have given me support, encouragement and help throughout the course of this work; I extend my thanks to all of you, including many whom space does not allow me to mention here. To Keith Burnett, who in addition to starting me off in the right direction and providing continual assistance along the way, was always ready with an endless loop of stories to lighten any occasion. To my colleagues in the lab: life wouldn't have been the same without circuit training, yoghurt tops and orange dazzler. To Alexandra, who was always puzzled by the Cat, and never received a satisfying explanation. To the Rhodes Trust, who provided my financial support at Oxford and generously granted additional funds to allow me to attend several local and international conferences. Finally, and most importantly, to my parents.

Geheimnisvoll am lichten Tag
Läßt sich Natur des Schleiers nicht berauben,
Und was sie deinem Geist nicht offenbaren mag,
Das zwingst du ihr nicht ab mit Hebeln und mit Schrauben.

Mysterious in the light of day,
Nature retains her veil, despite our clamours;
That which she doth not willingly display
Cannot be wrenched from her with levers, screws and hammers.

Goethe, *Faust*

Chapter 1

An Introduction to Femtosecond-Pulse Laser-Produced Plasmas

In the thirty years since its invention, the laser has revolutionized atomic physics. It has greatly expanded the boundaries of existing fields of research, such as spectroscopy, and in addition has led to the creation of entirely new subjects. One of these, which includes the work of the present thesis, is laser-produced plasmas: the use of intense laser light to generate ionized matter.

This thesis describes some theoretical work on the processes of light absorption in a laser-produced plasma, concentrating on the case of an intense ($\gtrsim 10^{15}$ W/cm^2) femtosecond ($\lesssim 1$ ps) laser pulse. Lasers which operate in this regime are a recent development, and there are significant differences between the plasmas produced by such lasers and those produced by their lower-intensity longer-pulse predecessors. The various chapters of this thesis focus on several different aspects of the high-intensity short-pulse interaction problem, describing the novel plasma behaviour and assessing the feasibility of some of the proposed applications.

In this chapter, the field of femtosecond-pulse laser-produced plasmas will be introduced, with several brief sections relating to laser development, applications of laser-produced plasmas and conventional absorption mechanisms, followed by an outline of the remainder of the thesis.

1.1 High-Power Femtosecond-Pulse Lasers

As a general rule, progress in laser-produced-plasma research has gone hand-in-hand with advances in high-power pulsed laser design [1, 2]. Apart from the relatively recent development of large-scale excimer lasers, high-power pulsed lasers have traditionally been solid-state systems. The first free-running ruby lasers in the early 1960s produced output energies on the order of 1 J in multiple spikes over about 1 ms. The peak laser power was at the kilowatt level and the focused intensity was in the range 10^5–10^7 W/cm^2. The invention of Q-switching, which led to stable reproducible pulses of nanosecond duration, immediately raised power levels to the megawatt level and intensities to 10^8–10^9 W/cm^2. Since that time, solid-state laser technology has gradually improved, with peak powers increasing from megawatts, through gigawatts, to terawatts. Modern large-scale solid-state laser systems use multiple amplifier stages and multiple beams to achieve enormous pulse energies. The prime example of such a system is the Nova Nd:glass laser at the Lawrence Livermore National Laboratory in the United States, which can generate 2.5 ns, 70 kJ pulses at a wavelength of 0.35 μm, providing target intensities in the range 10^{13}–10^{15} W/cm^2. Similar but less powerful facilities exist in several other countries, for example, Vulcan at the Rutherford Appleton Laboratory in the United Kingdom, Phebus at CEA Limeil in France, and Gekko at Osaka University in Japan [3].

Such large-scale laser systems represent one approach for obtaining high power: the use of the maximum possible pulse energy. However, an equivalent or greater power can be produced using a much lower pulse energy if the pulse duration is reduced. This can be achieved through mode-locking, where many cavity modes are synchronized in phase to produce an ultrashort pulse. The minimum width of such a mode-locked pulse depends on the bandwidth of the laser. In Nd:YAG the minimum pulse width is on the order of 100 ps, but in a dye laser (or more recently in Ti:sapphire) pulses shorter than 100 fs can be produced. In order to reach or exceed the peak power attainable with a large-scale solid-state laser, various techniques have been developed in recent years to generate and amplify ultrashort mode-locked pulses:

1. The pulses produced by a colliding-pulse mode-locked dye laser can be passed

through further dye amplifier stages to increase the pulse energy to the millijoule level. Pulses of 160 fs duration and 3.5 mJ energy at a wavelength of 620 nm have been produced at the University of California at Berkeley using this method, and a focused intensity of $\sim 10^{16}$ W/cm^2 has been achieved [4].

2. The output from a synchronously-pumped or distributed-feedback dye laser can be frequency multiplied or mixed to allow final amplification in an excimer laser. This approach has been used at the Max-Planck-Institute in Göttingen [5, 6, 7], the University of Tokyo [8, 9], the Los Alamos National Laboratory [10, 11] and Princeton University [12, 13]. The Japanese system has produced 390 fs, 1.5 J pulses at 248 nm, with a focused intensity of up to $\sim 10^{18}$ W/cm^2.

3. Mode-locked solid-state laser pulses can be compressed using the chirped-pulse-amplification technique. This involves propagating the initial $\sim$100 ps pulse through a length of optical fibre, which both broadens the pulse temporally and adds a frequency chirp. The stretched and chirped pulse can then be amplified in a regenerative amplifier and re-compressed using a grating pair. The extra bandwidth introduced by the chirp in the fibre allows the output pulse duration to be compressed down to $\sim$1 ps. This approach was pioneered at the University of Rochester using a Nd:YLF oscillator and Nd:glass amplifiers at 1053 nm. In the early experiments, pulse energies on the order of 1 J and intensities of up to 10^{16} W/cm^2 were produced, and the system was nicknamed the table-top terawatt laser [14, 15]. An improved system developed at the Lawrence Livermore National Laboratory can produce 800 fs, 6.8 J pulses with a peak power of 8.5 TW and a focused intensity in excess of $\sim 10^{18}$ W/cm^2 [16, 17]. A group at Limeil in France have recently used the chirped-pulse amplification technique to produce 1.2 ps pulses with an energy of 24 J [18], but the high-power record is currently held by the Institute of Laser Engineering at Osaka University, where 1 ps, 30 J pulses have been generated [19]. Chirped-pulse amplification has also been applied to systems based on Ti:sapphire, where the large gain bandwidth allows terawatt pulses to be produced at a wavelength of $\sim$800 nm and duration around 100 fs [20, 21, 22].

1.2 Applications of Laser-Produced Plasmas

When an intense laser pulse is focused on a gaseous, liquid or solid target, rapid ionization results in the formation of a plasma consisting of electrons and highly-stripped ions. This hot plasma radiates energy predominantly in the soft x-ray spectral range: distinct lines from bound transitions in the target atoms, and a continuum consisting of recombination radiation and bremsstrahlung from the free electrons. The physical conditions inside the plasma are extreme, and temperatures can approach 10^7 K ($\sim$1000 eV). Such conditions are otherwise only to be found in the centre of a star or in a nuclear explosion, and laser-produced plasmas thus present an opportunity to study these situations under laboratory conditions. In addition, laser-produced plasmas are useful test-beds for theories of the equation of state, coupling effects, and radiation transport in a high-temperature high-density system.

A major motivation for high-power laser development since the mid-1960s has been inertial confinement fusion (ICF). Here the aim is to use a spherical array of laser beams to compress and heat a small pellet containing a low-Z mixture to the point where sustained fusion reactions can occur. This can be attempted either by irradiating the pellet directly, in which case the compressive force comes from radiation pressure and as a reaction to the expansion of the plasma, or by internally irradiating a cavity around the pellet, in which case the compression comes from the huge x-ray flux produced by the plasma formed on the inside of the cavity wall. Despite considerable advances in laser technology, the break-even point for ICF has not yet been achieved, owing to a combination of factors including insufficient laser energy, non-uniform irradiation, plasma instabilities and target preheating.

Many applications of laser-produced plasmas, including high-resolution lithography and biological imaging, make use of the intense soft x-ray flux available. Recently, laser-produced plasmas have also been used in the construction of VUV and x-ray lasers [23]. Three quite different laser schemes have been proposed and demonstrated. Short-wavelength photoionization lasers are based on an inner-shell or multielectron excitation pumped by the broadband soft x-ray flux from a laser-produced plasma [24]. Collisionally-pumped x-ray lasers rely on selective electron-impact excitation during the incident laser pulse to create a population inversion in medium-Z, Ne-like or Ni-like ions [25]. Recombination x-ray lasers achieve a population inversion during the three-body recombination cascade following the laser pulse, in low-Z, H-like or Li-like ions [26]. There is particular interest in developing an x-ray laser which would operate efficiently in the so-called water window, from 2.2–4.4 nm. In this wavelength range, between the absorption K edges of carbon and oxygen, biological samples have a high contrast ratio against an aqueous background, and a short laser pulse would allow an image of a living sample to be recorded before significant damage could occur. Both of these points are important for the development of a practical x-ray microscope.

Plasmas produced by intense femtosecond laser pulses offer new possibilities and also a chance to improve on many of the existing applications, with the notable exception of ICF, for which a long laser pulse appears to remain a necessity. From a fundamental viewpoint, the lack of significant hydrodynamic motion during a femtosecond pulse may allow interactions in a hot, solid-density plasma to be studied directly, without the shielding effect of a long-scale-length underdense region. Extreme intensities can be achieved, allowing the testing of various theoretical models which attempt to describe the interaction of matter with intense radiation. X-ray pulses as short as $\sim$1 ps can be generated, and such an x-ray source could have a range of uses in ultrafast spectroscopy [27]. By focusing a pulse in a gas or liquid target at slightly lower intensity, a femtosecond white-light continuum source can be obtained, and this also has important spectroscopic applications [28]. Finally, shorter and more intense laser pulses may lead to the development of recombination x-ray lasers which are both more efficient and able to operate at shorter wavelengths than those so far constructed [29].

1.3 Absorption of Laser Light

The mechanisms which couple laser light into a plasma are of fundamental importance in determining the plasma conditions. Extensive reviews of the laser-plasma interaction problem can be found in Refs. [1], [2], [30] and [31].

A schematic picture of a typical solid-density laser-produced plasma is shown in Fig. 1.1. This consists basically of a solid-density region, an ablation front and a long-scale-length expansion region. Within the expansion region is the critical-density surface, at which the laser frequency equals the plasma frequency. The laser light cannot propagate beyond the critical-density surface and will be reflected at this point, but an evanescent field will penetrate a short distance, the skin depth, into the overdense plasma.

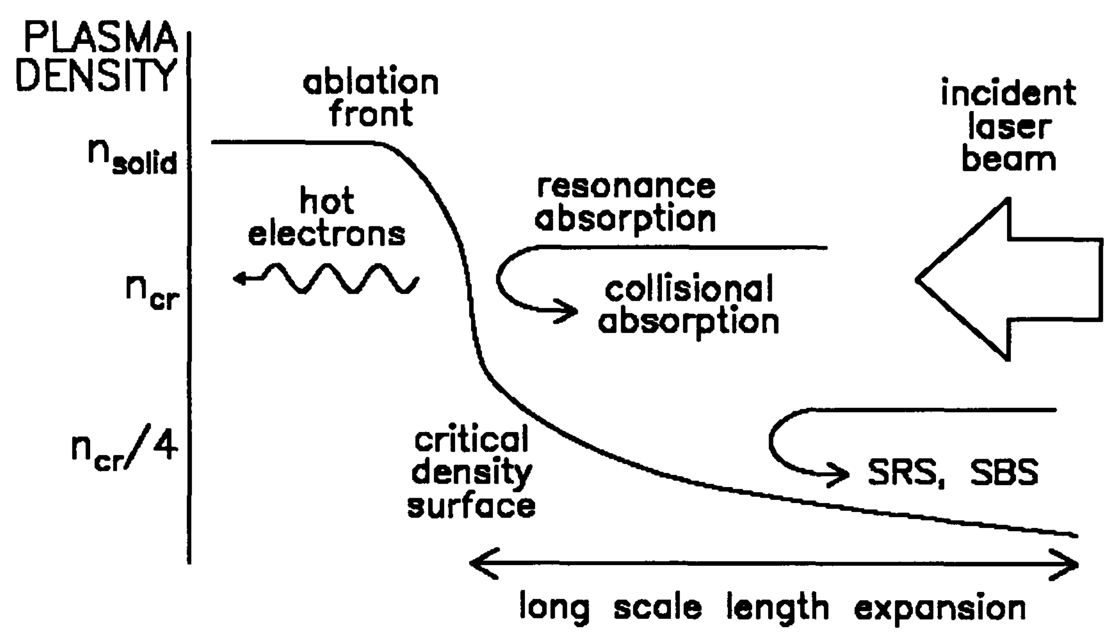

Figure 1.1: Schematic picture of a typical plasma produced by an intense laser pulse focused on a solid target.

Various mechanisms act to couple the light energy into the plasma. The most important of these is collisional or inverse bremsstrahlung absorption, which can occur everywhere within the underdense plasma and within the skin depth. In addition, if there is a component of the laser electric field parallel to the plasma density gradient, the field can excite plasma waves at the critical density surface, leading to resonance absorption and the production of hot electrons. Around the critical density surface, the radiation pressure and forces due to the intensity gradient can act to locally steepen the density profile. Farther out in the underdense plasma, beyond the quarter-density surface, parametric processes such as stimulated Raman scattering (SRS) and two-plasmon decay can occur. Other parametric processes, such as stimulated Brillouin scattering (SBS), can occur throughout the underdense region.

The major difference between plasmas produced by relatively long laser pulses (for example, ICF plasmas) and those produced by femtosecond pulses is the size of the expansion region. A nanosecond laser pulse may generate a density gradient scale length of some hundreds of laser wavelengths, but a femtosecond pulse results in a scale length on the order of a wavelength or less. Parametric processes exhibit an intensity threshold which typically varies inversely with the scale length, and as the density gradient becomes steeper these processes become less important. For scale lengths less than a laser wavelength, the absorption is dominated by collisional and resonance absorption. Femtosecond-pulse lasers may also reach intensities at which modifications to the standard absorption mechanisms need to be considered. Such modifications include the effect of the quiver motion on the electron velocity distribution, collective plasma excitations and field-induced ionization. These points will all be addressed in later chapters of this thesis.

1.4 Thesis Outline

The work included in this thesis deals almost exclusively with laser light absorption in plasmas, and no attempt is made at more complete plasma modelling. Thus, topics such as the equation of state, hydrodynamic motion, x-ray production and radiation transport are mentioned only briefly, if at all. Several extremely detailed computer codes have been developed which attempt a complete plasma simulation, for example, LASNEX at the Lawrence Livermore National Laboratory in the United States and MEDUSA at the Rutherford Appleton Laboratory in the United Kingdom. One of the aims of this thesis is to investigate the modifications which might be needed to such codes, were they to be applied to plasmas produced by the new generation of intense femtosecond-pulse lasers.

The thesis is divided into seven chapters:

Chapter 2 discusses the calculation of the electron-ion collision frequency and collisional absorption. Two high-intensity corrections to the standard expression are described, one due to a modification of the electron velocity distribution, and one arising from the excitation of collective plasma oscillations.

Chapter 3 uses an intensity-dependent electron-ion collision frequency in a static-profile reflectivity model to investigate the effect of collision-rate modifications on laser light absorption in a realistic plasma.

Chapter 4 introduces field-induced ionization, describes several theoretical models in the literature and compares field-induced ionization rates with collisional ionization rates, in order to determine the conditions under which the field-induced process will be important.

Chapter 5 outlines a propagation model which couples field-induced ionization to Maxwell's equations. Calculations of spectral shifts and broadening of an intense femtosecond laser pulse propagating through an atmospheric-density gas are presented. These are compared with experimental results in the literature, and with the predictions of simpler models which have previously been used in the analysis of experiments.

Chapter 6 uses the propagation-ionization model to investigate the properties of the plasma formed by the passage of an intense femtosecond laser pulse through an atmospheric-density gas. These plasmas have been proposed as potential candidates for recombination x-ray lasers, and the model provides a quantitative prediction of the plasma temperature, which is a crucial parameter in assessing the feasibility of any such scheme.

Chapter 7 forms a conclusion to the thesis, and includes a summary of the main results from earlier chapters and suggestions for future work.

Chapter 2

High-Intensity Modifications to Collisional Absorption

Inverse bremsstrahlung (collisional absorption) is often the dominant heating mechanism in laser-produced plasmas. In this chapter, the conventional methods for calculating absorption by this mechanism will be discussed in some detail, and two modifications which occur at high laser intensities will be addressed. The first of these is a result of the electron quiver motion altering the velocity distribution, leading to a reduction in the absorption rate. This so-called nonlinear inverse bremsstrahlung has been a topic of extensive investigation for many years. The second modification involves the direct excitation of plasma oscillations by the electron quiver motion, which in certain cases can lead to an increase in the absorption rate. This work is the subject of a recent publication by Rae and Burnett [32].

2.1 Standard Collisional Absorption

Consider a linearly-polarized plane-wave laser field, $E = E_0 \exp(i\omega_0 t)$. The equation of motion for a free electron in this field is

$$\frac{dv}{dt} + \nu_{ei} v = -\frac{eE}{m_e} , \tag{2.1}$$

where v is the electron velocity and ν_{ei} is an effective collision frequency, assumed here to be velocity-independent. This equation can be solved to give the plasma current,

$$J = -n_e e v = \frac{n_e e^2}{m_e} \frac{i\omega_0 - \nu_{ei}}{\omega_0^2 + \nu_{ei}^2} E \, . \tag{2.2}$$

The collisional absorption rate per unit volume, assuming $\nu_{ei} \ll \omega_0$, is then given by

$$\frac{1}{2}\mathrm{Re}\{J \cdot E^*\} = 2\,\mathcal{E}_q\,\nu_{ei}\,n_e \ , \tag{2.3}$$

where $\mathcal{E}_q$ is the average quiver energy,

$$\mathcal{E}_q = \frac{e^2 E_0^2}{4 m_e \omega_0^2} \ . \tag{2.4}$$

In this simple case, the absorption rate is proportional to the product of the collision frequency and the laser intensity. The collision frequency has been introduced here as a phenomenological parameter, but there are various methods by which it can be calculated explicitly, depending on the plasma conditions.

At very low temperatures, the electrons in the plasma obey Fermi-Dirac statistics. The Fermi energy is given by $\mathcal{E}_F = (\hbar^2/2m_e)(3\pi^2 n_e)^{2/3}$, where n_e is the electron density, and the average kinetic energy is approximately $\frac{3}{5}\mathcal{E}_F$. The plasma is said to be highly-degenerate when $\frac{3}{2}k_B T_e \ll \frac{3}{5}\mathcal{E}_F$, and non-degenerate (or classical) when $\frac{3}{2}k_B T_e \gg \frac{3}{5}\mathcal{E}_F$. Here T_e is the electron temperature and k_B is Boltzmann's constant. Strong-coupling effects may also be important in the plasma if the Coulomb interaction energy per electron is greater than the kinetic energy. The Coulomb energy may be estimated as $\mathcal{E}_C = e^2/4\pi\epsilon_0 a$, where $a = (3/4\pi n_e)^{1/3}$ is the electron-sphere radius. The plasma is said to be strongly-coupled if $\mathcal{E}_C \gg \frac{3}{2}k_B T_e$ and weakly-coupled if $\mathcal{E}_C \ll \frac{3}{2}k_B T_e$. The approximate boundaries between these various regimes (classical and degenerate statistics, strong and weak coupling) are shown in Fig. 2.1. For reference, the atomic density in an ideal gas at 1 atm pressure is 2.5×10^{19} cm^{-3}, and the carbon atom density in a low-density CH_2 plastic is 4×10^{22} cm^{-3}. The classical weakly-coupled regime is the easiest to treat theoretically, and plasma models often assume a minimum temperature which is above the degenerate and strongly-coupled boundaries.

In the classical weakly-coupled regime, assuming a Maxwellian velocity distri-

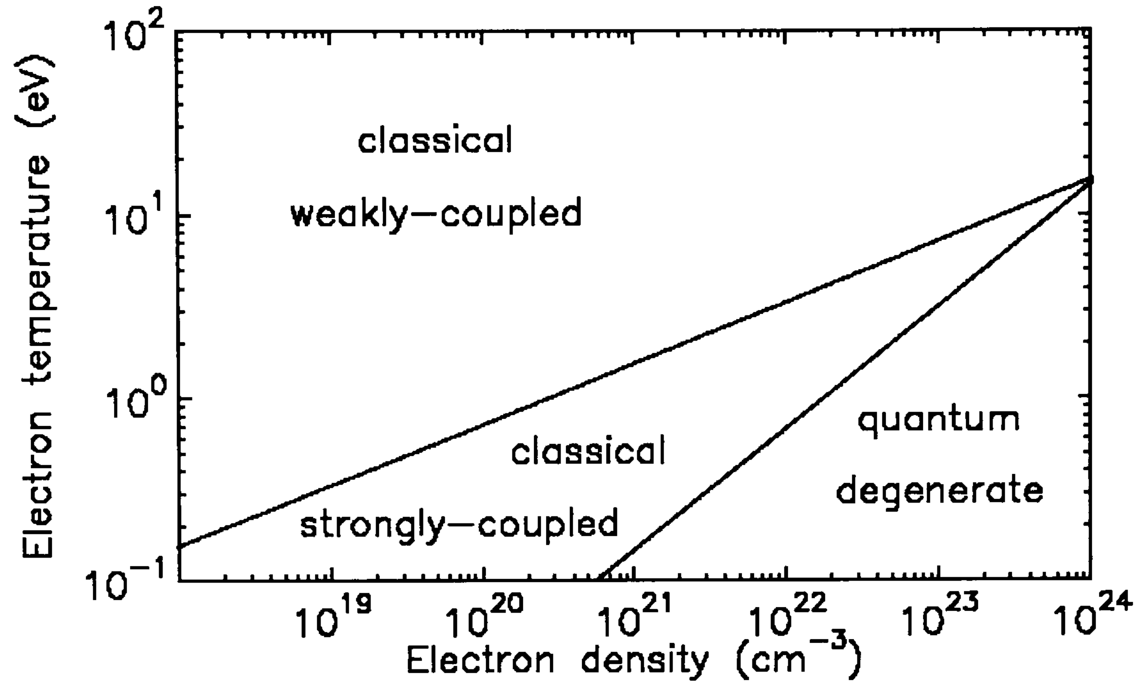

Figure 2.1: Plasma characteristics as a function of temperature and density, showing the approximate boundaries between strong and weak coupling, and between degenerate and classical statistics.

bution, the electron-ion collision frequency is given by the Spitzer expression [33, 34],

$$\nu_{ei} = \frac{4\sqrt{2\pi}}{3} \frac{Z n_e e^4 \ln \Lambda}{(4\pi\epsilon_0)^2 m_e^{1/2} (k_B T_e)^{3/2}} \; . \tag{2.5}$$

Here Z is the degree of ionization and $\ln \Lambda$ is the Coulomb logarithm, defined by

$$\ln \Lambda = \ln \left(\frac{r_{max}}{r_{min}} \right) \; , \tag{2.6}$$

where r_{max} and r_{min} are the maximum and minimum impact parameters, respectively. The maximum impact parameter is approximately given by the Debye wavelength,

$$r_{max} \simeq \lambda_D = \left(\frac{\epsilon_0 k_B T_e}{n_e e^2} \right)^{1/2} \; , \tag{2.7}$$

and the minimum impact parameter is given by the larger of the classical distance of closest approach and the de Broglie wavelength of the electron,

$$r_{min} = \max \left\{ \frac{Ze^2}{4\pi\epsilon_0 m_e v^2} \, , \, \frac{\hbar}{2m_e v} \right\} \, . \tag{2.8}$$

For a Maxwellian distribution, the electron velocity can be taken as the root-mean-square thermal velocity,

$$v = \left(\frac{3k_B T_e}{m_e} \right)^{1/2} \, . \tag{2.9}$$

The collision frequency in Eq. (2.5) is obtained from a model in which the momentum changes from electron-ion encounters are averaged over all possible impact parameters, and the time taken for a test particle to be deflected by 90° is determined. The collision frequency is defined as the inverse of this right-angle deflection time.

A very similar result for the collision frequency can be obtained by two quite different and more rigorous methods. The first involves solving the Fokker-Planck equation for the rate of change of the electron distribution function [30]. This solution is substituted into the kinetic equation to find the current density, and the resulting rate of energy dissipation is related to an effective collision frequency using Eq. (2.3). The only difference between the collision rate determined in this way and from the Spitzer expression is in the Coulomb logarithm. In the Fokker-Planck solution, the maximum impact parameter is given by

$$r_{max} = \frac{v_{th}}{\omega_0} \, , \tag{2.10}$$

instead of Eq. (2.7).

The most rigorous method starts with a classical calculation of the power spectrum emitted by an electron undergoing Coulomb scattering [1]. Using the spectral emission coefficient and Kirchhoff's law, which relates absorption and emission, the absorption coefficient and hence the effective collision frequency can be determined. In this case, a so-called Gaunt factor takes the place of the Coulomb logarithm. In the classical limit, the average Gaunt factor for a Maxwellian distribution is almost (apart from a small factor of order unity inside the logarithm) the same as the Coulomb logarithm in the Spitzer expression, except that the maximum impact parameter is again specified by Eq. (2.10) instead of Eq. (2.7).

The Spitzer formula is only valid in the weakly-coupled regime, and its approximations break down as $\ln \Lambda$ approaches zero [35]. At solid densities and temperatures of $\lesssim 10$ eV, the Spitzer formula can be incorrect by as much as a factor of ten. The additional effects of ion correlations, as well as various quantum mechanical and relativistic corrections, have been extensively investigated [1], but in many cases the basic Spitzer formula gives results which approximately agree with considerably more detailed numerical calculations.

2.2 Effect of the Quiver Motion

The most significant correction to the Spitzer formula as far as high-intensity laser experiments are concerned involves the effect of the electron quiver motion on the velocity distribution function.

A laser intensity I corresponds to an electric field of amplitude E_0, where

$$E_0 = \left(\frac{2I}{\epsilon_0 c}\right)^{1/2} , \tag{2.11}$$

and the maximum quiver velocity of a free electron in this field is given by

$$v_q = \frac{eE_0}{m_e \omega_0} . \tag{2.12}$$

Defining a characteristic thermal velocity as

$$v_{th} = \left(\frac{k_B T_e}{m_e}\right)^{1/2} , \tag{2.13}$$

the ratio v_q/v_{th} can be used as a measure of the laser field strength. For $v_q/v_{th} \ll 1$, the Spitzer expression is valid, but for $v_q/v_{th} \gtrsim 1$, the velocity distribution is severely affected and a correction to the standard expression is required. Many authors have addressed the problem of nonlinear collisional absorption, including Rand [36], Silin [37], Bunkin and Fedorov [38], Pert [39], Schlessinger and Wright [40] and Jones and

Lee [41]. All agree on the basic form of the expression in the strong-field limit, but differ in numerical constants and the specific form of the Coulomb logarithm.

From Eq. (2.3), it can be seen that the rate of energy absorption in an element of plasma is proportional to the product of the collision frequency and the laser intensity. In the strong-field limit, the collision rate decreases as $I^{-3/2}$, so the total power dissipation decreases as $I^{-1/2}$. In the weak-field limit, the collision rate is independent of intensity, and the power dissipation increases linearly with I. The intensity where $v_{th} = v_q$ is approximately the optimum intensity for collisional absorption. This intensity is given by

$$I_{opt} = \frac{m_e k_B T_e \omega_0^2 \epsilon_0 c}{2e^2} = 1.1 \times 10^{15} \left(\frac{k_B T_e}{200 \text{ eV}}\right) \left(\frac{500 \text{ nm}}{\lambda_0}\right)^2 \text{ W/cm}^2 . \tag{2.14}$$

In the intermediate regime, where the thermal and quiver velocities are comparable, the problem is considerably more difficult, and analytical solutions are in general unobtainable. An approximate correction factor for the Spitzer expression in this intermediate regime, discussed by Schlessinger and Wright [40], is given by

$$F = \left(1 + \left\langle v_q^2 \right\rangle / 3 v_{th}^2\right)^{-3/2} . \tag{2.15}$$

When compared with more detailed calculations, this simple correction is found to be reasonably accurate over a wide range of parameter space. In a collisional plasma, the average quiver velocity can be determined by treating the electron motion as a damped, driven oscillator. This gives

$$\left\langle v_q^2 \right\rangle = \frac{e^2 E_0^2}{2 m_e^2 (\omega_0^2 + \nu_{ei}^2)} . \tag{2.16}$$

As this expression includes a dependence on the collision frequency, Eqs. (2.5), (2.15) and (2.16) must be solved iteratively to obtain a solution.

The derivation of Eq. (2.15) assumes that the electrons can be described by a Maxwellian velocity distribution which is oscillating in the laser field. Langdon [42] has shown that in some cases the electron-electron collision frequency is not sufficiently rapid to maintain a true Maxwellian background, and modifications to this distribution can further reduce the absorption rate. Defining a parameter $\alpha = Zv_q^2/v_{th}^2$, the absorption rate is found to be reduced by a factor

$$F = 1 - \frac{0.553}{1 + (0.27/\alpha)^{0.75}} , \tag{2.17}$$

for α in the range $1 \lesssim \alpha \ll Z$. At intensities for which $v_q \simeq v_{th}$, and for $Z \gg 1$, the additional reduction can be as much as $\sim$50%.

The existence of an optimum intensity for coupling laser light into a plasma through collisions poses a serious problem. In an attempt to achieve higher plasma temperatures, lasers with shorter pulses and higher intensities are being used, but beyond the optimum intensity the volume absorption rate actually decreases. Eventually, it is more efficient to distribute the same laser energy over a larger focal spot, rather than using the maximum possible target intensity. However, the effect of an intensity-dependent collision rate on the reflectivity of a plasma with a realistic density profile is not immediately obvious, since it depends on the rate of attenuation of the laser field inside the plasma. This will be investigated more fully in Chapter 3, where a nonlinear reflectivity model will be developed.

2.3 Collective Plasma Effects

It has been suggested recently by Mulser *et al.* [43] that the rate of collisional absorption in a solid-density laser-produced plasma might be augmented at high intensities by a collective contribution, arising from the excitation of plasma waves by the oscillating electrons. In order to show how such a collective effect might arise, it is necessary to consider the dielectric response of the plasma explicitly. A basic stopping-power model will be briefly reviewed, and then a more detailed calculation will be described.

2.3.1 Stopping-Power Model

Initially, it is instructive to use a stopping-power model, in which an ion moves with a straight-line velocity v_0 through a background of thermal electrons. This is equivalent (through a change in reference frame) to a situation in which the electrons move through a stationary background of ions, but it is a simpler situation to analyse, as the thermal and quiver velocities are separated.

In this model, the moving charge generates a wake field in the plasma, and the interaction of this wake field with the moving charge leads to a rate of energy loss given by [44]

$$\frac{dW}{dt} = \frac{q_0^2}{\pi v_0} \int \frac{dk}{k} \int_{-kv_0}^{kv_0} d\omega \; \omega \; \mathrm{Im}\left\{\epsilon(k,\omega)\right\}^{-1} \; , \tag{2.18}$$

where q_0 is the charge and $\epsilon(k,\omega)$ is the dielectric response function. The integrand in Eq. (2.18) is proportional to the density-fluctuation spectrum in the plasma. In the limit $k \gg k_D$, where $k_D = 1/\lambda_D$ is the Debye wavenumber, the spectrum is Maxwellian, representing thermal fluctuations. In the limit $k \ll k_D$, the spectrum is dominated by peaks at $\omega = \pm\omega_p$ representing the excitation of collective modes in the plasma. Here ω_p is the plasma frequency, given by

$$\omega_p = \left(\frac{n_e e^2}{\epsilon_0 m_e}\right)^{1/2} \; . \tag{2.19}$$

The k-integration can thus be conveniently split into two parts, and using the approximate forms of the dielectric response function in each case leads to two terms: an individual-particle term for $k \gg k_D$,

$$\left(\frac{dW}{dt}\right)_{ind} = \frac{q_0^2 \omega_p^2}{v_0} \ln\left(\frac{k_{max}}{k_D}\right) \; , \tag{2.20}$$

and a collective term for $k \ll k_D$,

$$\left(\frac{dW}{dt}\right)_{coll} = \frac{q_0^2 \omega_p^2}{v_0} \ln\left(\frac{k_D}{\omega_p/v_0}\right) \; . \tag{2.21}$$

The first term corresponds to the Spitzer expression evaluated for $v_0 \gg v_{th}$, and a comparison of the two terms suggests that a simple correction to the Coulomb logarithm may be sufficient to include the collective effects. If the Coulomb logarithm were written

$$\ln \Lambda = \ln \left(\frac{k_{max}}{\omega_p / v_0} \right) , \tag{2.22}$$

then both contributions should be included. This form of the Coulomb logarithm (which is essentially the one obtained by Mulser *et al.*), with v_0 replaced by the average quiver velocity, v_q, will be used together with an intensity-corrected Spitzer expression in a later section to compare with results from the detailed model to be outlined below.

2.3.2 Detailed Model for Collective Response

A detailed model for the collective component of absorption will now be outlined, using the correct oscillatory motion for the electrons and the full version of the dielectric response function. As in the straight-line stopping-power model, a frame of reference is used in which the electrons have only their random thermal motion, and the oscillatory motion of the linearly-polarized laser field is transferred to the ions. This follows the method of Rand [36] and Jones and Lee [41]. In this reference frame, the charge distribution due to an oscillating ion is

$$\rho(\mathbf{r}, t) = Ze\, \delta(\mathbf{r} + \mathbf{r}_q \cos \omega_0 t) \ . \tag{2.23}$$

Here Z is the degree of ionization, ω_0 is the laser angular frequency and $\mathbf{r}_q$ is the quiver amplitude, given by

$$\mathbf{r}_q = \frac{e\mathbf{E_0}}{m_e \omega_0^2} , \tag{2.24}$$

where $\mathbf{E_0}$ is the laser electric field. The Fourier transform of Eq. (2.23) in space and time is

$$\rho(\mathbf{k}, \omega) = \sum_{n=-\infty}^{\infty} 2\pi\, Ze\, \delta(\omega - n\omega_0)\, i^n\, J_n(\mathbf{k} \cdot \mathbf{r}_q) , \tag{2.25}$$

where $J_n(x)$ is an ordinary Bessel function of order n.

Using Poisson's equation, the potential due to this charge source is found to be

$$\begin{aligned}\Phi(\mathbf{r},t) &= -\int\int \frac{d^3k}{(2\pi)^3}\frac{d\omega}{2\pi}\frac{4\pi e}{k^2}\frac{1}{\epsilon(\mathbf{k},\omega)}\,\rho(\mathbf{k},\omega)\exp(-i\mathbf{k}\cdot\mathbf{r}-i\omega t) \\ &= -\int \frac{d^3k}{(2\pi)^3}\frac{4\pi Ze^2}{k^2}\sum_{n=-\infty}^{\infty}\frac{i^n J_n(\mathbf{k}\cdot\mathbf{r}_q)}{\epsilon(\mathbf{k},n\omega_0)}\exp(-i\mathbf{k}\cdot\mathbf{r}-in\omega_0 t)\ , \quad (2.26)\end{aligned}$$

where $\epsilon(\mathbf{k},\omega)$ is the longitudinal dielectric response function for the plasma [44], which will be defined in detail below.

The force on the ion due to this potential is

$$\begin{aligned}\mathbf{F}(t) &= \mathrm{Re}\{-Z\ \nabla\Phi(\mathbf{r},t)\} \\ &= \mathrm{Im}\int \frac{Z^2e^2\mathbf{k}\ d^3k}{2\pi^2}\sum_{n,m}\frac{J_n(\mathbf{k}\cdot\mathbf{r}_q)J_m(\mathbf{k}\cdot\mathbf{r}_q)i^{n-m}\exp\{i(m-n)\omega_0 t\}}{k^2\epsilon(\mathbf{k},n\omega_0)} \quad (2.27)\end{aligned}$$

and the power absorption per unit volume is given by

$$\frac{dW}{dt} = n_i\Big\langle \mathbf{F}(t)\cdot\mathbf{v}_q\sin\omega_0 t\Big\rangle_{cycle}\ , \quad (2.28)$$

where n_i is the ion density. Substituting for $\mathbf{F}(t)$ from Eq. (2.27) gives

$$\frac{dW}{dt} = \frac{Zn_e e^2\omega_0}{\pi^2}\int\frac{d^3k}{k^2}\sum_{n=1}^{\infty}\mathrm{Im}\left\{\frac{1}{\epsilon(\mathbf{k},n\omega_0)}\right\}nJ_n^2(\mathbf{k}\cdot\mathbf{r}_q)\ . \quad (2.29)$$

Using polar coordinates, where $\mathbf{k}\cdot\mathbf{r}_q = kr_q\cos\theta$ and $d^3k = k^2\sin\theta\ dk\ d\theta\ d\varphi$, and assuming that $\epsilon(\mathbf{k},n\omega_0)$ is isotropic, the power absorption may be written in the form

$$\frac{dW}{dt} = \frac{4Zn_e e^2\omega_0}{(4\pi\epsilon_0)\pi r_q}\int_0^{k_{max}}\frac{dk}{k}\sum_{n=1}^{\infty}\mathrm{Im}\left\{\frac{1}{\epsilon(k,n\omega_0)}\right\}\int_0^{kr_q}nJ_n^2(x)\ dx\ . \quad (2.30)$$

In the low-field limit only the individual-particle effects, with $k \gg k_D$, are of importance, and the first term of the summation is dominant. In this case,

$$\sum_{n=1}^{\infty} \mathrm{Im}\left\{\frac{1}{\epsilon(k, n\omega_0)}\right\} \int_0^{kr_q} nJ_n^2(x)\, dx \simeq \mathrm{Im}\left\{\frac{1}{\epsilon(k,\omega_0)}\right\} \int_0^{kr_q} J_1^2(x)\, dx$$
$$\simeq \mathrm{Im}\left\{\frac{1}{\epsilon(k,\omega_0)}\right\} \frac{1}{12}(kr_q)^3 . \qquad (2.31)$$

Taking the classical Maxwellian plasma dispersion function for $k \gg k_D$ [44],

$$\mathrm{Im}\left\{\frac{1}{\epsilon(k,\omega_0)}\right\} = -\left(\frac{\pi}{2}\right)^{1/2} \frac{\omega_0 k_D^2}{k^3 (k_B T_e/m_e)^{1/2}} \exp\left(\frac{-\omega_0^2}{2k^2(k_B T_e/m_e)}\right) , \qquad (2.32)$$

and converting the power absorption rate into an effective electron-ion collision frequency leads to

$$\nu_{ei} \simeq \frac{4\sqrt{2\pi}}{3} \frac{Z n_e e^4}{(4\pi\epsilon_0)^2 m_e^{1/2} (k_B T_e)^{3/2}} \int_{k_D}^{k_{max}} \frac{dk}{k} \exp\left(-\frac{1}{2}\frac{\omega_0^2}{\omega_p^2}\frac{k_D^2}{k^2}\right)$$
$$\simeq \frac{4\sqrt{2\pi}}{3} \frac{Z n_e e^4}{(4\pi\epsilon_0)^2 m_e^{1/2} (k_B T_e)^{3/2}} \ln\left(\frac{k_{max}}{k_D}\right) , \qquad (2.33)$$

which is the standard Spitzer expression.

In order to calculate absorption from the full expression in Eq. (2.30), an analytic form for the dielectric response function in the plasma must be found. The general form of the classical collisionless dielectric response function is [44]

$$\epsilon^0(\mathbf{k},\omega) = 1 - \frac{\omega^2}{k^2} \int d^3v \, \frac{\mathbf{k}\cdot\{\partial f_e(\mathbf{v})/\partial \mathbf{v}\}}{\mathbf{k}\cdot\mathbf{v} - \omega - i\eta} . \qquad (2.34)$$

Using an isotropic Maxwellian velocity distribution, this becomes

$$\epsilon^0(k,\omega) = 1 + \frac{k_D^2}{k^2}\, \xi\left(\frac{\omega}{k\,(k_B T_e/m_e)^{1/2}}\right) , \qquad (2.35)$$

where $\xi(x)$ is defined by

$$\xi(x) = ix \left(\frac{\pi}{2}\right)^{1/2} \exp\left(\frac{-x^2}{2}\right) - 2\exp\left(\frac{-x^2}{2}\right) \int_0^{x/\sqrt{2}} \exp(t^2)\, dt \; . \tag{2.36}$$

This function can be written in terms of the plasma dispersion function, $Z(y)$, as

$$\xi(x) = 1 + \frac{x}{\sqrt{2}}\, Z\left(\frac{x}{\sqrt{2}}\right) \; . \tag{2.37}$$

The plasma dispersion function has been described in detail by Fried and Conte [45]. It can be calculated using a repeated fraction or by solving a characteristic differential equation, and there are also power series and asymptotic expansions for use in the appropriate limits.

As it stands, Eq. (2.35) is incomplete, because no account is taken of electron-ion collisions. It is, however, essential to include the collisional damping of plasmons in the calculation of absorption by the collective modes. The collisionless dielectric function predicts a plasmon width due to Landau damping alone, which will vanish as k approaches zero, a region critical to the collective response. Simply replacing ω by $\omega + i\nu$, where ν is a collision frequency, is known to be incorrect. This would imply that collisions relax the distribution function to global equilibrium rather than the proper local equilibrium, and would violate the conservation of local number density and hence upset the sum rules on the response function. As the collective contribution relies on the validity of the sum rules, it is necessary to incorporate the collisions in a consistent manner. Mermin [46] has shown that collisions can be included in a way that ensures local conservation of particles. The required form of the dielectric response function is

$$\epsilon(k,\omega) = 1 + \frac{(1 + i\nu_{ei}/\omega)\{\epsilon^0(k,\omega + i\nu_{ei}) - 1\}}{1 + (i\nu_{ei}/\omega)(\epsilon^0(k,\omega + i\nu_{ei}) - 1)/(\epsilon^0(k,0) - 1)} \; . \tag{2.38}$$

The electron-ion collision frequency, ν_{ei}, can be calculated using the Spitzer expression together with an intensity-dependent correction.

Up to this point in the derivation, a number of assumptions and approximations have been made. These will be summarized here, before proceeding with some results from the calculations:

1. The electron motion is non-relativistic, $v_q \ll c$. This puts an upper limit on the laser intensity,

$$I \ll \frac{\epsilon_0 c^3 m_e^2 \omega_0^2}{2e^2} = 5.5 \times 10^{18} \left(\frac{500 \text{ nm}}{\lambda_0}\right)^2 \text{ W/cm}^2 . \tag{2.39}$$

2. Collisions are instantaneous, that is, the collision duration is negligible compared with $(1/\omega_p)$. If the collision duration were not negligible, a high-frequency roll-off would need to be included in the dielectric response function. This topic has been discussed by Utsumi and Ichimaru [47].

3. The collision frequency is less than the plasma frequency, $\nu_{ei} < \omega_p$. If this condition does not hold, then the ion motion will not be sinusoidal as given by Eq. (2.23), and plasmons will not exist as genuine excitations. The ratio (ν_{ei}/ω_p) scales approximately as

$$\frac{\nu_{ei}}{\omega_p} \propto \frac{Zn_e/(k_B T_e)^{3/2}}{n_e^{1/2}} = \frac{Zn_e^{1/2}}{(k_B T_e)^{3/2}} . \tag{2.40}$$

   Thus, in high-Z targets plasmons can only exist at very high temperatures (or at very low temperatures, where classical statistics do not apply and plasmons are somewhat different in nature).

4. The electron temperature is sufficiently high that the electrons obey classical statistics and the plasma is weakly-coupled. For the solid-density plasmas considered here, this condition is approximately $k_B T_e \gtrsim 100$ eV.

5. Ion thermal motion is negligible. This will be the case if the movement of an ion during a plasmon lifetime is small compared with the wavelength of the excitation,

$$\frac{(v_{th})_{ion}}{\nu_{ei}} \ll \frac{1}{k} . \tag{2.41}$$

   As the maximum value of k is the Debye wavenumber, k_D, this requirement amounts to

$$\frac{k_D\,(v_{th})_{ion}}{\nu_{ei}} = \frac{\omega_p}{\nu_{ei}} \left(\frac{m_e}{m_i}\frac{T_i}{T_e}\right)^{1/2} \ll 1 . \tag{2.42}$$

The equilibration of electron and ion temperatures in a plasma takes on the order of $(1/Z)(m_i/m_e)$ times longer than the electron-electron thermalization time, so there is usually a large imbalance between the electron and ion temperatures [48]. This, together with the electron-ion mass ratio, ensures that the inequality will be satisfied in the solid-density plasmas considered and ion motion effects may be safely neglected.

6. The electron distribution function is isotropic and Maxwellian. Langdon [42] has shown that modifications to the distribution function can, under certain conditions, reduce the inverse bremsstrahlung absorption rate by up to ~50%. However, this may have a smaller effect on the collective contribution, because for low-k interactions the dielectric response function is less sensitive to the form of the distribution. In the extreme limit as k approaches zero, the dielectric response function is given by $\epsilon(0, \omega) = 1 - \omega_p^2/\omega^2$, and depends only on the electron density.

2.3.3 Results of the Calculation

A computer program written in FORTRAN 77 was used to numerically integrate Eq. (2.30) for the collective absorption rate, using Romberg's method [49]. As the emphasis here is on the additional absorption due to collective effects, the k-integral was only evaluated over the range $0 < k < k_D$. For a typical set of parameters, a few minutes of CPU time on a VAX 7800 processor was required.

The number of terms which need to be included in the summation over Bessel functions depends on the laser intensity. At very low intensities only the $n = 1$ term is significant, but at high intensities terms up to the order of $n_{max} \simeq 3\omega_p/\omega_0$ are required to obtain reasonable convergence. For solid-density aluminium and 248 nm light, $n_{max} \simeq 15$. For high-Z targets, or long-wavelength laser light, the number of terms required (and hence the computing time) increases.

The results are plotted as a rate of energy absorption, not as an effective electron-ion collision frequency, because the former is the more fundamental quantity. The data shown also refer to a solid-density plasma, which is overdense for the laser radiation ($\omega_p > \omega_0$). This may seem strange, given that radiation cannot propagate in an overdense plasma, but it must be remembered that in a femtosecond-pulse plasma the density gradient will be extremely steep, and in this case the properties of the plasma in the evanescent (overdense) region can have a significant effect on the overall reflectivity.

Figure 2.2 shows the collective component of absorption plotted as a function of laser intensity, for a laser wavelength of 248 nm and a solid-density lithium target at a temperature of 250 eV. The dotted curves denote the contributions from each of the first ten terms in the summation and the solid line marks the total. Each term only appears to turn on beyond an associated threshold intensity. At very low intensities, as expected, only the $n = 1$ term is significant, but at intensities for which $v_q \gg v_{th}$, a higher term (in this case, $n = 3$) dominates the absorption. The value of n which dominates at high intensity is the one which most closely matches the condition $n\omega_0 = \omega_p$.

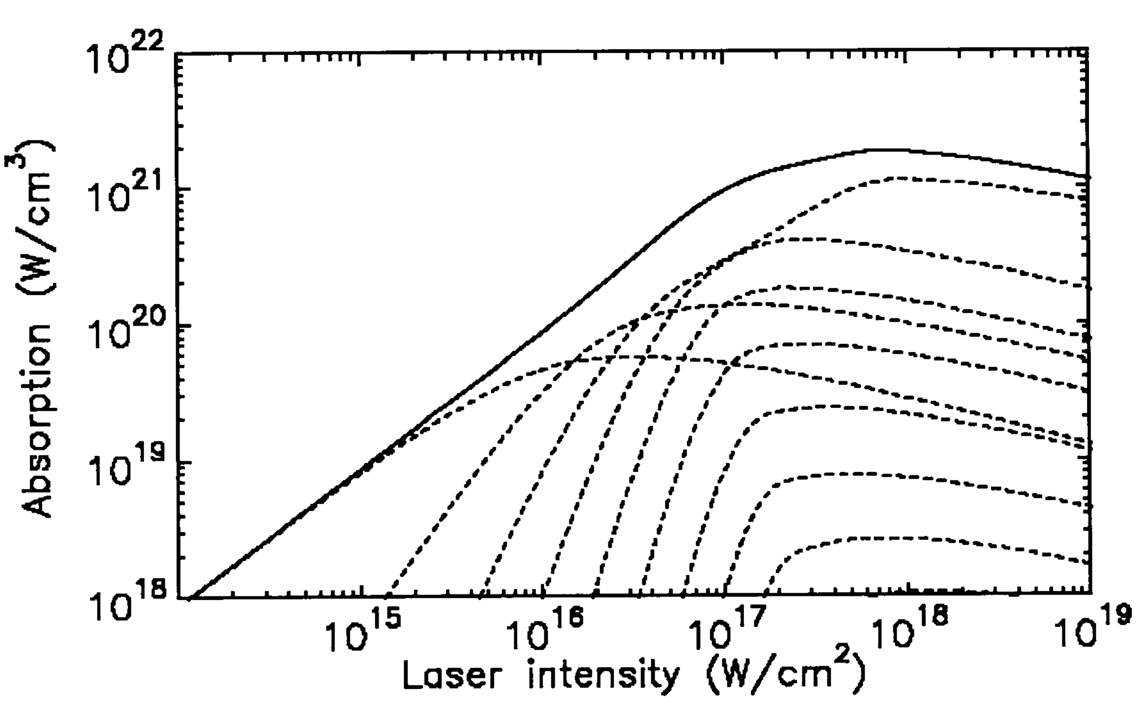

Figure 2.2: The collective component of absorption calculated for solid-density, fully-ionized lithium. The contributions from the first ten terms of the summation are shown as dotted lines, and the total as a solid curve.

For different values of the electron temperature, T_e, or the degree of ionization, Z, the basic behaviour remains the same. A higher value for Z leads to a larger ω_p, and means that more terms must be included in the summation. In this case, the separation between the individual contributions is reduced. A higher value for T_e increases the separation and shifts the curves to higher intensities, as it increases the intensity for which $v_q = v_{th}$.

In order to assess the relative significance of the collective contribution, the total curve in Fig. 2.2 must be compared with the standard inverse bremsstrahlung absorption rate. Figure 2.3 shows absorption rate plotted against laser intensity, for the intensity-corrected Spitzer expression, the estimate of the collective contribution using the modified Coulomb logarithm in Eq. (2.22), and the collective contribution calculated using the detailed model. The case of a solid-density lithium target at 250 eV is shown in Fig. 2.3(a) and a solid-density aluminium target at the same temperature in Fig. 2.3(b). In each case the collective contribution is small relative to the Spitzer term, but increases in importance with increasing laser intensity. The detailed model predicts values for the collective component of absorption which differ considerably from those given by the simple modified Coulomb logarithm.

The behaviour of the absorption resonances for $n\omega_0 \simeq \omega_p$ is shown in Fig. 2.4, where the collective absorption from the detailed model is plotted against laser wavelength. Only in the somewhat artificial case of solid-density hydrogen, in Fig. 2.4(a), does much structure survive in the total curve, and here the resonances for $n = 2$ and $n = 3$ can be clearly seen. There is a slight shift in wavelength from the ideal position due to dispersion,

$$\omega_k^2 = \omega_p^2 + 3(k_B T_e/m_e)k^2 + \ldots \tag{2.43}$$

Both dispersion and electron-ion collisions act to broaden the absorption resonances and in higher-Z targets, for example, lithium in Fig. 2.4(b), the individual resonance peaks become more difficult to distinguish.

A suggestive interpretation of the resonance peaks in Fig. 2.4 is in terms of multiphoton events: several photons being absorbed from the laser field to create a single plasmon, the energy of which is then dissipated by collisions. According to this picture, in Fig. 2.2 a three-photon process dominates the collective absorption at high laser intensities. Of course, the model outlined here is a purely classical one,

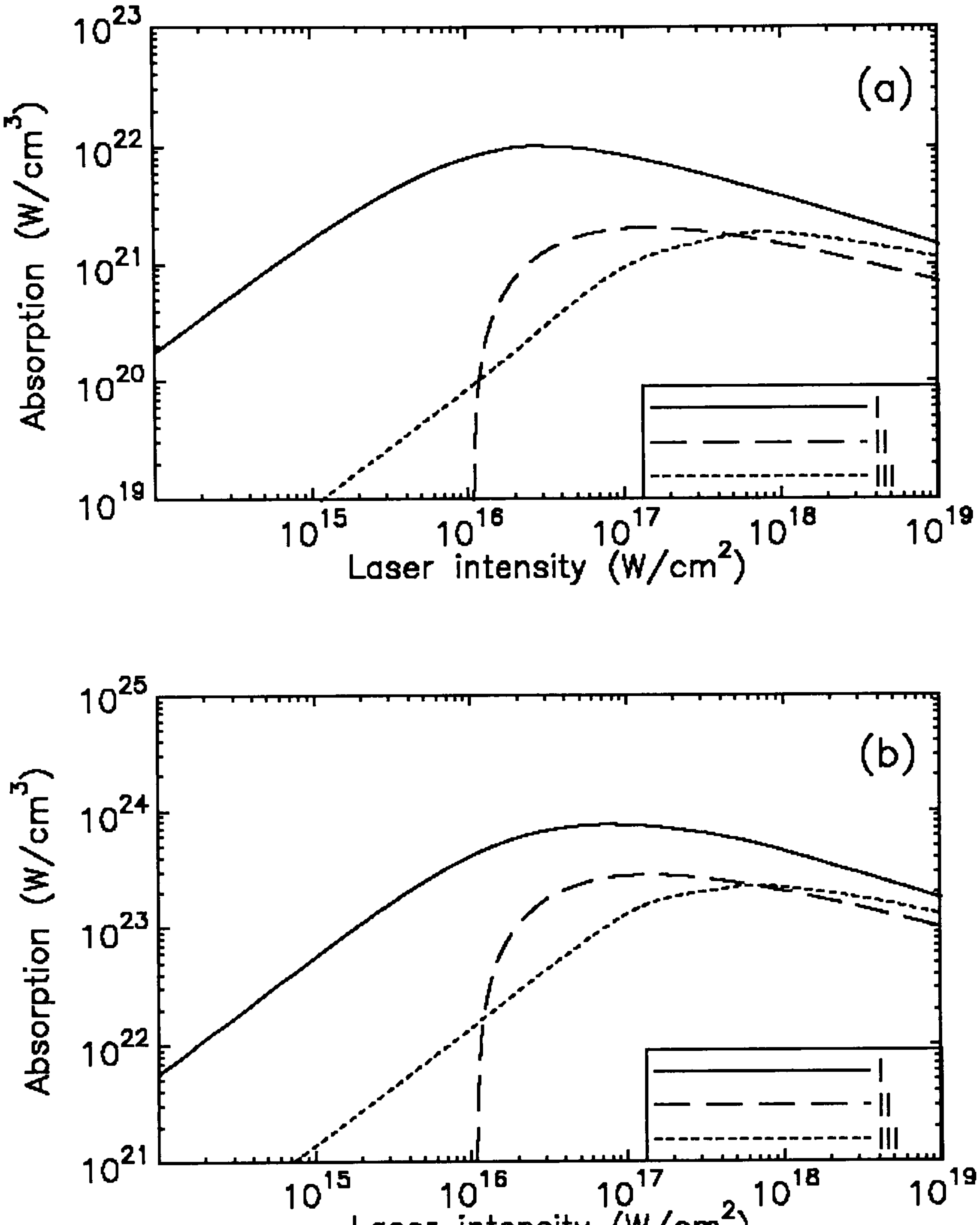

Figure 2.3: Comparison between conventional individual-particle inverse bremsstrahlung absorption (curve I), collective absorption from a simple estimate (curve II), and collective absorption from the full calculation (curve III), for (a) solid-density, fully-ionized lithium and (b) solid-density, fully-ionized aluminium.

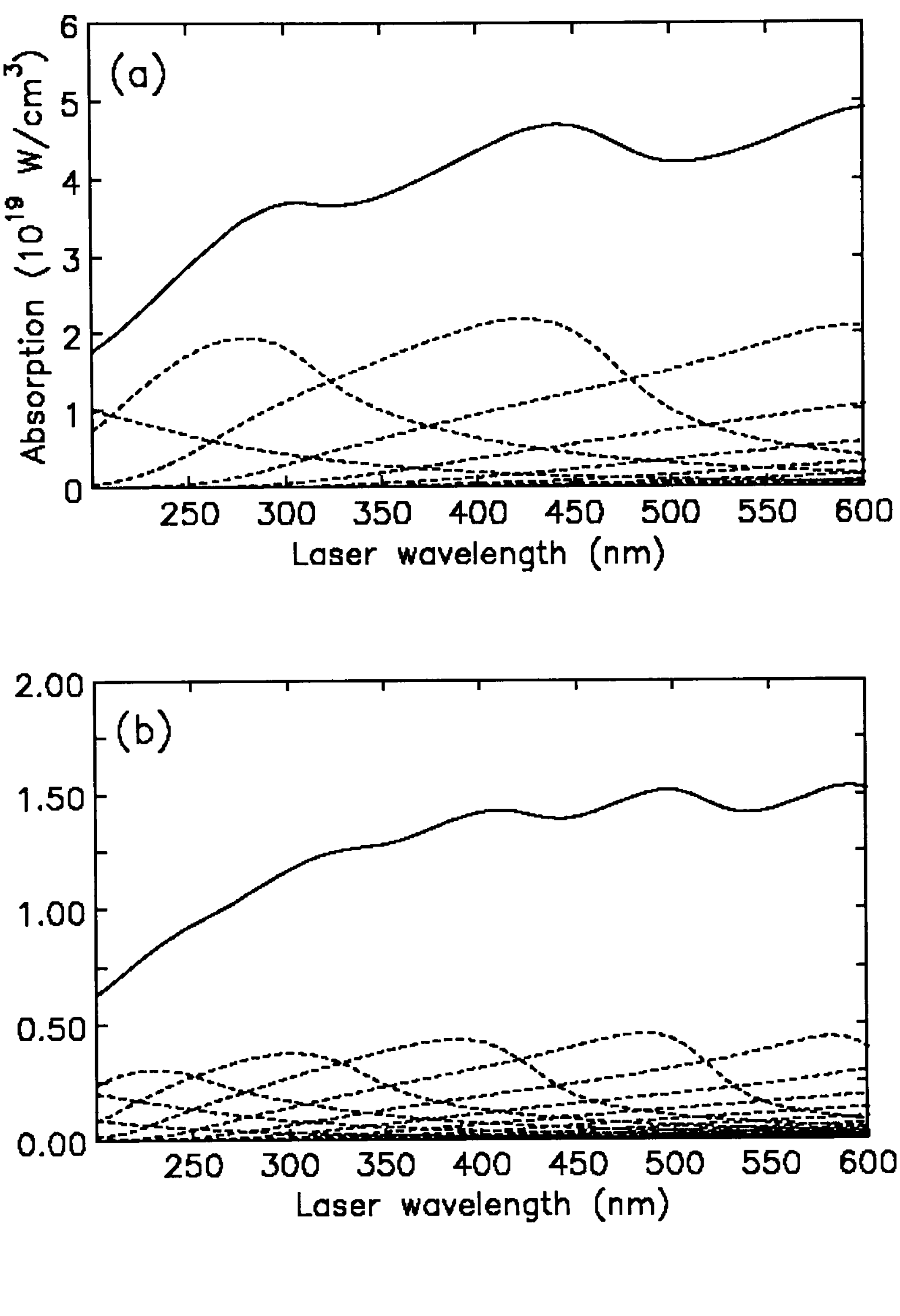

Figure 2.4: Resonances in collective absorption plotted as a function of laser wavelength, for (a) solid-density, fully-ionized hydrogen and (b) solid-density, fully-ionized lithium. Contributions from the individual terms in the summation are shown as dotted lines, and the total as a solid curve.

but the results have an interesting quantum-like appearance.

Using Eq. (2.30), it would be possible to calculate total absorption rather than just the collective contribution by changing the upper limit of the integration. The reason for not performing this full calculation is that the number of terms required in the summation would be extremely large. There are more efficient ways to calculate the standard (individual-particle) contribution to absorption.

The results presented here refer only to the high-temperature classical case but, given a suitable form for the dielectric response function, the same method could also be applied to lower-temperature systems. For $k_B T_e \ll \mathcal{E}_F$, the plasma is degenerate and strongly coupled. In this regime, a quantum mechanical dielectric function would be required, using a Fermi-Dirac distribution. In the intermediate temperature range, the plasma is strongly-coupled but no longer degenerate, and the form of the dielectric function in this case is extremely complicated [50].

2.3.4 Importance of the Collective Contribution

It has been shown here that the collective contribution to inverse bremsstrahlung absorption in laser-produced plasmas is not significant at presently achievable intensities, and in most cases can be accounted for by a small term in addition to the standard individual-particle absorption rate. Only in the combined limits of low degree of ionization, high electron temperature and ultrahigh laser intensity will the collective term become important. A simple correction to the Coulomb logarithm suggested by a straight-line stopping-power model does not give a good estimate of the collective absorption. Overall, given the relatively small contribution due to collective effects, the total absorption rate is still expected to decrease at laser intensities for which the quiver velocity exceeds the thermal velocity.

Chapter 3

A Static-Profile Model for Plasma Reflectivity in Steep Density Gradients

A computer code which simulates the evolution of a solid-density laser-produced plasma has to include models for a large number of processes and, inevitably, this will involve a compromise between physical complexity and computational efficiency. In many simulation codes, absorption of the laser light is calculated using a standard electron-ion collision frequency and high-intensity modifications, such as those discussed in the previous chapter, are not included.

In this chapter, a static-profile model is developed in order to determine the possible effect of an intensity-dependent collision frequency on the reflectivity of a femtosecond-pulse laser-produced plasma. A detailed calculation is required, because the overall effect depends on the rate at which the laser field is attenuated inside the plasma. If the field is attenuated rapidly, then the effect of an intensity-dependent nonlinearity is minimized, but if the field penetrates a large distance into the plasma, the nonlinearity could become significant. Results from this nonlinear reflectivity model have recently been published by Rae and Burnett [51].

3.1 Outline of the Model

The reflectivity of a fixed-profile plasma, assuming only collisional and resonance absorption, can be calculated by numerically solving the time-independent Helmholtz equation, for example, using a matrix method [52, 53]. A rectangular coordinate system is employed, in which the plasma density gradient is in the x-direction and an electromagnetic plane wave is incident in the xy-plane at an angle θ to the x-axis. The plasma response is described by a local dielectric function, $\epsilon = \epsilon(x)$, and the plasma is assumed to be non-magnetic, $\mu = 1$. In the case of s-polarized light, the equation for the only non-zero component of the electric field is

$$\frac{d^2 E_z(x)}{dx^2} + k_0^2(\epsilon(x) - \sin^2\theta)\, E_z(x) = 0 \ , \tag{3.1}$$

where the field takes the form

$$E_z(x, y, t) = E_z(x) \exp(-i\omega_0 t + ik_0 y \sin\theta) \ , \tag{3.2}$$

and $k_0 = \omega_0/c$ is the vacuum wavenumber. The corresponding equation for the only non-zero component of the magnetic field in the case of p-polarized light is

$$\frac{d^2 H_z(x)}{dx^2} - \frac{1}{\epsilon(x)} \frac{d\epsilon(x)}{dx} \frac{dH_z(x)}{dx} + k_0^2(\epsilon(x) - \sin^2\theta)\, H_z(x) = 0 \ . \tag{3.3}$$

In both cases there are three non-zero components of E and H, only two of which are linearly independent. Solving for the independent components generates a matrix equation, in which a 2×2 characteristic matrix contains all the information required for propagating an electromagnetic wave through the plasma. A medium of continuously varying density can be considered as equivalent to a large number of very thin slices, each of constant density, and the overall characteristic matrix is given by the product of the characteristic matrices for each slice. The electric and magnetic fields in the plasma can be calculated slice-by-slice, and the reflection coefficient for the medium as a whole can be derived from the overall characteristic matrix. This numerical procedure is stable and accurate provided that a sufficient number of slices are taken across the plasma. Typically, several hundred to a few thousand slices are required.

The dielectric function within each plasma slice is given by

$$\epsilon = 1 - \frac{n_e/n_{cr}}{1 + i\nu_{ei}/\omega_0} \ , \tag{3.4}$$

where n_e is the electron density, $n_{cr} = \epsilon_0 m_e \omega_0^2/e^2$ is the critical density and ν_{ei} is the electron-ion collision frequency. The density profile, $n_e(x)$, has to take some assumed form, for example, linear,

$$n_e = \begin{cases} n_{cr}(x/L) & \text{if } \ 0 \leq x/L \leq n_{solid}/n_{cr} \ , \\ n_{solid} & \text{if } \ x/L > n_{solid}/n_{cr} \ , \end{cases} \tag{3.5}$$

or exponential,

$$n_e = \begin{cases} n_{solid} \exp((x - x_0)/L) & \text{if } \ 0 \leq x \leq x_0 \ , \\ n_{solid} & \text{if } \ x > x_0 \ , \end{cases} \tag{3.6}$$

where x_0 is a parameter which cuts off the exponential tail at some large distance from the solid-density region. An exponential profile would be expected for a purely isothermal plasma expansion.

3.1.1 Dimensionless Parameters

In the simplest case, the collision frequency can be assumed to vary linearly with electron density. Three dimensionless parameters are then sufficient to determine the plasma reflectivity: the normalized electron density in the solid material, n_{solid}/n_{cr}, the normalized collision frequency at critical density, ν_{ei}^*/ω_0, and the normalized scale length, L/λ_0. As an example, the plasma reflectivity calculated for an exponential-profile plasma with $n_{solid}/n_{cr} = 30$ and $\nu_{ei}^*/\omega_0 = 0.1$ is shown in Fig. 3.1, as a function of the angle of incidence. For a very steep scale length, $L/\lambda_0 = 0.01$, the reflectivity curves are almost exactly those given by the Fresnel formula for reflection at a step interface [53]. For longer scale lengths, the characteristic reflectivity minimum for p-polarized light moves to lower angles, but the shape of the curve in the case of s-polarized light remains essentially unchanged. The reflectivity at normal incidence increases initially with increasing scale length, but then decreases rapidly beyond $L/\lambda_0 = 0.1$.

The situation is very different if the normalized collision frequency is reduced to a very low value. Figure 3.2 shows the angular dependence of reflectivity for p-polarized light, under the same conditions as Fig. 3.1 except that $\nu_{ei}^*/\omega_0 = 0.001$.

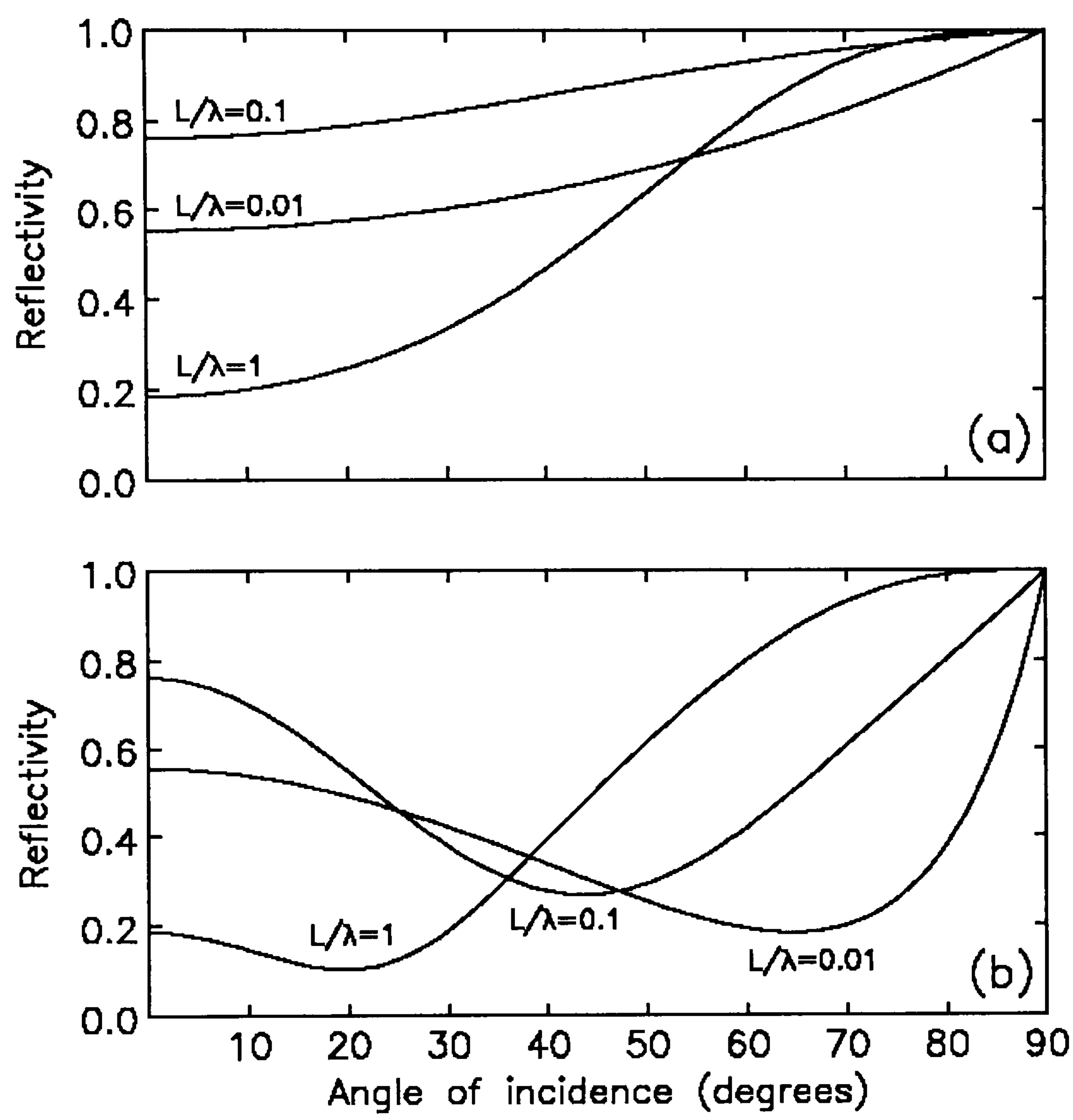

Figure 3.1: Plasma reflectivity for an exponential-profile plasma (n_{solid}/n_{cr} = 30, ν^*_{ei}/ω_0 = 0.1) as a function of the angle of incidence, for (a) s-polarized light and (b) p-polarized light.

Here collisional absorption is almost negligible, and the curves show a considerably narrower minimum which is due solely to resonance absorption. The resonance occurs because there is a component of the electric field, $E\cos\theta$, parallel to the plasma density gradient, which is able to drive a resonant plasma wave at the critical density [54, 55]. Even though the damping rate is very small, the amplitude of the resonant wave is such that significant absorption can still occur. As the angle of incidence increases, a larger component of the incident electric field is parallel to the density gradient, but the amplitude of the driving field at the critical density is reduced. This is because the laser light is actually reflected at the point where $\epsilon(x) = \sin^2\theta$, corresponding to a sub-critical density. Hence, there is some optimum angle for maximum resonance absorption. If the damping rate were reduced further, the resonance would become steeper, and the numerical procedure used here to solve the Helmholtz equation would eventually become unstable. In the case of s-polarized light, there is no component of electric field parallel to the plasma density gradient and resonance absorption cannot occur. For the conditions of Fig. 3.2, the reflectivity for s-polarized light is virtually unity at all angles of incidence.

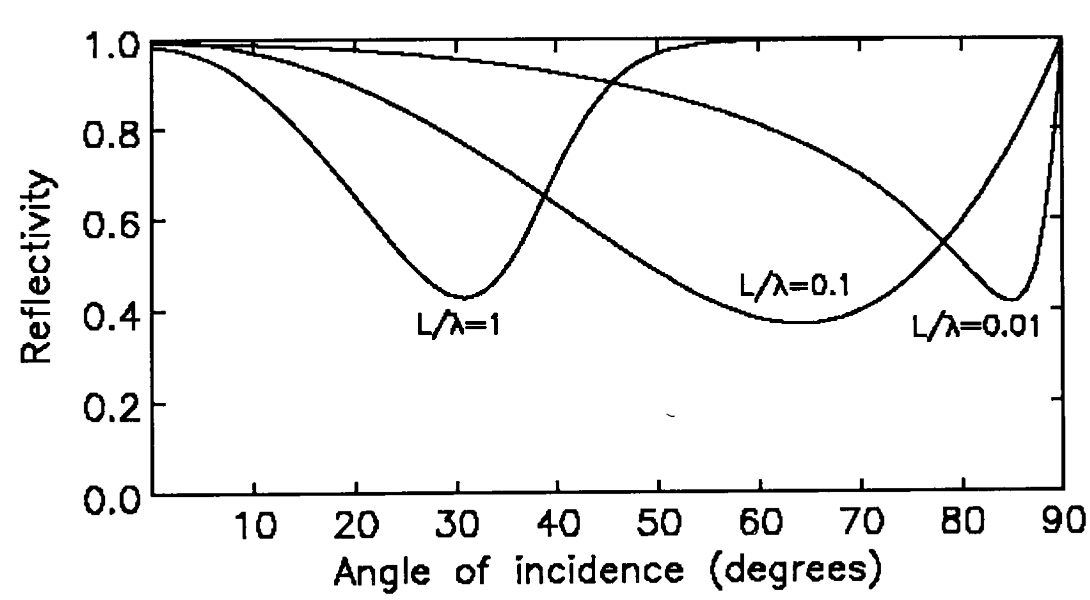

Figure 3.2: Plasma reflectivity for an exponential-profile plasma ($n_{solid}/n_{cr} = 30$, $\nu_{ei}^*/\omega_0 = 0.001$) as a function of the angle of incidence, for p-polarized light. Reflectivity for s-polarized light under the same conditions is virtually unity at all angles.

3.1.2 Including a Nonlinear Collision Frequency

Although it is convenient to be able to calculate plasma reflectivity using only three dimensionless parameters, this is no longer possible once nonlinearities in the collision frequency need to be included.

In the regime where the plasma is classical and weakly-coupled, the electron-ion collision frequency is given by the Spitzer expression [33, 34],

$$\nu_{ei} = \frac{4\sqrt{2\pi}}{3} \frac{Z n_e e^4 \ln \Lambda}{(4\pi\epsilon_0)^2 m_e^{1/2} (k_B T_e)^{3/2}} , \tag{3.7}$$

where Z is the degree of ionization and $\ln \Lambda$ is the Coulomb logarithm, defined in the usual way. At low temperatures ($k_B T_e / Z \lesssim 10$ eV for solid-density aluminium) the Spitzer expression becomes invalid, and a collision rate appropriate for a strongly-coupled plasma would need to be used instead [35].

If the laser intensity is such that the electron quiver velocity is comparable with or greater than the thermal velocity, then the Spitzer expression needs modification, as described in Chapter 2. In order to have a convenient expression for the intensity dependence, a correction factor discussed by Schlessinger and Wright [40] will be used. This factor is given by

$$F = \left(1 + \left\langle v_q^2 \right\rangle / 3 v_{th}^2\right)^{-3/2} , \tag{3.8}$$

where $v_{th} = (k_B T_e / m_e)^{1/2}$ and

$$\left\langle v_q^2 \right\rangle = \frac{e^2 E^2}{2 m_e^2 (\omega_0^2 + \nu_{ei}^2)} . \tag{3.9}$$

The modified collision rate thus has a complicated intensity-dependence and the Helmholtz equation must be solved iteratively to obtain solutions for the fields.

3.1.3 The Effect of Wavebreaking

In the case of p-polarized light, the reduction in collision rate leads to a further complication. As there is a component of the incident field in the direction of the density gradient, a resonant wave can be driven in the plasma at the critical density. At low incident intensities this resonance is strongly damped, but at higher intensities the nonlinearity in the collision frequency allows the resonance to grow to the point where spatial dispersion and wavebreaking effects must be considered. These phenomena are closely linked, and both act to limit the maximum size of the resonantly-driven plasma wave.

Spatial dispersion arises because the oscillatory motion of the electrons generates a non-local dielectric function. Using Eq. (3.4) and Maxwell's curl equation for $\nabla \times H$, the resonantly-enhanced electric field around the critical density is found to be

$$E_x(x) = \left(\frac{\mu_0}{\epsilon_0}\right)^{1/2} \frac{H_z(x)\sin\theta}{\epsilon(x)} = \left(\frac{\mu_0}{\epsilon_0}\right)^{1/2} \frac{H_z(x)\sin\theta}{x'/L - i\nu_{ei}/\omega_0} \,. \tag{3.10}$$

Here $x' = x_{cr} - x$, and it is assumed that $\nu_{ei}/\omega_0 \ll 1$ and that the density profile is locally linear with scale length L. Incorporating the oscillatory motion of the electrons suggests that Eq. (3.10) should more correctly be written as

$$E_x(x) = \left(\frac{\mu_0}{\epsilon_0}\right)^{1/2} \frac{H_z(x)\sin\theta}{\frac{1}{L}\left(x' + \int_0^T v_z\,dt\right) + i\nu_{ei}/\omega_0} \,. \tag{3.11}$$

The dispersion term in the denominator ensures that, even for $\nu_{ei} = 0$, the driven field remains finite. Harmonics of the laser frequency can also be generated at the resonant point [56].

The major factor which limits the amplitude of the resonantly-driven wave is wavebreaking, first proposed by Dawson [57], and subsequently investigated by many workers [58, 59, 60, 61]. If an electron starting from a position x_0 oscillates with a displacement given by $\xi(t)$, then there may be some value of t for which the condition

$$|d\xi/dx_0| = 1 \tag{3.12}$$

is met. If this occurs, then particles which were initially adjacent overlap, and the wave will break. Consider the simple case of a driven, damped harmonic oscillator,

$$\frac{d^2\xi}{dt^2} + \nu_{ei}\frac{d\xi}{dt} + \omega_p^2\xi = -\frac{eE_d}{m_e}\exp(i\omega_0 t) \ , \tag{3.13}$$

where $E_d = (\mu_0/\epsilon_0)^{1/2} H_z \sin\theta$ is the driving field, $\omega_p = (e^2 n_e/\epsilon_0 m_e)^{1/2}$ is the plasma frequency and the density gradient scale length is locally linear, that is, $n_e = n_{cr}(x_0/L)$. Assuming that $\xi \ll L$, the steady-state solution is

$$\xi(t) = \frac{eE_d \exp(i\omega_0 t)}{m_e\left(\omega_0^2 - \omega_p^2 - i\nu_{ei}\omega_0\right)} \ , \tag{3.14}$$

where the x_0 dependence is contained in the plasma frequency. Solving Eq. (3.12), the displacement at breaking is found to be

$$\xi_{br} = \left(\frac{eE_d L}{m_e\omega_0^2}\right)^{1/2} \ , \tag{3.15}$$

and the breaking field is

$$E_{br} = \left(\frac{m_e\omega_0^2 E_d L}{e}\right)^{1/2} \ . \tag{3.16}$$

Here spatial dispersion has been neglected, and this is only strictly valid if the plasma frequency is independent of the displacement. Including dispersion, Eq. (3.13) should more correctly be written as

$$\frac{d^2\xi}{dt^2} + \nu_{ei}\frac{d\xi}{dt} + \omega_p^2\xi\left(1 + \frac{\xi}{x_0}\right) = -\frac{eE_d}{m_e}\exp(i\omega_0 t) \ . \tag{3.17}$$

The solution to this can be obtained in terms of a Fourier series,

$$\xi = \xi_1 \exp(i\omega_0 t) + \xi_2 \exp(2i\omega_0 t) + \ldots \tag{3.18}$$

Taking only the first two terms in this expansion, it can be shown that for $\nu_{ei} \simeq 0$ the displacement near resonance does not become infinite, but has a limiting value,

$$\xi_1 \to \left(\frac{6eE_d L^2}{m_e\omega_0^2}\right)^{1/3} \ . \tag{3.19}$$

However, as ξ_1 in Eq. (3.19) will always be greater than ξ_{br} in Eq. (3.15), the wave will break before it reaches the maximum amplitude imposed by spatial dispersion. Thus, it is only necessary to include a mechanism for limiting the maximum amplitude of the wave to the wavebreaking value, and dispersion effects can be neglected.

Particle-in-cell simulations performed by various groups [62, 63, 64, 65] have shown that wavebreaking leads to absorption and the generation of hot electrons, but it is beyond the scope of the present dielectric function approach to include a complex distribution of electron energies. Instead, wavebreaking is modelled by including an extra term in the dissipative part of the dielectric function around the resonance region, in order to limit the maximum field to the breaking field given by Eq. (3.16). This has been shown by Freidberg *et al.* [66] to give approximately the same plasma reflectivity as the full treatment. Effectively, the electron-ion collision frequency near resonance is limited to a minimum value, given by

$$(\nu_{ei})_{min} = \left(\frac{eE_d}{m_e L}\right)^{1/2} . \tag{3.20}$$

With this correction for wavebreaking, the effect of an intensity-dependent collision frequency for p-polarized light can be calculated.

3.2 Modified Plasma Reflectivity

The nonlinear Helmholtz equation was solved iteratively, using the matrix method outlined earlier, with a computer program written in FORTRAN 77. A typical run required several minutes of CPU time on a VAX 7800 processor.

In order to show the effect of the nonlinearity, the reflectivity of an exponential-profile plasma was calculated as a function of the angle of incidence for two different intensities, 10^{14} W/cm^2 and 10^{17} W/cm^2. In each case, a constant set of parameters was used: $T_e = 200$ eV, $Z = 10$, $n_{solid} = 34\, n_{cr}$ (appropriate to solid-density aluminium), and $\lambda_0 = 248$ nm. Calculations were performed for density gradient scale lengths $L/\lambda_0 = 1$, 0.1 and 0.01.

Figure 3.3 shows the results for the case of s-polarized light. The higher laser intensity leads to an increase in reflectivity at all scale lengths, with the strongest effect for $L/\lambda_0 = 1$ and an almost insignificant change for $L/\lambda_0 = 0.01$. The basic shape of the reflectivity curve is unaltered by variations in intensity and in each case the reflectivity increases monotonically from $\theta = 0°$ to $\theta = 90°$.

For the case of $\theta = 20°$ and $L/\lambda_0 = 1$, Fig. 3.4 shows the electric field and the imaginary part of the dielectric function,

$$\mathrm{Im}\,\epsilon = \frac{n_e}{n_{cr}}\frac{\nu_{ei}}{\omega_0}\left(1+\frac{\nu_{ei}^2}{\omega_0^2}\right)^{-1}, \tag{3.21}$$

as functions of distance into the plasma. At 10^{14} W/cm^2, Im ϵ is simply proportional to the density, but at 10^{17} W/cm^2 the nonlinearity has both lowered the average collision frequency and introduced a periodic variation. The corresponding electric field shows an enhanced peak-to-peak amplitude as a result of the higher overall reflectivity.

The angular dependence of reflectivity in the case of p-polarized light is shown in Fig. 3.5. In this case, there is also an overall increase in reflectivity with intensity, but the curves no longer retain their original shape, the characteristic resonance minimum moving to higher angles. The increase in reflectivity at the higher intensity is most noticeable for a scale length of $L/\lambda_0 = 1$, where the resonance is also considerably narrowed. For a shorter scale length, the increase in reflectivity at the higher intensity is relatively small.

Figure 3.6 shows the variation in the electric field and the imaginary part of the dielectric function, again for $\theta = 20°$ and $L/\lambda_0 = 1$. Here the most notable feature is the resonance at critical density, which is heavily damped at the lower laser intensity, but much less strongly damped at the higher intensity. The amplitude of the electric field in the latter case is limited by wavebreaking to about $20\,E_0$.

In order to show how the penetration of the laser light into the plasma varies with the scale length, the electric field and electron density are plotted in Fig. 3.7 as functions of distance into the plasma, for an intensity of 10^{17} W/cm^2 and normal incidence. For $L/\lambda_0 = 1$, there is a relatively large underdense region and the light is reflected well before reaching solid density; as the gradient steepens, the light is attenuated much more rapidly, but penetrates to a higher plasma density.

The degree of electric field penetration determines to a large extent the sig-

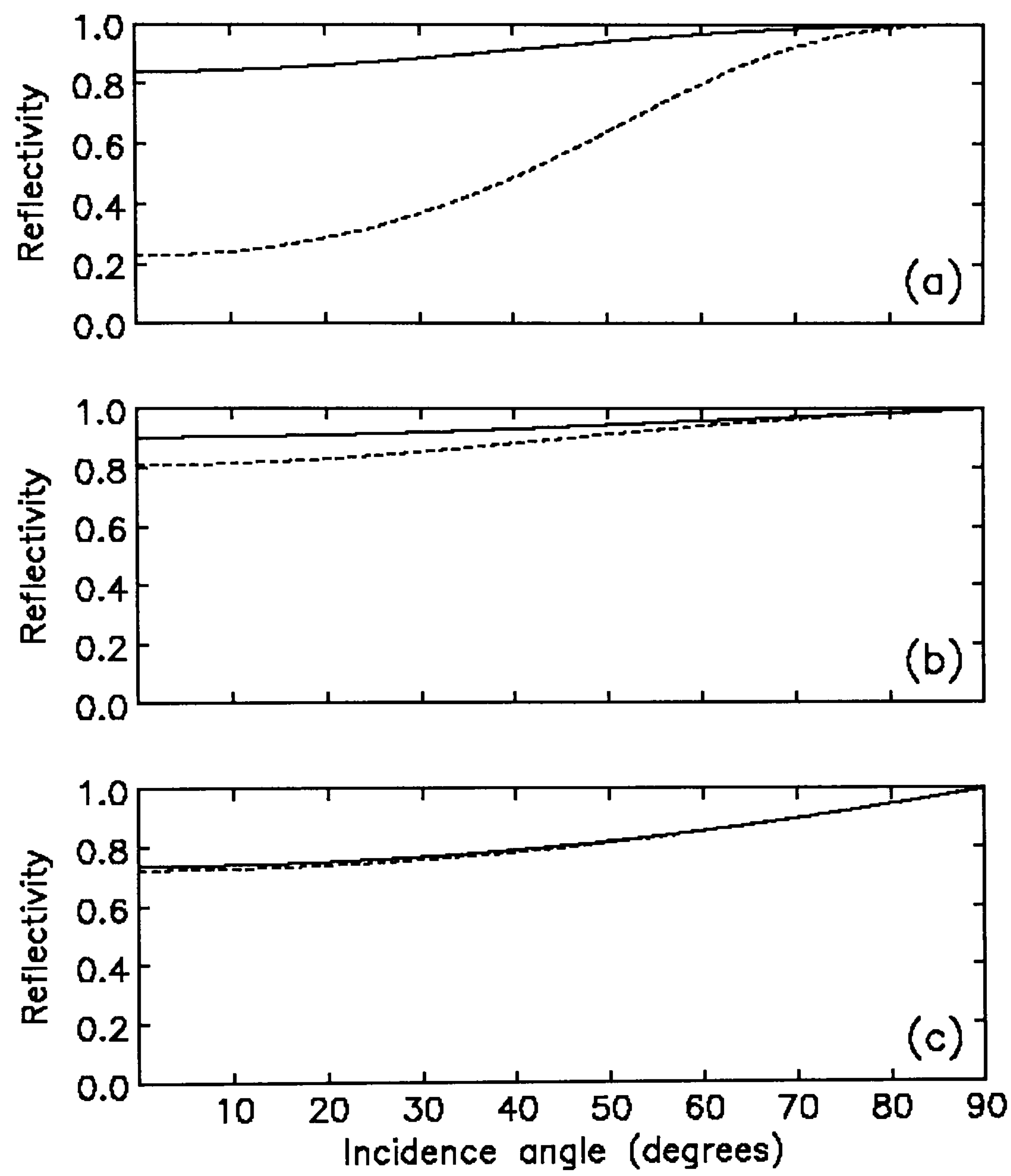

Figure 3.3: Angular dependence of reflectivity for s-polarized light and scale lengths (a) $L/\lambda_0 = 1$, (b) $L/\lambda_0 = 0.1$, and (c) $L/\lambda_0 = 0.01$. Curves shown for 10^{14} W/cm^2 (broken line) and 10^{17} W/cm^2 (solid line).

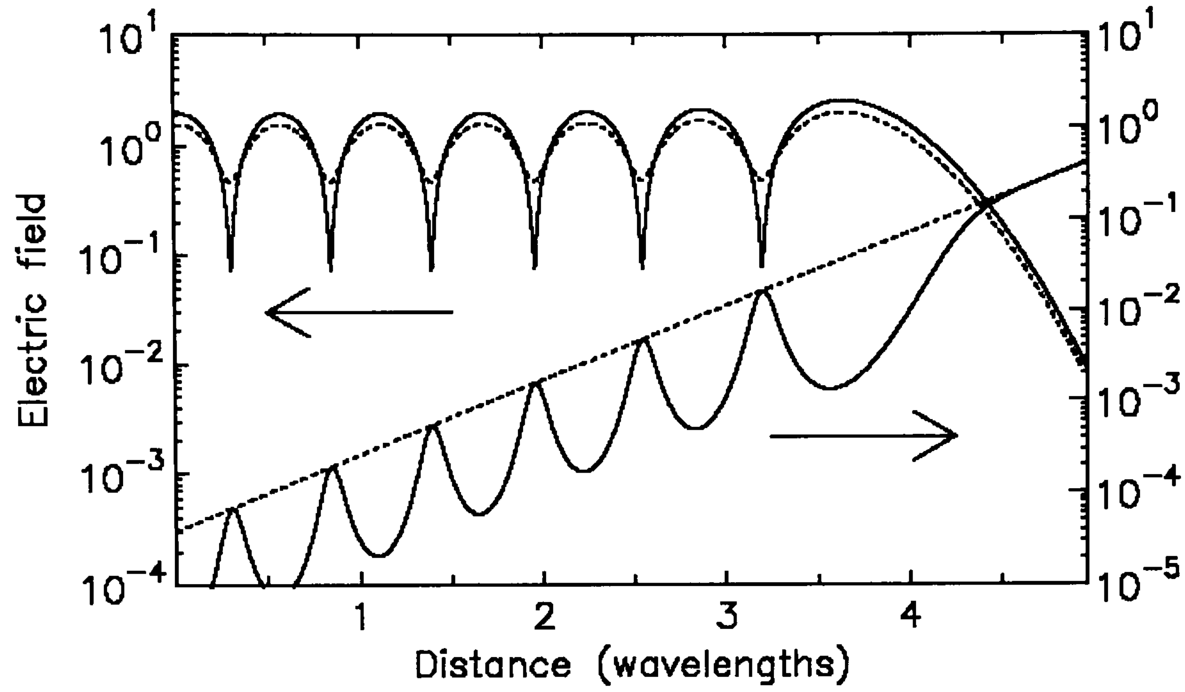

Figure 3.4: Dependence of the electric field (normalized to the incident field) and the imaginary part of the dielectric function against distance, for s-polarized light and $L/\lambda_0 = 1$. Curves shown for 10^{14} W/cm^2 (broken line) and 10^{17} W/cm^2 (solid line).

nificance of the nonlinearity in the collision frequency. In certain cases, particularly for s-polarized light and $L/\lambda_0 = 1$, the increase in reflectivity due to the nonlinear collision frequency is dramatic. As seen in Fig. 3.3, the reflectivity at normal incidence increases from 23% at 10^{14} W/cm^2 to 84% at 10^{17} W/cm^2. For this scale length there is a relatively large region of underdense plasma where the electric field remains close to its incident value, and the nonlinearity thus operates over a extended length of plasma. As the density gradient steepens, the nonlinear effect becomes weaker, until for $L/\lambda_0 = 0.01$ the reflectivity (for s-polarized light at least) is virtually independent of laser intensity. This change is associated with the rapid attenuation of the electric field in cases where the density profile approaches a step interface.

In the results for p-polarized light, the increase in reflectivity is less marked for long scale lengths, but still noticeable for very short scale lengths. In all cases there is a shift in the position of minimum reflectivity toward higher angles at higher intensity. At 10^{17} W/cm^2 and for $L/\lambda_0 = 1$, the additional absorption in the case

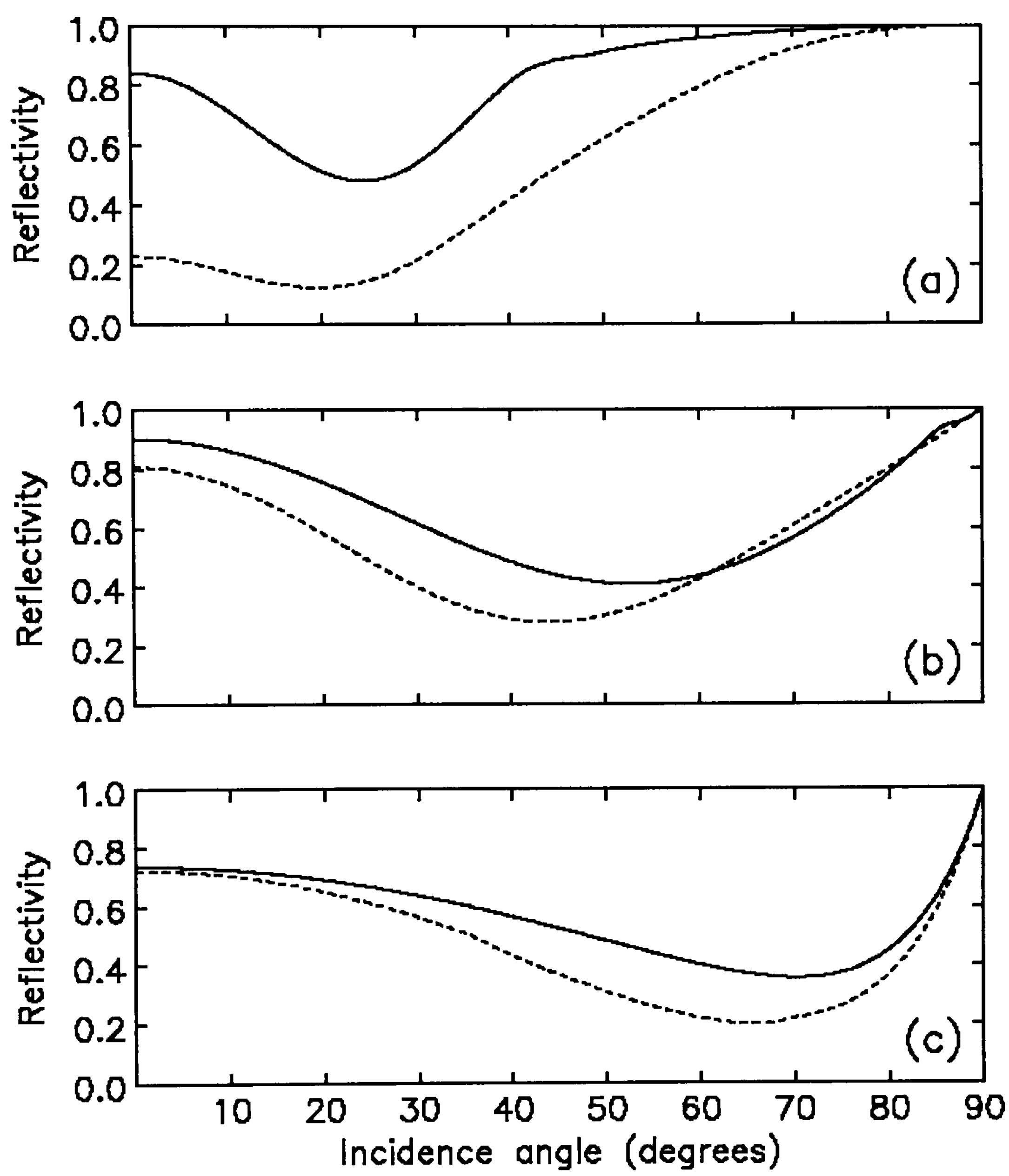

Figure 3.5: Angular dependence of reflectivity for p-polarized light and scale lengths (a) $L/\lambda_0 = 1$, (b) $L/\lambda_0 = 0.1$, and (c) $L/\lambda_0 = 0.01$. Curves shown for 10^{14} W/cm^2 (broken line) and 10^{17} W/cm^2 (solid line).

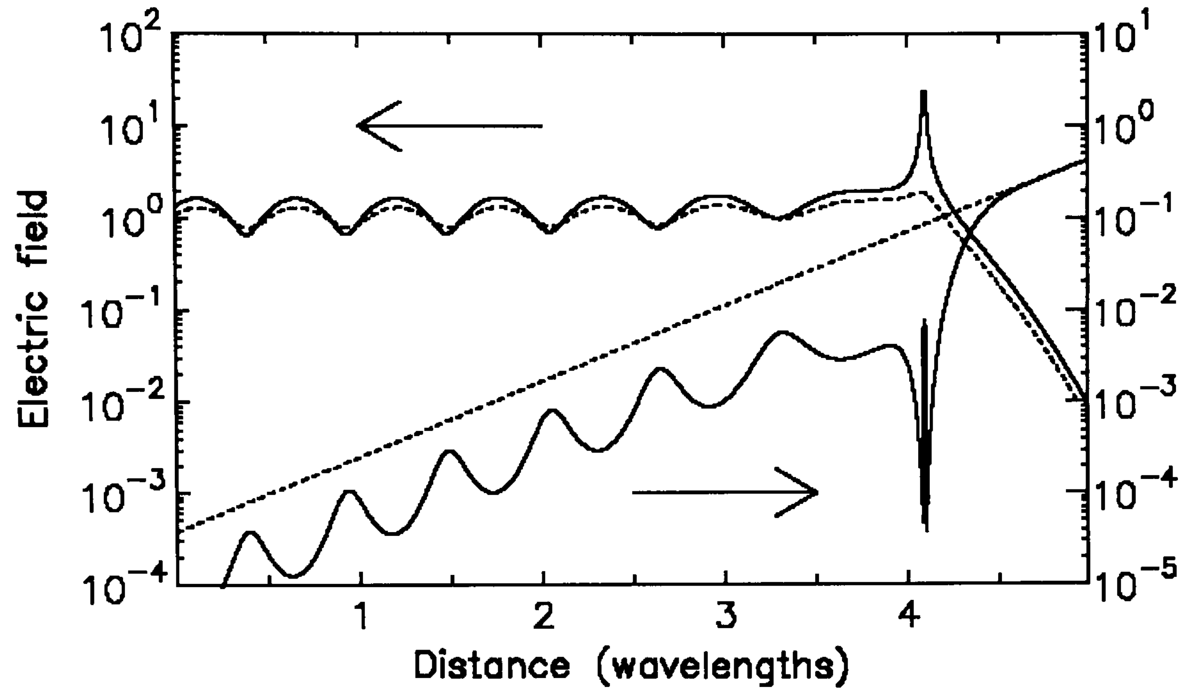

Figure 3.6: Dependence of the electric field (normalized to the incident field) and the imaginary part of the dielectric function against distance, for p-polarized light and $L/\lambda_0 = 1$. Curves shown for 10^{14} W/cm^2 (broken line) and 10^{17} W/cm^2 (solid line).

of p-polarized compared to s-polarized light is due to the growth and breaking of a resonant plasma wave at critical density. The shape of the reflectivity curve changes at the higher intensity because the underlying component of collisional absorption is reduced and only the resonance component remains. As the collision frequency outside the wavebreaking region is greatly reduced in this case, the situation is quite similar to collisionless resonance absorption. Particle-in-cell simulations [61] have shown that approximately 50% absorption is possible at the optimum angle of incidence, and this agrees with the results of the present model.

Analytical solutions to the problem of plasma reflectivity are only available in a certain number of restricted cases [67]. For a vacuum-to-plasma step interface and a constant collision frequency, the Fresnel equations describe reflectivity for s-polarized and p-polarized light in terms of the angle of incidence and the complex angle of refraction. If the dielectric function varies slowly on the scale of a laser wavelength, a WKB solution can be obtained in the case of s-polarized light. The Fresnel equations and the WKB solution have been used as a check for the accuracy of the present

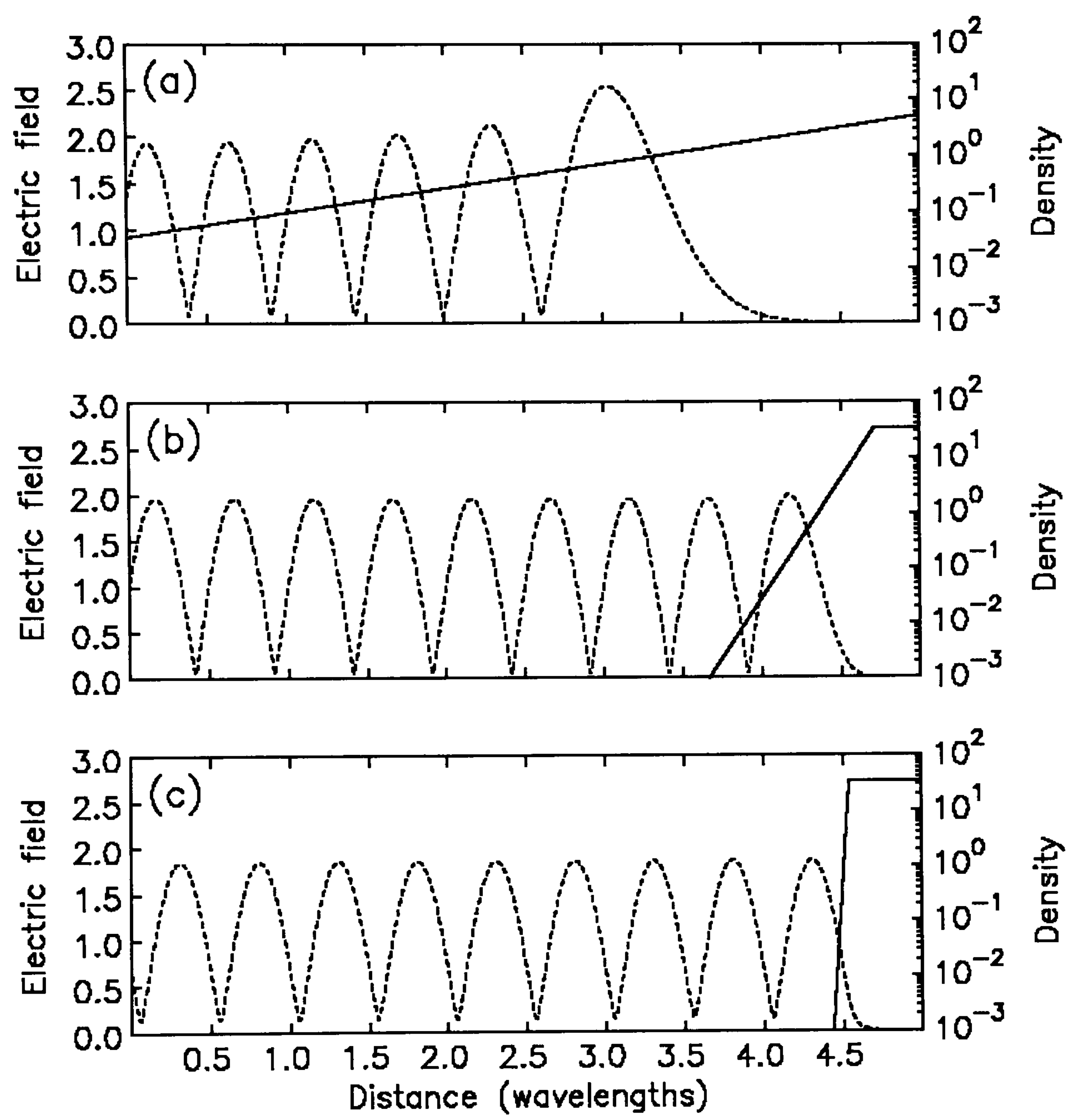

Figure 3.7: Penetration of a normally-incident light wave into a solid-density plasma with (a) $L/\lambda_0 = 1$, (b) $L/\lambda_0 = 0.1$, and (c) $L/\lambda_0 = 0.01$. Solid line shows the plasma electron density, normalized to critical density; broken line shows the electric field, normalized to the incident field.

model. However, none of these exact or approximate analytical solutions are valid in the case where the dielectric function varies with the local electric field.

The correction factor used to calculate the nonlinear collision frequency is an approximation which assumes that the electron velocity distribution is not greatly perturbed from the original Maxwellian. The use of a self-consistent distribution would probably lower the effective collision frequency further and this would increase the high-field reflectivity beyond that predicted by the present model. In addition, it is assumed here that the electron temperature does not change with intensity; if allowance were made for an increase in temperature at high intensities, the high-field reflectivity would also increase.

In order to solve the nonlinear wave equation, the present model assumes a fixed density profile for the plasma, which means that it must average over any plasma motion. In this way, it is difficult to include time-dependent phenomena, both related to electrons (growth and breaking of resonant plasma waves) and ions (expansion of the plasma, and ponderomotive density profile steepening). Ion motion is the easier of these to address, since the laser pulse is so short that any such motion must necessarily be very limited. As an example, consider density profile steepening. Particle-in-cell simulations performed by Forslund *et al.* [68] have shown that an initially linear density profile can develop a sharp jump around the critical density, as a result of pressure generated both by the reflecting laser beam and by the resonantly-driven electrostatic wave. The time taken for this feature to develop is on the order of 50 laser cycles in simulations with an electron-ion mass ratio of 1:100. In the case of a solid-density aluminium plasma, the mass ratio is almost 500 times smaller, so the characteristic time should be $\sqrt{500}$ times longer. Although this rules out any significant bulk motion of ions in a femtosecond laser pulse, a smaller movement across the narrow resonance region is still possible and this could have an important effect on the reflectivity, as the behaviour in the vicinity of the resonant point dominates the overall response. A time-dependent particle-in-cell code would be the ideal way to investigate such phenomena, but in such a code it is difficult to incorporate nonlinear collisional effects.

In the case of p-polarized light, it appears that the local electric field around the critical density can be enhanced by more than an order of magnitude before wavebreaking occurs. This extremely large field in a buried layer of the plasma could lead to some interesting effects, in particular, rapid ionization due to field-induced processes and the generation of very hot electrons. However, the detailed investigation of this behaviour goes far beyond the scope of a simple model.

The effect of the collective excitation mechanism discussed in Chapter 2 has also been investigated using the reflectivity model. However, even at 10^{17} W/cm^2 in a long-scale-length plasma, the change in reflectivity due to this effect is negligible. At still higher intensities, collective effects may become important, but the problem is then significantly more complicated owing to the number of other competing high-intensity modifications.

3.3 Relevance to High-Intensity Experiments and Computer Simulations

From the results above, it is possible to draw some general conclusions regarding light absorption in intense femtosecond-pulse laser-produced plasmas. Once the incident intensity is sufficiently high that the electron quiver velocity exceeds the thermal velocity, modifications to the electron-ion collision frequency will reduce the fraction of energy absorbed in the plasma. The severity of this effect depends both on the polarization of the light and on the density profile scale length, being most severe for s-polarized light and scale lengths $L/\lambda_0 \gtrsim 1$. For shorter scale lengths, the rapid attenuation of the electric field inside the plasma reduces the importance of the nonlinearity, and in the limit of a step-like plasma the intensity dependence of the reflectivity is quite weak. For p-polarized light, the resonance absorption arising from wavebreaking is insensitive to the laser intensity and the reflectivity shows a weaker intensity dependence.

For intensities above about 10^{15} W/cm^2, the intensity-dependence of the collision frequency will need to be included in plasma simulation codes. The modelling of experiments designed to measure the reflectivity of a femtosecond-pulse laser-produced plasma (for example, Milchberg *et al.* [69, 70], Kieffer *et al.* [71, 72] and Fedosejevs *et al.* [7, 73]), may need to include nonlinear effects. At the highest intensity so far used in these experiments, 2.5×10^{15} W/cm^2 at 248 nm, the nonlinear modification to the collision frequency probably has only a small effect, but at higher intensities, parameters derived from a linear model will no longer be accurate.

At ultrahigh intensities, other effects also need to be considered, such as field-induced ionization, profile modification and the production of hot electrons. The full investigation of these phenomena would require a time-dependent treatment including a dynamical description of the electron and ion populations.

Chapter 4

A Comparison of Field-Induced and Collisional Ionization Rates

In a laser-produced plasma, the equilibrium degree of ionization represents a balance between ionization and recombination processes. In a low-density plasma, three-body recombination is negligible, and collisional ionization is balanced by radiative recombination, leading to a so-called coronal equilibrium. At the opposite extreme, in a dense plasma, the populations of atoms and ions are controlled entirely by collisions. This is the regime of local thermal equilibrium. In general, the density falls somewhere between these two limits, and both radiative and three-body recombination processes must be considered. Ionization is commonly assumed to occur only by electron impact. This is certainly a valid simplification above a certain plasma temperature, and for a relatively low laser intensity. However, during the initial stages of evolution of a solid-density plasma produced by an intense femtosecond laser pulse, or more especially in a gaseous plasma, the effect of collisions will be diminished and field-induced ionization may become important.

The relationship between field-induced and electron-impact ionization in laser-produced plasmas is not a topic which has been widely discussed in the literature, so in this chapter a brief comparison is made between the two processes. The theory relating to field-induced ionization is summarized, field-induced ionization rates from two different models are calculated for a range of laser intensities and these are compared with collisional ionization rates calculated under a range of plasma conditions.

4.1 Field-Induced Ionization

The study of ionization in an intense laser field is a rapidly-expanding area of research. Many theoretical approaches to the problem of calculating field-induced ionization rates have been developed [74, 75, 76], but no single treatment is valid and accurate for a wide range of intensities and different atomic species. Experiments to measure field-induced ionization rates are difficult to perform and often, due to a variety of associated effects, are unable to distinguish clearly between competing theoretical models. Below, several models for field-induced ionization will be briefly outlined, and the intensity range over which each is applicable will be discussed.

It is convenient to specify the laser intensity using a dimensionless parameter, and here the adiabaticity or tunnelling parameter, γ, will be used. This is defined by

$$\gamma = (\mathcal{E}_i/2\mathcal{E}_q)^{1/2} , \tag{4.1}$$

where $\mathcal{E}_i$ is the ionization potential. The quiver or ponderomotive energy, $\mathcal{E}_q$, is given by

$$\mathcal{E}_q = \frac{e^2E^2}{4m_e\omega_0^2} , \tag{4.2}$$

where ω_0 is the laser angular frequency and E is the peak electric field.

4.1.1 Perturbation Theory

If the laser electric field is small with respect to the atomic binding potential, such that $\gamma \gg 1$, perturbation theory can be used [77]. In this case, the rate for k-photon ionization is given by

$$\mathcal{R}_k = \sigma_k I^k , \tag{4.3}$$

where I is the laser intensity and σ_k is a generalized k-photon cross-section.

At low intensities, around 10^{12} W/cm^2, experiments have confirmed the power-law dependence on intensity up to quite high values of the exponent [78], but the *ab initio* calculation of the cross-section and its dependence on laser wavelength is a difficult task. Multiphoton cross-sections have been calculated by Karule [79] for hydrogen, and rules have been developed by Lambropoulos [77] for scaling these to other elements, but theoretical predictions made using the scaled cross-sections disagree with the experimental results of Perry *et al.* [80]. Often, the values of the cross-sections are simply left as adjustable parameters, to be determined by fitting theoretical curves to experimental data. This procedure can result in an acceptable fit even at intensities above 10^{14} W/cm^2, if a correction to the ionization potential is made to account for the ponderomotive shift. Such corrections are automatically included in more-advanced nonperturbative theories. Resonances with intermediate states can also play an important role, enhancing the ionization rate by orders of magnitude for certain laser wavelengths [81, 82].

4.1.2 Nonperturbative Methods

Above a certain limiting intensity, perturbation theory breaks down and the field-induced ionization rate no longer varies according to a strict power law. A number of nonperturbative approaches have been developed for the high-intensity regime, including the Keldysh model [83], Floquet theory [84, 85], time-dependent Hartree-Fock theory [86], solution of a set of coupled rate equations [87] and direct numerical integration of the Schrödinger equation [88, 89, 90].

Owing to its relatively simple form, the Keldysh model is the most widely-used method for calculating intense-field ionization rates. The basic assumption of this model is that the electron makes a transition directly from the ground state of the atom to a free, quivering state in the laser field (a Volkov state). The internal structure of the atom is thus assumed to be less important than the final state of the ionized electron. As the Keldysh model neglects the effect of the final atomic potential on the outgoing electron, it best describes the case of ionization from a simple negative ion, but the model is often used to provide approximate ionization rates for ions of arbitrary charge-state.

The full Keldysh expression for the ionization rate is given by [83]

$$\mathcal{R} = A\,\omega_0 \left(\frac{\mathcal{E}_i}{\hbar\omega_0}\right)^{3/2} \left(\frac{\gamma}{\sqrt{1+\gamma^2}}\right)^{5/2} S\left(\gamma, \frac{\tilde{\mathcal{E}}_i}{\hbar\omega_0}\right)$$
$$\times \exp\left[-\frac{2\tilde{\mathcal{E}}_i}{\hbar\omega_0}\left(\sinh^{-1}\gamma - \frac{\gamma(1+\gamma^2)^{1/2}}{1+2\gamma^2}\right)\right] . \tag{4.4}$$

Here ω_0 is the laser angular frequency, $\mathcal{E}_i$ is the ionization potential, $\tilde{\mathcal{E}}_i = \mathcal{E}_i + \mathcal{E}_q$ is the ionization potential including the ponderomotive shift and A is a numerical factor of order unity which allows for a weak dependence on the atomic structure. The function $S(\gamma, x)$, which includes a summation over all possible multiphoton orders, is given by

$$S(\gamma, x) = \sum_{m=0}^{\infty} \left\{\exp\left[-\left(2\left\langle x+1\right\rangle - x + m\right)\left(\sinh^{-1}\gamma - \frac{\gamma}{\sqrt{1+\gamma^2}}\right)\right]\right\}$$
$$\times \Phi\left\{\left[\frac{2\gamma}{\sqrt{1+\gamma^2}}\left(\langle x+1\rangle - x + m\right)\right]^{1/2}\right\} . \tag{4.5}$$

The notation $\langle x+1\rangle$ means the integer part of $x+1$, and the function $\Phi(x)$, related to the error function, is given by

$$\Phi(x) = \int_0^x \exp(t^2 - x^2)\, dt \ . \tag{4.6}$$

The Keldysh expression reduces to simpler forms in the low-field and high-field limits, for which $\gamma \gg 1$ and $\gamma \ll 1$, respectively. In the low-field limit, the expression reduces to the same power-law relationship as that given by perturbation theory. In the high-field limit, the expression simplifies to an exponential dependence, related to the probability of an electron tunnelling out of a short-range potential well under the action of a static electric field [91].

The Keldysh model has been found to reproduce the results of intense-field ionization experiments in a qualitative way, but provides semi-quantitative predictions in the case of the first charge-state only [80]. For higher charge-states, the theory can only be made to fit experimental results if the constant A is given extremely large (non-physical) values. The theoretical shortcomings of the Keldysh

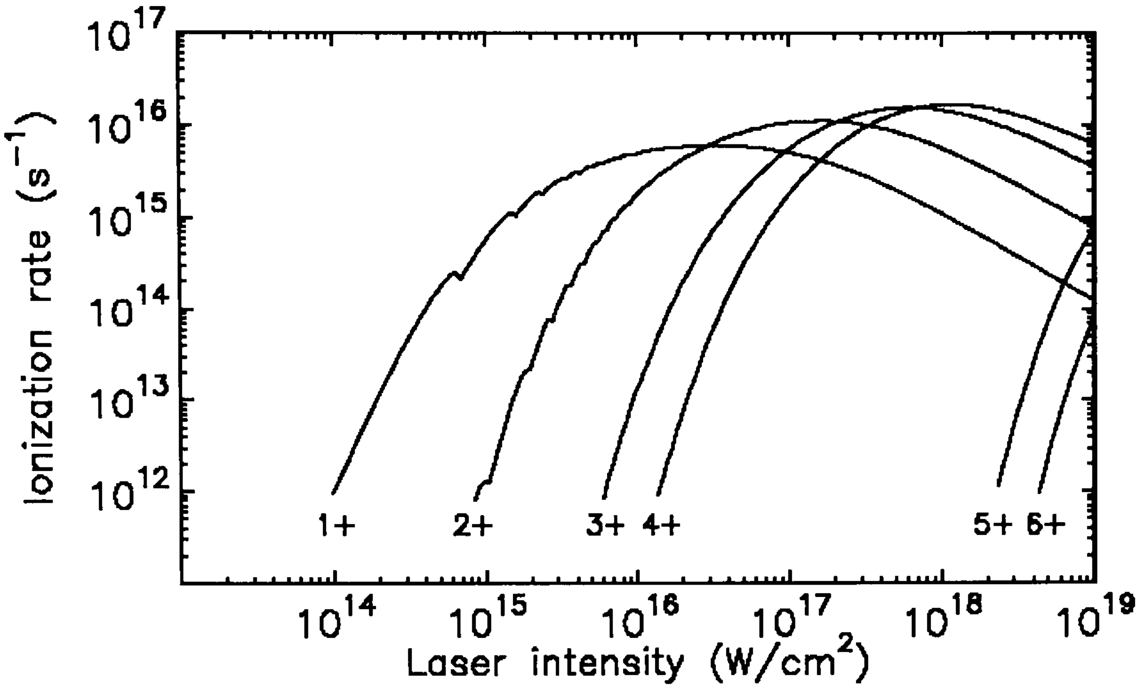

Figure 4.1: Keldysh ionization rates for carbon as a function of laser intensity, for 248 nm light.

model have been discussed by several authors [92, 93, 94], and various corrected models have been proposed [95, 96, 97]. Despite its obvious problems, however, the basic model is often used as a benchmark for the calculation of approximate ionization rates.

Figure 4.1 shows the predicted ionization rates for the various charge-states of carbon as a function of laser intensity, calculated using the full Keldysh expression, Eq. (4.4), with A equal to unity. There is a slight wavelength dependence at lower intensities; the results here are plotted for 248 nm light, and a longer wavelength would lead to a slightly increased ionization rate.

The curves all show a steep increase in ionization rate at low intensities (with the gradient given by the perturbative power-law), followed by a region of saturation and eventually a decrease at high intensities. It is clear that the most important region of the curves is before saturation, as a rate of, for example, 10^{14} s^{-1} will lead to complete ionization in ~10 fs. As saturation is approached, the ionization rates become comparable with the laser frequency ($\omega_0 = 7.60 \times 10^{15}$ s^{-1} for 248 nm) and the model breaks down. This problem is unlikely to arise in a practical situation, because during the pulse rise time, each successive stage should ionize completely before the relevant saturation intensity is reached. Only in the case of a pulse with a very sharp turn-on would this picture of sequential ionization need to be modified.

The structure in the curves is a result of the ponderomotive potential closing off ionization channels. As an example, consider neutral carbon, which at low intensities is ionized in a three-photon process. The ejected electron must also have sufficient energy to overcome the ponderomotive potential barrier, and if the intensity rises to 6.5×10^{14} W/cm^2, the quiver energy is just large enough to close off the three-photon channel. At this point, the ionization rate suffers a slight drop before the four-photon rate increases and takes over. At higher intensities, further channel closures occur, but these become progressively more difficult to resolve.

4.1.3 Tunnelling Ionization

In the high-intensity limit, where $\gamma \ll 1$, the photon energy is much less than the ionization potential, and this allows the use of an adiabatic approximation. For a static electric field, E, the tunnelling ionization rate for a hydrogen-like potential is given by [98]

$$\mathcal{R}_{st} = 4\,\omega_{at} \left(\frac{\mathcal{E}_i}{\mathcal{E}_h}\right)^{5/2} \frac{E_{at}}{E} \exp\left[-\frac{2}{3}\left(\frac{\mathcal{E}_i}{\mathcal{E}_h}\right)^{3/2} \frac{E_{at}}{E}\right] , \tag{4.7}$$

where $\mathcal{E}_i$ is the ionization potential of the atom or ion concerned, $\mathcal{E}_h$ is the ionization potential for hydrogen (13.6 eV), and ω_{at} and E_{at} are the atomic units for frequency (4.134×10^{16} s^{-1}) and electric field (5.142×10^9 V/cm), respectively.

For an atom or ion in an arbitrary initial state, Eq. (4.7) can be generalized to [99, 100]

$$\mathcal{R}_{st} = \frac{\omega_{at}}{2}\, C_{n^*}^2\, \frac{\mathcal{E}_i}{\mathcal{E}_h}\, \frac{(2l+1)(l+|m|)!}{2^{|m|}(|m|)!(l-|m|)!} \times \left[2\left(\frac{\mathcal{E}_i}{\mathcal{E}_h}\right)^{3/2} \frac{E_{at}}{E}\right]^{2n^*-|m|-1} \exp\left[-\frac{2}{3}\left(\frac{\mathcal{E}_i}{\mathcal{E}_h}\right)^{3/2} \frac{E_{at}}{E}\right] . \tag{4.8}$$

Here l and m are quantum numbers for the initial state, $n^* = Z(\mathcal{E}_h/\mathcal{E}_i)^{1/2}$ is the effective principle quantum number, and $C_{n^*} \simeq (2\varepsilon/n^*)^{n^*}(2\pi n^*)^{-1/2}$ is a constant of order unity. Given that the characteristic atomic frequency is much higher than the laser frequency, Eq. (4.8) can be averaged over an optical cycle to obtain the mean ionization rate in a sinusoidal field,

$$\mathcal{R} = \left[\frac{3}{\pi}\frac{E}{E_{at}}\left(\frac{\mathcal{E}_h}{\mathcal{E}_i}\right)^{3/2}\right]^{1/2} \mathcal{R}_{st} \ . \tag{4.9}$$

A recent series of detailed experiments, measuring the production rates of highly-charges ions in the tunnelling regime [101, 102], have confirmed that the generalized tunnelling formula is in good agreement with observations. Overall, the formula predicts the appearance intensities of various ion stages within a factor of two, and certainly performs better than the Keldysh model for higher charge-states.

Figure 4.2 shows the cycle-averaged tunnelling ionization rates for carbon, calculated using Eq. (4.9), as a function of laser intensity. Compared with the ionization rates in Fig. 4.1 from the Keldysh model, the tunnelling ionization rates are larger at a given intensity and have lower intensity thresholds. As the tunnelling ionization rate depends only on the magnitude of the electric field, there is no dependence on laser wavelength. In addition, there is no structure arising from the closure of ionization channels, because an assumption of the tunnelling model is that the quiver energy is already much larger than the ionization potential.

As in the Keldysh model, an implicit assumption here is that the electric field is small compared with the atomic field,

$$\left(\frac{\mathcal{E}_h}{\mathcal{E}_i}\right)^{3/2} \frac{E}{E_{at}} \ll 1 \ , \tag{4.10}$$

which ensures that the probability of ionization during a laser cycle is considerably less than unity. If this condition is violated, the binding potential is distorted to an extent where the electron can pass freely out of the well, and the problem becomes one of classical over-the-barrier escape rather than quantum-mechanical tunnelling.

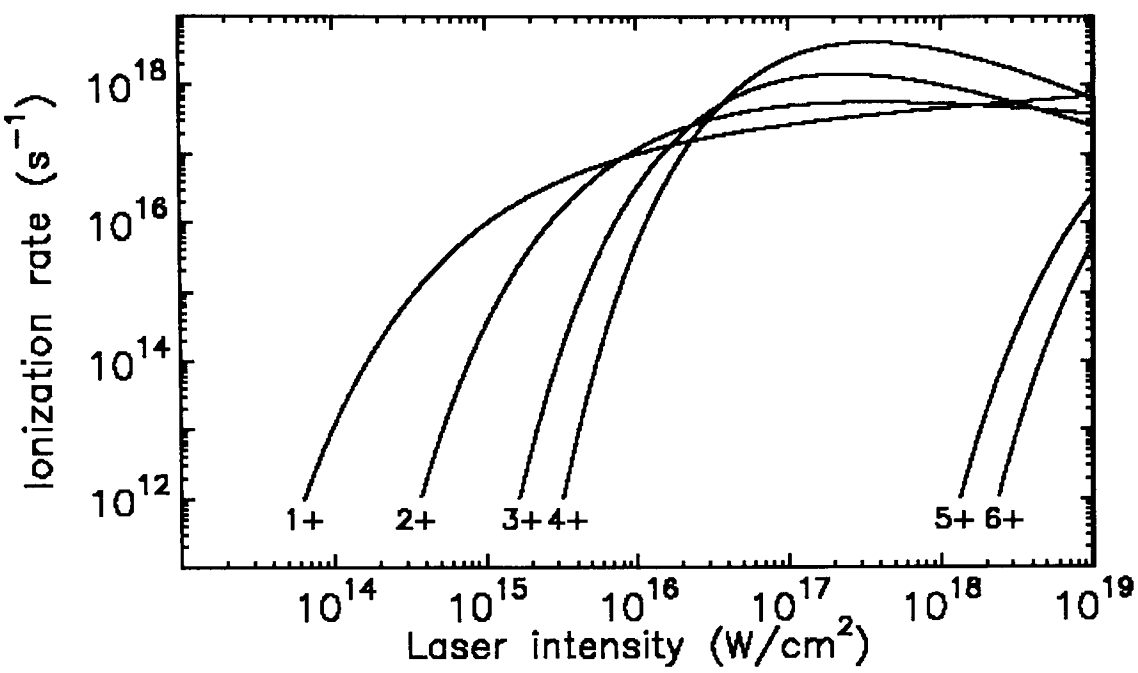

Figure 4.2: Cycle-averaged tunnelling ionization rates for carbon as a function of laser intensity.

4.2 Collisional Ionization

Unless the plasma is so dense that pressure effects must be considered (which typically occurs only in compressed solids), the rate of collisional ionization is given by

$$\mathcal{R}_{coll} = n_e \int v\, f(v)\, \sigma(v)\, dv \tag{4.11}$$

where $f(v)$ is the velocity distribution and $\sigma(v)$ is the velocity-dependent cross-section.

The direct calculation of electron-impact cross-sections is an extensive subject in its own right [103], and in order to obtain an estimate for the collisional ionization rates, a relatively simple binary-encounter approximation will be used. The collision cross-section in this case is given by [104]

$$\sigma(\mathcal{E}) = 4\pi a_0^2 p_i \left(\frac{\mathcal{E}_h}{\mathcal{E}_i}\right)^2 G\left(\frac{\mathcal{E}}{\mathcal{E}_i}\right) , \tag{4.12}$$

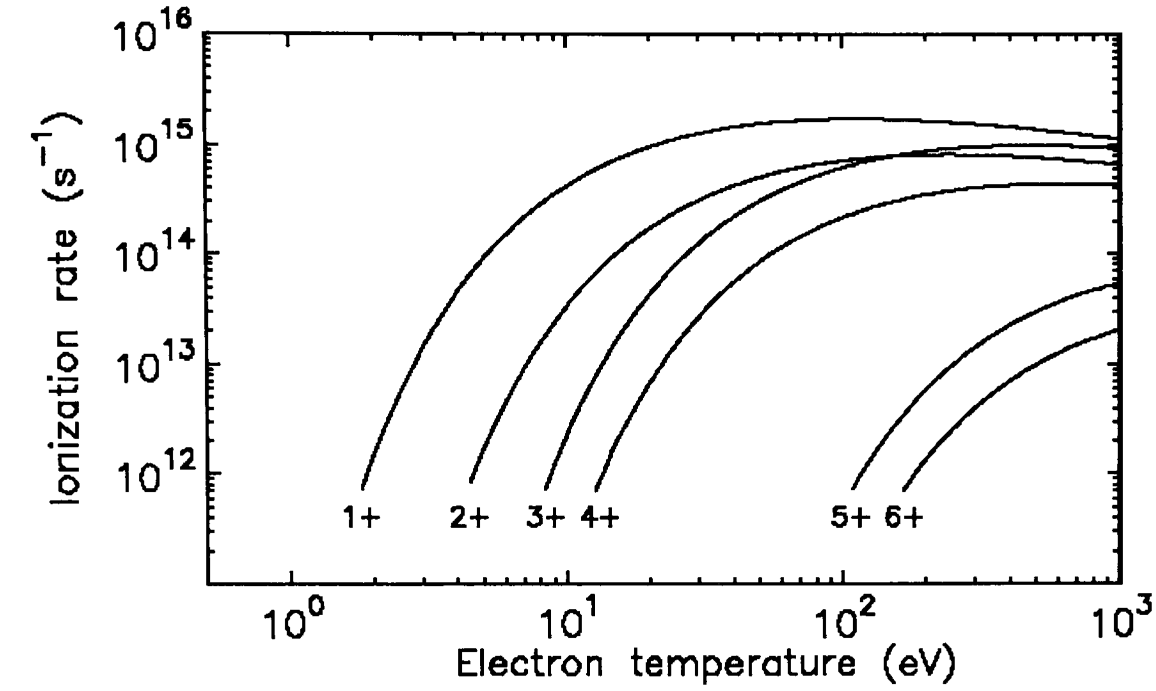

Figure 4.3: Collisional ionization rates for carbon as a function of electron temperature, for a low-density CH_2 plastic.

where

$$G(u) = \frac{1}{u}\left(\frac{u-1}{u+1}\right)^{3/2}\left[1+\frac{2}{3}\left(1-\frac{1}{2u}\right)\ln\left\{2.7+(u-1)^{1/2}\right\}\right] . \tag{4.13}$$

Here a_0 is the Bohr radius for hydrogen and p_i is the number of equivalent electrons in the atomic shell.

Figure 4.3 shows the collisional ionization rates for carbon as a function of electron temperature, assuming a Maxwellian velocity distribution. The electron density for the rate $C^{m+} \rightarrow C^{(m+1)+}$ is taken as $(m+\frac{1}{2})n_0$, where $n_0 = 4\times10^{22}$ cm^{-3}, which is the carbon atom density in a low-density CH_2 plastic.

4.3 A Comparison of Ionization Rates

To assess the relative importance of field-induced and collisional ionization, the tunnelling ionization rates shown in Fig. 4.2 can be compared with the collisional ionization rates shown in Fig. 4.3. It should be noted that the field-induced rates are plotted as a function of laser intensity (and are independent of density), whereas the collisional rates are plotted as a function of density (and, at least to a first approximation, are independent of laser intensity).

Consider the case of an intense femtosecond laser pulse incident on a carbon plastic target. Initially, the target is semi-transparent to the laser radiation, but the formation of an overdense plasma quickly limits the penetration of the laser light. Experiments with 250 fs, 248 nm pulses focused to an intensity of 2.5×10^{15} W/cm^2 on metal targets [7] have measured density gradient scale lengths on the order of 0.05–0.1 λ_0, and for such scale lengths the electric field will be attenuated inside the plasma over a characteristic distance of much less than a laser wavelength. In this case there will only be a narrow layer at the boundary of the plasma within which field-induced effects can contribute to the total ionization.

The significance of field-induced ionization depends strongly on the rise-time of the laser pulse. If the intensity rises rapidly to $\sim 10^{16}$ W/cm^2, for example, while the temperature remains less than $\sim$10 eV, the field-induced ionization rates for producing ionization stages up to C^{4+} will be orders of magnitude larger than the collisional ionization rates. This will result in a highly-ionized skin layer, in front of a region of more weakly-ionized plasma heated by thermal conduction. Once the temperature of the plasma rises above about 100 eV, however, collisional ionization to C^{5+} and C^{6+} can occur, and field-induced ionization cannot compete unless the intensity is above 10^{18} W/cm^2. Thus, at a sufficiently high plasma temperature, field-induced ionization will cease to play an significant role.

An important consideration for a femtosecond-pulse laser-produced plasma is the time required to reach equilibrium. Calculations of the collisional-radiative equilibrium for carbon plasmas [105] show that although a temperature of 25 eV is sufficient to produce a C^{4+} plasma at equilibrium, the time taken to reach equilibrium is about 250 fs. At a temperature of 200 eV, the equilibrium state is fully-stripped C^{6+}, but the time taken to reach equilibrium is on the order of 1 ps. During a femtosecond pulse, an equilibrium state will probably not be reached. For a steeply-rising pulse, field-induced ionization might increase the final ionization stage slightly above that predicted by a standard collisional-radiative model.

It is difficult to make general statements about the overall importance of field-induced ionization without becoming involved in detailed time-dependent modelling. There is a complex interplay between collisional and field-induced processes, particularly at low temperatures. However, it is clear that field-induced ionization would be of fairly limited significance in a femtosecond-pulse solid-density plasma. It would have an increased importance, however, in a lower-density plasma, as the collisional ionization rates are directly proportional to the density. For a longer laser pulse, with a consequently larger region of underdense plasma, field-induced ionization may be more significant, but the intensities required for rapid field-induced ionization cannot currently be produced in laser pulses longer than ~1 ps. In order to reach a situation where field-induced ionization is the dominant mechanism, a much lower initial density is required. In a gas, with $n_e \simeq 10^{-3}\ n_{solid}$, the maximum collisional ionization rate would be $\sim 10^{12}$ s^{-1} (making the ionization time longer than the laser pulse itself), and the collisional heating rate would also be much reduced. In addition, a gaseous plasma would be underdense to the laser radiation, allowing field-induced processes to occur over the entire plasma, rather than only within a narrow skin layer.

Recent experimental and theoretical investigations of gaseous plasmas produced by intense femtosecond laser pulses have discovered some fundamentally new effects: spectral shifts and broadening of the laser pulse due to rapid plasma generation [106]; and an unusually low plasma temperature, which might be used to advantage in recombination x-ray laser schemes [29]. These topics will be discussed in detail in the following two chapters.

Chapter 5

Spectral Shifts and Broadening in an Intense Femtosecond Pulse

During the propagation of an intense femtosecond laser pulse through a plasma, field-induced ionization can cause a rapid increase in the electron density, which results in a decrease in the refractive index and has a feedback effect on the pulse propagation. This plasma-induced self-phase modulation leads to effects both in the spatial domain (defocusing) and in the frequency domain (spectral broadening). In a solid-density plasma, the effects are difficult to observe clearly, firstly because field-induced ionization competes with collisional ionization, secondly because the plasma becomes overdense and reflects a large fraction of the radiation, and lastly due to the plasma expansion. If, however, an intense laser pulse is focused through a gas cell or into a gas jet, the geometry is more tightly controlled, and the density is also sufficiently low to ensure that field-induced ionization is the dominant process.

In this chapter, the effect of field-induced ionization on the spectrum of a femtosecond laser pulse propagating through a plasma will be investigated. Initially, a variety of mechanisms for producing spectral shifts and broadening, including plasma generation, will be described. A simple theoretical model for plasma-induced shifts will be outlined, in which propagation effects are neglected. The pulse propagation will then be included, by coupling Maxwell's equations to the ionization rate equations, and the propagation model will be used to make predictions about plasma-induced spectral shifts under a wide range of conditions. The result of averaging over the focusing geometry will be discussed, and predictions from the model will be compared with experimental results in the literature.

5.1 Mechanisms for Spectral Modification

An excellent review of self-phase modulation and continuum generation has recently been published [107], but this unfortunately excludes plasma generation. Continuum generation was first observed by Alfano and Shapiro [108] in 1970, using picosecond laser pulses and various crystal and glass targets. The phenomenon was associated with the onset of beam filamentation, and the localized intensity in the filaments was estimated at around 10^{13} W/cm^2, which is below the threshold for plasma formation. The spectral broadening was attributed to an intensity-dependent refractive index caused by electronic distortion. This is a third-order nonlinearity, for which the additional term in the refractive index is proportional to the product of $\langle E^2 \rangle$ and the third-order nonlinear susceptibility, $\chi^{(3)}$.

During the rising edge of the laser pulse, the $\chi^{(3)}$ nonlinearity results in an increasing refractive index and a negative frequency shift of the laser light (towards the red); during the trailing edge of the pulse, the refractive index decreases and there is a positive frequency shift (towards the blue). The overall broadening is roughly symmetrical about the incident frequency, producing a quasi-continuum. In the early experiments, emission was seen over the entire visible spectrum. More recently, spectral broadening has been observed using femtosecond pulses, and a pump-probe experiment has clearly shown the time-dependent behaviour of the frequency shift [109]. In some cases, a slight asymmetry has been observed in the spectrum favouring the blue-shifted side, and theoretical models have attributed this to a distortion of the pulse shape as the pulse propagates through the nonlinear medium [110, 111].

If the laser intensity is relatively low and the interaction length is very large, as in transmission through an optical fibre, very clean self-phase modulated pulses can be obtained [112]. However, in experiments with tightly-focused pulses other effects become important, such as parametric four-photon coupling [113]. In the basic four-photon process, two incident laser photons are transformed into a frequency-shifted photon pair, with conservation of energy, $2\omega_0 = \omega_i + \omega_j$, and momentum,

$2\mathbf{k}_0 = \mathbf{k}_i + \mathbf{k}_j$. The main experimental evidence for parametric processes is a spectral and angular correlation observed in the transmitted laser light. There is, however, a complex relationship between the fundamental $\chi^{(3)}$ nonlinearity and the parametric process, and there has been considerable debate over which mechanism dominates in a given situation [114].

Gases are unlikely candidates for continuum generation, as they have a much smaller $\chi^{(3)}$ nonlinearity. However, above a certain intensity threshold, continuum generation has been observed in high-pressure rare gases [115, 116, 117]. The mechanism responsible is still rather uncertain: it does not involve free electrons, as the laser intensity is below that required for plasma formation, but the shifts are much larger than expected from a simple analysis. A partial theory proposed by Strickland and Corkum [118] stresses the proper treatment of self-focusing in the limit where the beam diameter is larger than the pulse length. This theory predicts the formation of transient temporal microstructures in the gas, and the continuum generated by these structures matches the experimental observations, at least in a qualitative way. An alternative explanation involves the excitation of a coherent set of Rydberg levels in the neutral atoms [119].

At laser intensities well above the self-focusing threshold, self-phase modulation is dominated by the production of free electrons through field-induced and avalanche collisional ionization. This effect was predicted by Bloembergen [120] in 1973, and observed soon afterwards by Yablonovitch [121, 122, 123] in high-pressure gases using nanosecond laser pulses at 10.6 μm. With infrared radiation, the plasma rapidly becomes overdense, and only a narrow spike from the leading edge of the laser pulse is transmitted. The spectrum of the transmitted pulse shows a narrow, symmetrical broadening, consistent with a step-like fall in amplitude due to the plasma growth. In recent years, similar experiments have been performed by Downer *et al.* [106, 124, 125, 126, 127, 128] using femtosecond laser pulses at 620 nm. At optical wavelengths, the gaseous plasma is underdense and the laser pulse is largely transmitted, but a blue shift is observed arising from the plasma formation. The origin of the one-sided broadening can be seen in the collisionless expression for the plasma refractive index,

$$\eta = (1 - n_e/n_{cr})^{1/2} . \tag{5.1}$$

where n_e is the electron density and $n_{cr} = (\epsilon_0 m_e \omega_0^2/e^2)$ is the critical density. The increase in electron density during the laser pulse causes a negative change in the refractive index, which decreases the optical path length through the plasma and hence causes a blue shift of the light. As recombination occurs on a much slower time scale, there is no corresponding red shift in the trailing edge of the pulse. This differs from the usual $\chi^{(3)}$ electronic nonlinearity, for which nearly-symmetrical broadening is observed. In addition, the frequency shift during the rising edge of the pulse is in the opposite direction, which, in a pump-probe experiment, provides a means of distinguishing the two mechanisms.

5.2 Homogeneous Plasma Model

In the past, a homogeneous plasma model (also called a Drude model) has been used to analyse plasma-induced spectral shifts [123, 125]. In this model it is assumed that the entire plasma can be described by a single value of refractive index. For a monochromatic incident beam of wavelength λ_0, and an interaction length L, the wavelength shift is given by

$$\Delta = \frac{\lambda_0 L}{c}\frac{d\eta}{dt} . \tag{5.2}$$

The plasma refractive index, including collisions, can be written

$$\eta = \left(1 - \frac{n_e/n_{cr}}{1 + i\nu_{ei}/\omega_0}\right)^{1/2} , \tag{5.3}$$

where ν_{ei} is the electron-ion collision frequency. Making the reasonable assumptions for gaseous densities that $\nu_{ei} \ll \omega_0$ and $n_e \ll n_{cr}$, Eq. (5.3) can be substituted into Eq. (5.2) to obtain

$$\Delta = -\frac{e^2 L \lambda_0^3}{8\pi^2 \epsilon_0 m_e c^3}\frac{dn_e}{dt} . \tag{5.4}$$

Table 5.1: Ionization potentials for the first ten ionization stages of argon and neon.

ionization stage	ionization potential (eV)	
	argon	neon
I	15.8	21.6
II	27.6	41.0
III	40.7	63.5
IV	59.8	97.1
V	75.0	126.2
VI	91.0	157.9
VII	124.3	207.3
VIII	143.5	239.1
IX	422.5	1195.9
X	478.7	1362.2

For high-intensity laser pulses, ionization can be modelled using the generalized tunnelling formula discussed in Chapter 4. The cycle-averaged ionization rate is given by

$$\begin{aligned} \mathcal{R} &= \frac{\omega_{at}}{2} C_{n^*}^2 \frac{\mathcal{E}_i}{\mathcal{E}_h} \left[\frac{3}{\pi}\frac{E}{E_{at}}\left(\frac{\mathcal{E}_h}{\mathcal{E}_i}\right)^{3/2}\right]^{1/2} \frac{(2l+1)(l+|m|)!}{2^{|m|}(|m|)!(l-|m|)!} \\ &\times \left[2\left(\frac{\mathcal{E}_i}{\mathcal{E}_h}\right)^{3/2}\frac{E_{at}}{E}\right]^{2n^*-|m|-1} \exp\left[-\frac{2}{3}\left(\frac{\mathcal{E}_i}{\mathcal{E}_h}\right)^{3/2}\frac{E_{at}}{E}\right] . \end{aligned} \tag{5.5}$$

Here E is the electric field, $\mathcal{E}_i$ is the ionization potential for the atom or ion concerned, $\mathcal{E}_h$ is the ionization potential for hydrogen, ω_{at} and E_{at} are the atomic units for frequency and electric field, respectively, l and m are quantum numbers for the initial state, n^* is the effective principle quantum number and C_{n^*} is a constant of order unity [99]. The ionization potentials for the first ten stages of argon and neon, taken from Ref. [129], are listed in Table 5.1.

The ions are assumed to be in their ground states, and only sequential ionization processes are considered. This approximation has been shown to be valid in recent experiments on field-induced ionization at high intensities [80]. Using Eq. (5.5), the time-dependent populations of the various ionization stages can be obtained from a set of coupled differential equations,

$$\left.\begin{aligned}\frac{dn_0}{dt} &= -\mathcal{R}_0 n_0 \\ \frac{dn_1}{dt} &= -\mathcal{R}_1 n_1 + \mathcal{R}_0 n_0 \\ \frac{dn_2}{dt} &= -\mathcal{R}_2 n_2 + \mathcal{R}_1 n_1 \\ &\vdots \\ \frac{dn_m}{dt} &= -\mathcal{R}_m n_m + \mathcal{R}_{m-1} n_{m-1}\end{aligned}\right\} \tag{5.6}$$

where n_0 denotes the density of neutral atoms, n_1 the density of singly-ionized atoms, and so on, up to some maximum ionization stage, m. Using the known pulse envelope, the time-dependent electron density can be determined from the solution of this set of equations, and Eq. (5.4) then gives the time-dependent wavelength shift.

As an example, the time-dependent wavelength shift will be calculated for a 620 nm, 100 cycle laser pulse with a sine-squared field envelope (FWHM 75 fs) and peak intensity 10^{16} W/cm^2, propagating through a 50 λ_0 (30 μm) length of 5 atm argon gas. Figure 5.1 shows the relative populations of the neutral atom and the first six ionization stages as functions of time. Successively higher ionization stages appear as the intensity rises during the leading edge of the pulse, but after the peak intensity has been reached there is very little change in the relative populations.

Figure 5.2 shows the degree of ionization, and the wavelength shift calculated from Eq. (5.4), as functions of time. The degree of ionization increases in a series of steps as the threshold intensities for the successive stages are reached, and peaks in the wavelength shift correspond to these steps.

Transforming the time-dependent wavelength shift in Fig. 5.2 into a transmitted pulse spectrum is not, however, a trivial task. In the simplest interpretation, a number of peaks in the spectrum would be expected, each spectrally-shifted peak corresponding to a peak in Fig. 5.2. In the case of a femtosecond pulse, there are a

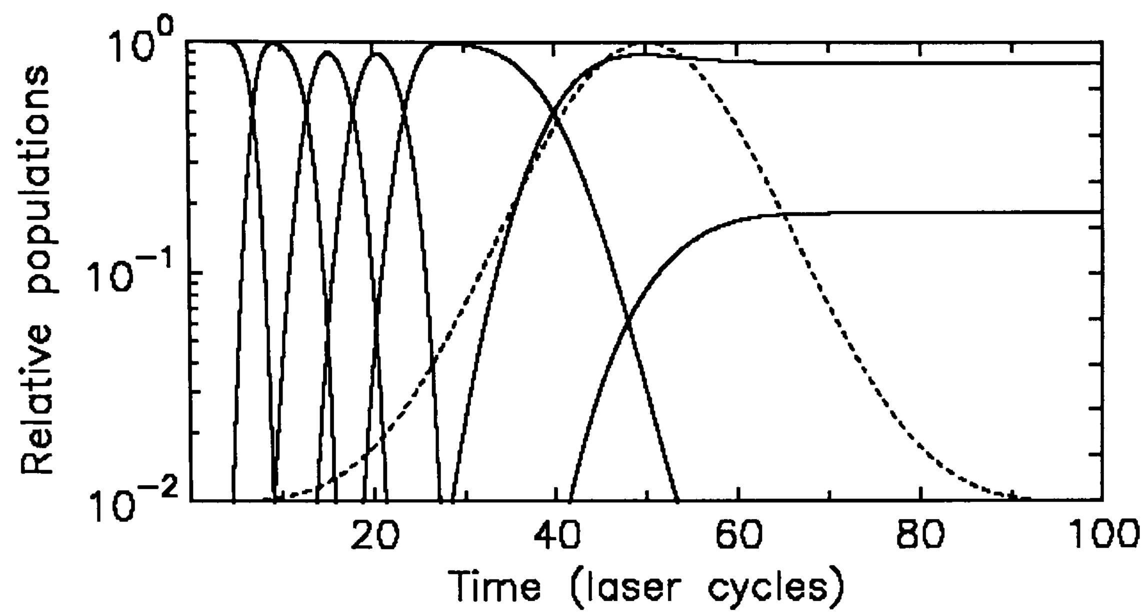

Figure 5.1: Relative populations of the neutral atom and the first six ionization stages of argon as a function of time, for a 620 nm, 100 cycle laser pulse at an intensity of 10^{16} W/cm^2. The populations are shown as solid lines, and the intensity envelope of the laser pulse as a dotted line.

number of problems with this approach. Firstly, the incident pulse is not monochromatic and consists of spread of wavelengths. Secondly, and more importantly, the ionization occurs rapidly compared with the duration of the laser pulse. The peaks associated with the first few ionization stages in Fig. 5.2 correspond to extremely large wavelength shifts (up to 300 nm), but as the peaks only have widths on the order of a few femtoseconds, distinct shifted features would not be expected in the transmitted pulse spectrum. Lastly, only a small fraction of the pulse energy is in the rising edge, where the most rapid ionization occurs, and the slower ionization rate near the peak of the laser pulse is more likely to be important in determining the main features of the transmitted spectrum.

A first-order approximation to the transmitted spectrum can be obtained by assuming that the ionization occurs slowly compared to the propagation time through the plasma. In this case, the major contribution to the transmitted pulse spectrum at wavelength λ comes from the point in time when $\lambda = \lambda_0 + \Delta(t)$. Denoting the initial pulse spectrum by $f_0(\lambda)$, the transmitted spectrum in this approximation can be written

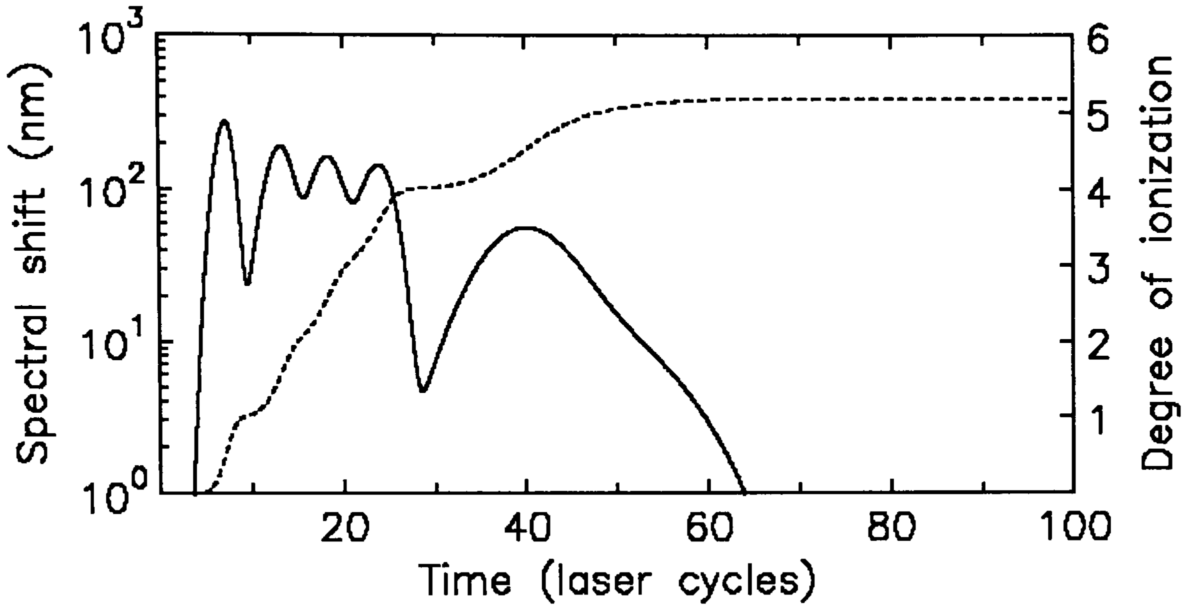

Figure 5.2: Average degree of ionization (dotted line) and spectral shift (solid line) for a 620 nm, 100 cycle, 10^{16} W/cm^2 laser pulse and 50 λ_0 of 5 atm argon.

$$f(\lambda) = \frac{1}{\tau} \int \int \delta(\lambda - \Delta(t) - \lambda') \, f_0(\lambda') \, d\lambda' \, dt \ , \tag{5.7}$$

where τ is the pulse duration. For the example above, the transmitted pulse spectrum is shown in Fig. 5.3, together with the initial pulse spectrum for comparison. The two curves have been normalized to the same peak height. The maximum wavelength shift is several hundred nanometres, and does not fit on the scale here, but the shifted peak near 570 nm, for example, is clearly identifiable with the peak in $\Delta(t)$ occurring about 40 laser cycles into the pulse. A significant fraction of the pulse energy in the trailing edge is unshifted in wavelength, because the ionization rate following the peak of the pulse is close to zero.

Despite the problems associated with obtaining a shifted spectrum, the homogeneous plasma model has been used by Downer *et al.* [125] to fit experimental spectra for an intense femtosecond laser pulse propagating through a gaseous plasma. The exact procedure employed is not clear. After calculating the time-dependent wavelength shift, "an integration over the Gaussian spatial profile corresponding to the experimental focal geometry [was] performed in order to compute a spatially and temporally averaged spectral shift." The agreement between the experimental

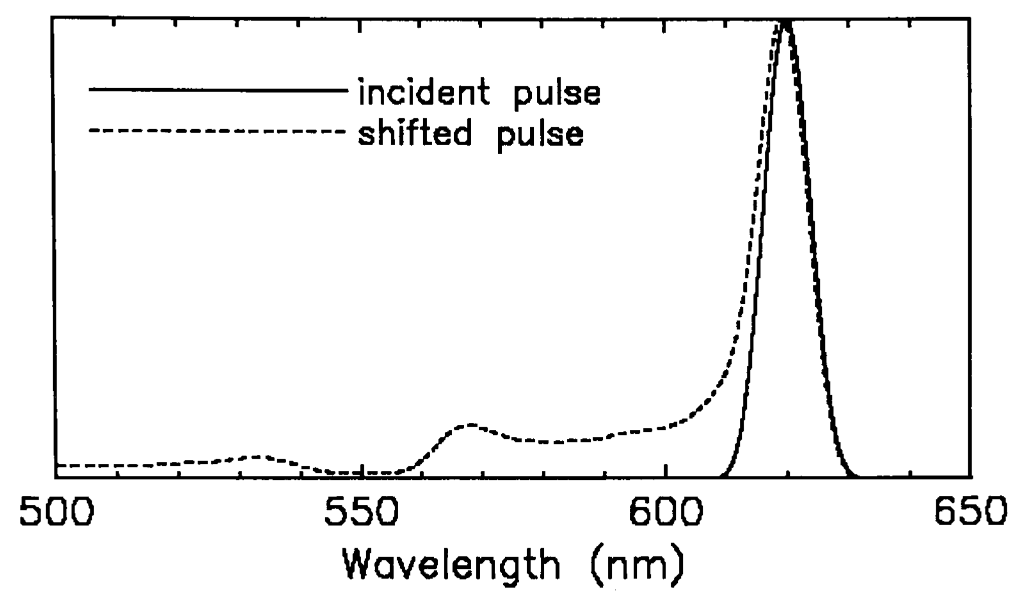

Figure 5.3: Initial pulse spectrum (solid line) and transmitted pulse spectrum (dotted line) from the homogeneous plasma model, for a 620 nm, 100 cycle, 10^{16} W/cm^2 laser pulse and 50 λ_0 of 5 atm argon.

and theoretical spectrum in the case of a neon plasma was quite acceptable, but the procedure failed to match the observed spectrum for argon, which at intensities $\gtrsim 10^{16}$ W/cm^2 was broader and shifted ~10 nm further to the blue than the theoretical prediction. This anomalous broadening in argon was attributed to additional ionization caused by electron-ion collisions. However, some of the disagreement may be due instead to the use of an oversimplified plasma model. This question will be discussed more fully in a later section, after the results from an improved theoretical model, incorporating propagation effects, have been presented.

5.3 Pulse Propagation Model

In this more detailed model, the plasma is extended in one dimension, and the coupled set of rate equations is solved at each point in the plasma. Simultaneously, Maxwell's equations are solved for the propagation of a linearly-polarized laser pulse through the plasma. Ionization is calculated using the instantaneous value of the electric field rather than using a cycle-averaged value. Ionization occurs predominantly near the laser cycle peaks, where the electric field is a maximum and the quiver velocity of the free electrons is instantaneously zero. An additional electron ionized at this point remains in phase with the bulk free electrons, and there is no additional absorption of energy. However, an electron ionized at a time slightly offset from the peak of the electric field acquires a dephasing energy, which will remain as residual kinetic energy once the pulse has passed. The dephasing energy, which is the classical equivalent of above-threshold-ionization (ATI) energy [29], is generally small and has a minimal effect on the spectral properties of the transmitted pulse. However, it is important in determining the final temperature of the plasma, which is a topic will be addressed in greater detail in Chapter 6.

In the one-dimensional case, a transverse electromagnetic pulse propagating along the x-axis obeys a time-dependent wave equation,

$$\frac{\partial^2 E}{\partial x^2} - \frac{1}{c^2}\frac{\partial^2 E}{\partial t^2} - \mu_0 \frac{\partial J}{\partial t} = 0 \; , \tag{5.8}$$

where J is the total plasma current. The current can be calculated from an electron distribution function, $f(x, v, t)$, with the addition of a term to ensure energy conservation during ionization,

$$J = -e \int f(x, v, t) \; v \; dv \;\; + J_{ioniz} \; . \tag{5.9}$$

The ionization current, J_{ioniz}, is obtained by equating the energy loss through ionization to the Joule heating,

$$E \cdot J_{ioniz} = \sum_{k=1}^{m} \mathcal{R}_k n_k \mathcal{E}_k \; . \tag{5.10}$$

The equation of motion for the electron distribution function,

$$\frac{\partial f}{\partial t} - \frac{eE}{m_e}\frac{\partial f}{\partial v} = \sum_{k=1}^{m} \mathcal{R}_k n_k \; , \tag{5.11}$$

must be solved simultaneously with the wave equation.

The entire system of equations, consisting of Eqs. (5.8)–(5.11), can be solved using an explicit finite-difference method [130]. This requires x and v to be partitioned into meshes of spacing Δx and Δv, and the electric field to be evaluated at fixed time increments Δt. For numerical stability, the method requires that $c\Delta t \leq \Delta x$. Typically, $\Delta x = \lambda_0/25$, and $\Delta t = \tau_0/50$, where λ_0 is the vacuum laser wavelength and τ_0 is the laser cycle time. The velocity mesh spacing determines the accuracy to which the dephasing energy is calculated. Where the emphasis is on the spectrum of the transmitted pulse, accuracy in calculating the dephasing energy can be sacrificed to increase the computational speed, and the velocity mesh can be reduced to a single cell. This effectively makes the assumption that all the electrons move at the same velocity. Such a simplification makes a negligible difference to the transmitted pulse spectrum for the parameters used in this chapter. In Chapter 6, however, where the plasma properties are of primary interest, an accurate calculation of the dephasing energy is required, and there a fine velocity mesh will be used.

Using a computer program written in FORTRAN 77, a simulation run for a 100 cycle laser pulse and a 50 λ_0 length of gas required approximately 30 minutes of CPU time on a Convex C220 vector processor. Coarser step sizes can be used to increase the speed, but at the expense of overall accuracy. The typical parameters quoted above result in energy conservation within about 1%.

5.4 Simulation Results

In this section, a variety of simulated spectra will be presented. The effects of laser intensity, laser pulse length and plasma interaction length on the transmitted pulse spectrum will be investigated, and results will be given for simulations using two pulses: an intense pump pulse and a weak, delayed probe pulse. The importance of collisional ionization will be investigated, and spectra averaged over the focusing geometry will be presented for comparison with experimental results.

The simulations are performed for a laser wavelength of 620 nm, which is the wavelength used in recent experiments by Downer *et al.* [125]. The laser pulses have a sine-squared field envelope, and the neutral gas density is apodized slightly to minimize the reflections which occur when the plasma is perfectly square-sided.

5.4.1 Comparison with the Homogeneous Model

In Sec. 5.2, a transmitted pulse spectrum was calculated using the homogeneous model, for a 620 nm, 100 cycle laser pulse (FWHM 75 fs) with a peak intensity of 10^{16} W/cm^2 and a 50 λ_0 (30 μm) length of 5 atm argon gas. Figure 5.4 compares that spectrum with one obtained from the propagation model under exactly the same conditions. There are significant differences between the two results. The homogeneous model underestimates the intensity of the features at small blue shifts and overestimates the intensity at large blue shifts, because it fails to correctly account for the distribution of energy within the pulse. Features at small blue shifts are associated with relatively slow ionization near the peak of the laser pulse, and these features should be much more significant than those at large blue shifts which are associated with rapid ionization in the leading edge of the pulse. The propagation model includes such energy balancing automatically.

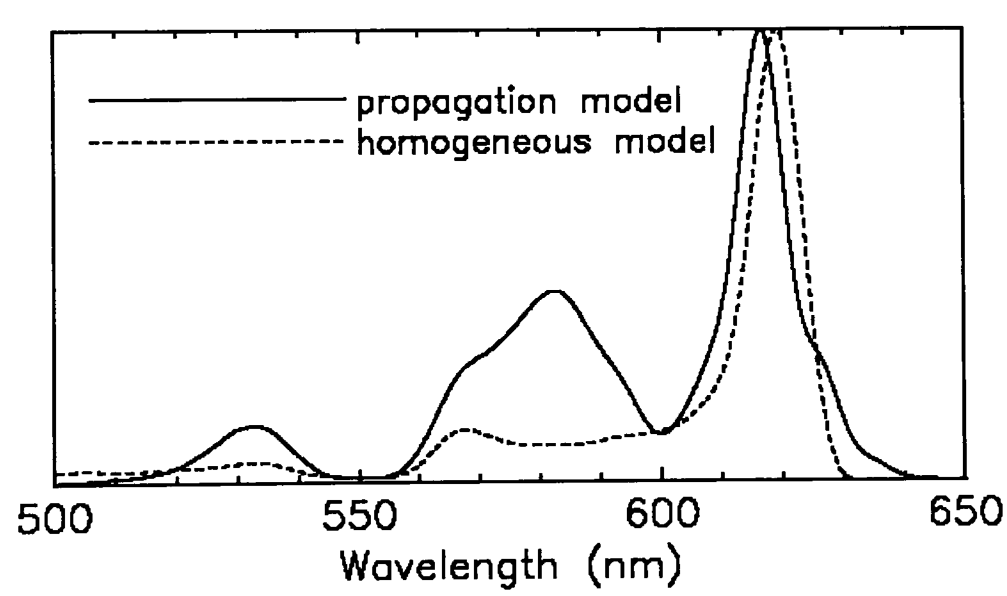

Figure 5.4: Comparison of transmitted pulse spectra from the homogeneous model and the pulse propagation model, for a 620 nm, 100 cycle, 10^{16} W/cm^2 laser pulse and 50 λ_0 of 5 atm argon. The spectra have been normalized to the same peak height.

5.4.2 Dependence on Laser Intensity

Figure 5.5 shows the transmitted pulse spectra and the average degree of ionization for a 620 nm, 100 cycle laser pulse and a 50 λ_0 length of 5 atm argon gas, at a number of intensities in the range 10^{15}–10^{16} W/cm^2. The spectra have all been normalized to the same peak height.

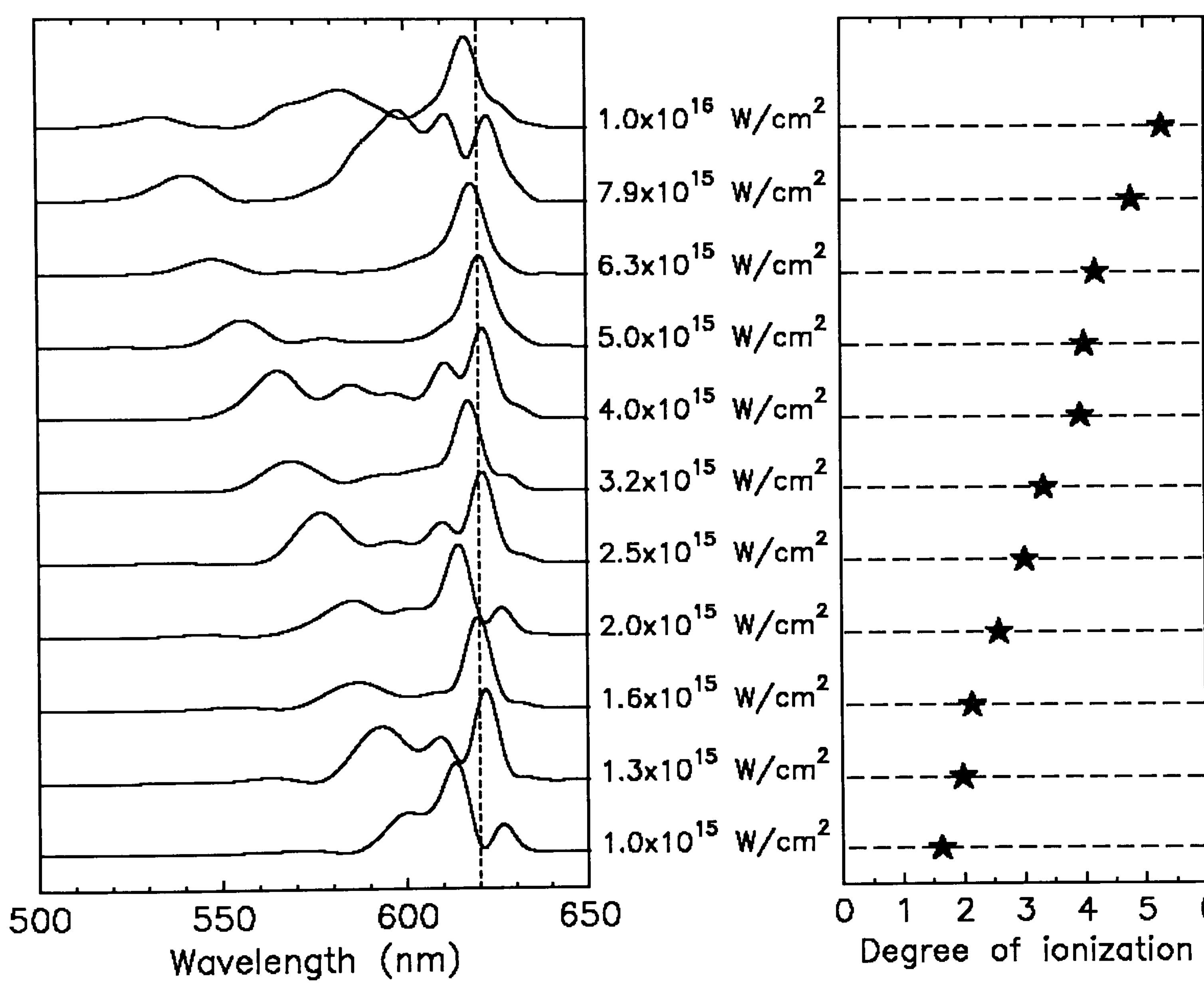

Figure 5.5: Transmitted spectra and degree of ionization for a 620 nm, 100 cycle laser pulse and 50 λ_0 of 5 atm argon.

The peak laser intensity determines the highest ionization stage which is reached during the pulse. The degree of ionization varies from 1.59 at 10^{15} W/cm^2

to 5.29 at 10^{16} W/cm^2. As the intensity increases, more features appear on the blue-shifted side of the main peak, and the maximum blue shift increases. At the highest intensity, the maximum blue shift is almost 100 nm. In each case, however, a large fraction of the pulse energy is transmitted essentially unshifted in wavelength, and this corresponds to the trailing edge of the pulse, which causes no additional ionization and experiences a constant refractive index. There is no simple correlation between the number of subsidiary peaks in the shifted spectrum and the degree of ionization, as there was in the homogeneous plasma model considered previously, and it is sometimes difficult to identify the origin of certain features. Nevertheless, some clearly-resolved features in the shifted spectrum probably do correspond to characteristic ionization rates in the plasma. There are no significant red-shifted features, and what appears as a red-shifted peak in the spectrum for 10^{15} W/cm^2, for example, is in fact the unshifted wing of the initial spectrum, amplified by the normalization process.

It should be noted that the production of such spectra does not appear to require a large fraction of the pulse energy to be converted into ionization. The largest fractional energy absorption for the spectra shown in Fig. 5.5 is 2.4% at 2.0×10^{15} W/cm^2. As the pulse does not lose a significant amount of energy in propagation, the degree of ionization is almost constant across the plasma.

The corresponding transmitted pulse spectra for the case of a neon plasma are shown in Fig. 5.6. Here the degree of ionization is considerably lower, only reaching 2.53 at 10^{16} W/cm^2. There is less detail in the shifted spectra, and the maximum blue shift is considerably smaller. The two neon spectra which show the greatest detail, at 1.0×10^{15} and 5.0×10^{15} W/cm^2, seem to be associated with the production of a new ionization stage, which shows that ionization occurring slowly across the peak of the pulse can generate prominent features at small blue shifts. At an intensity of 2.5×10^{15} W/cm^2, where almost no significant blue shifted features are seen, ionization of the first stage occurs in the early leading edge of the pulse, and the ionization rate near the peak of the pulse is close to zero.

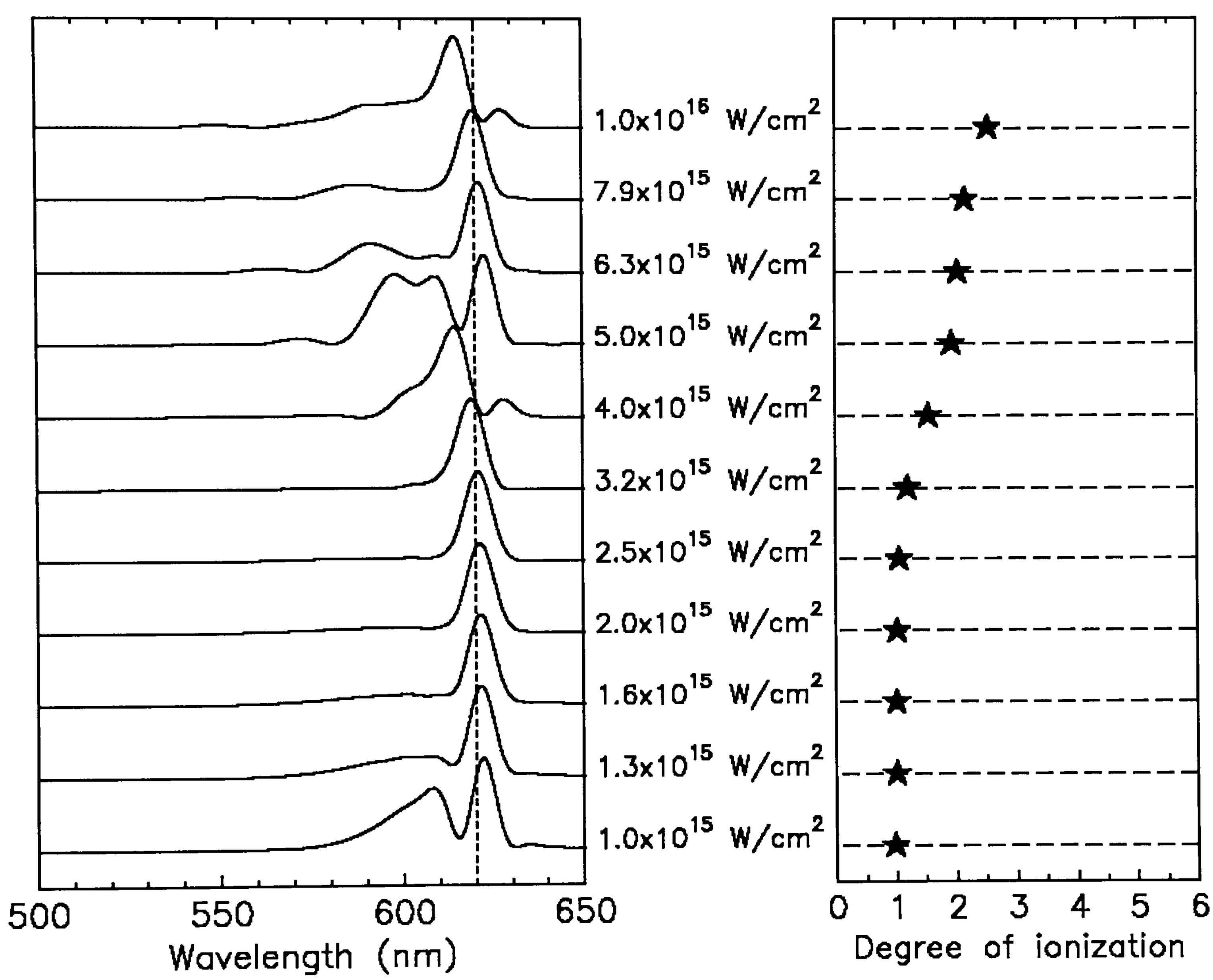

Figure 5.6: Transmitted spectra and degree of ionization for a 620 nm, 100 cycle laser pulse and 50 λ_0 of 5 atm neon.

5.4.3 Dependence on Plasma Length, Gas Pressure and Laser Pulse Duration

In the homogeneous plasma model, the wavelength shift is directly proportional to the interaction length, which suggests that the blue shift should scale linearly with the length of the plasma. Figure 5.7 shows a number of spectra calculated for a 620 nm, 100 cycle laser pulse and a varying length of 5 atm argon. Although the maximum blue shift does increase for a larger interaction distance, the change is not simply an expansion along the wavelength axis; considerable extra detail is introduced as well. As in the previous cases, a large fraction of the initial pulse energy remains unshifted in wavelength.

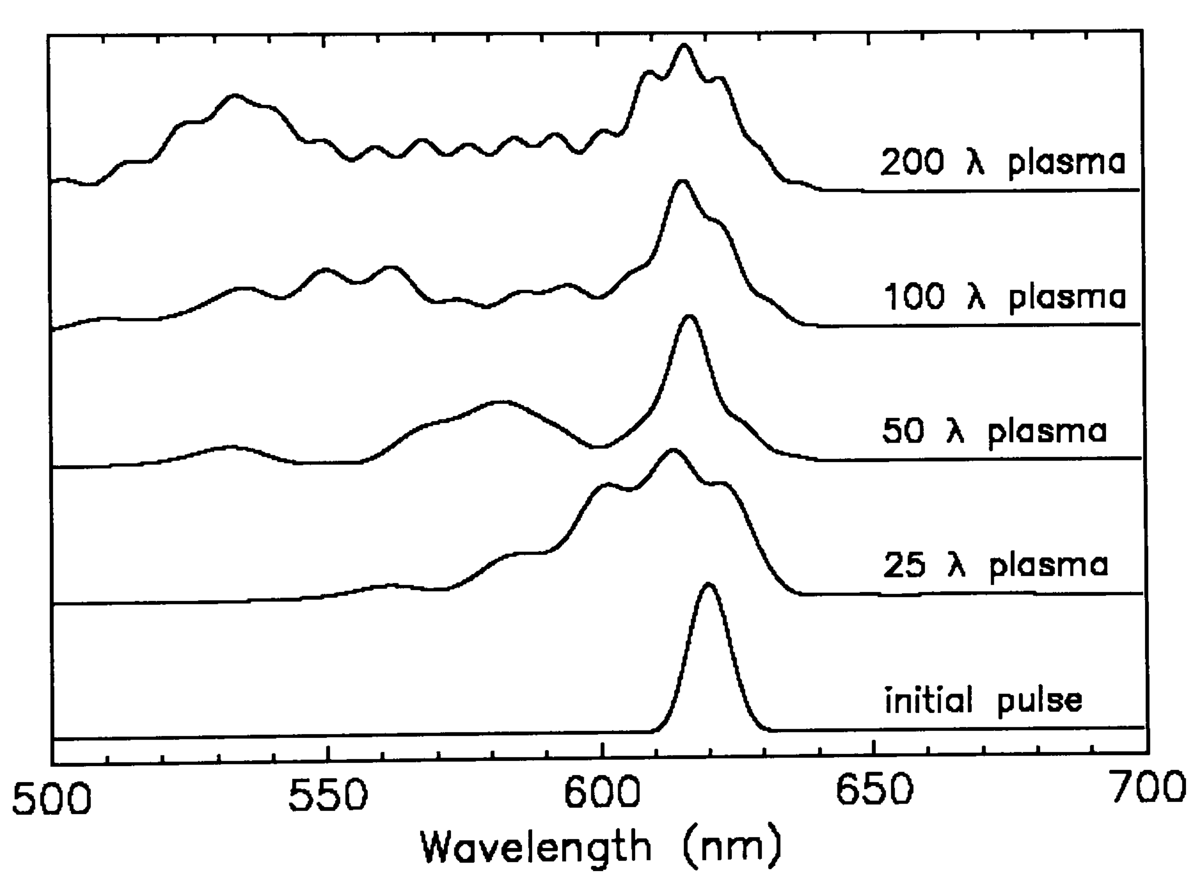

Figure 5.7: Effect of plasma length on the transmitted spectrum, for a 620 nm, 100 cycle, 10^{16} W/cm^2 laser pulse and 5 atm argon.

The modulation observed in the case of a 200 λ_0 plasma is due to a modification of the pulse envelope. This is clearly shown in Fig 5.8, where the electric field in the transmitted pulse is plotted as a function of time. The initial pulse has a sine-

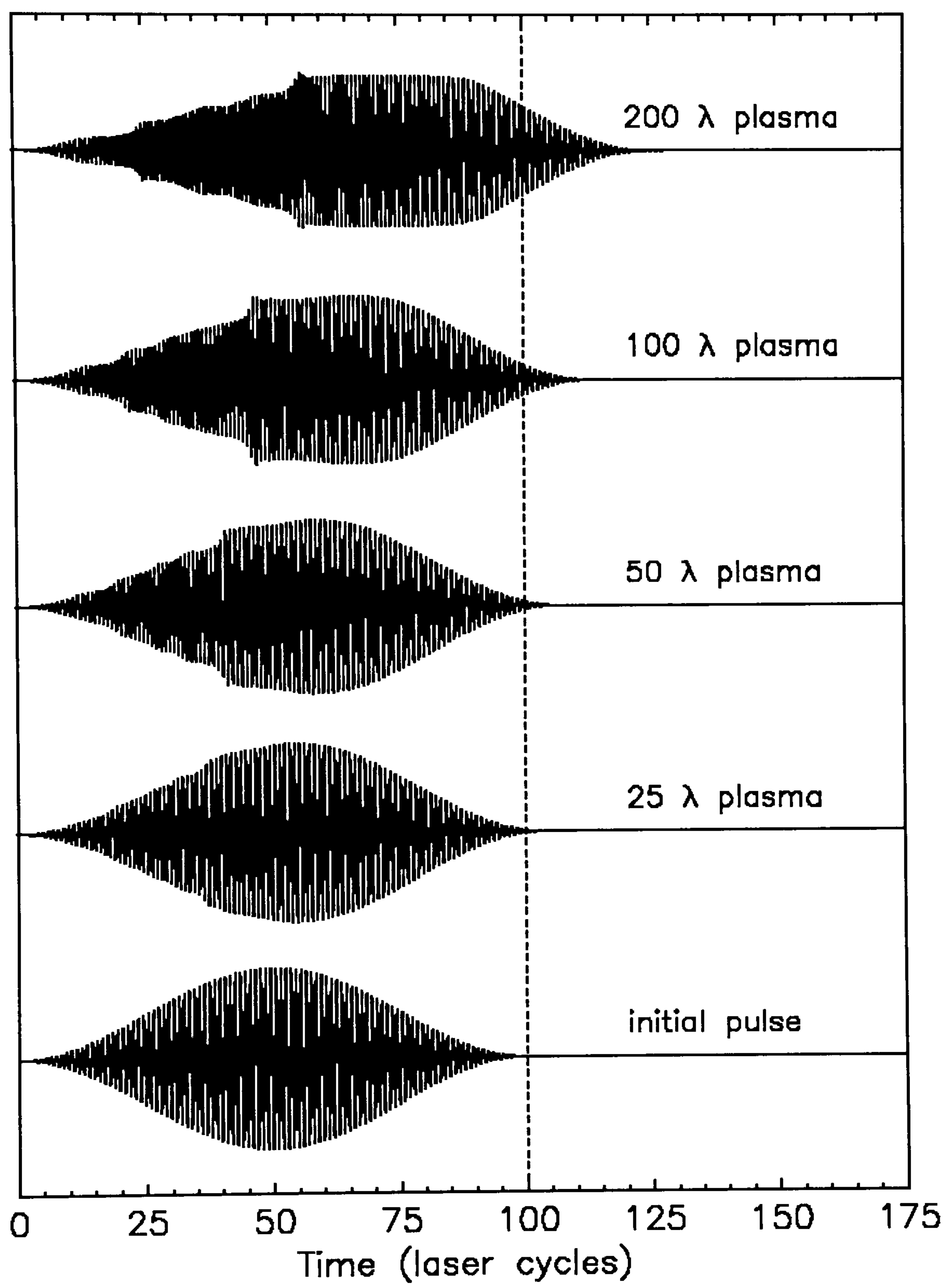

Figure 5.8: Electric field as a function of time for a 620 nm, 100 cycle, 10^{16} W/cm^2 laser pulse and 5 atm argon.

squared envelope and is 100 cycles long. As the length of plasma increases, step-like features gradually develop on the leading edge of the pulse (associated with the critical intensities for the various ionization stages), and the pulse is also stretched in time.

The pattern of solid black areas within the pulse envelope is caused by the limited resolution of the printer which was used to generate the figure, but it gives a convenient visual indication of the blue shift. In the initial pulse the pattern is uniform across the entire envelope, but for long lengths of plasma an increasing proportion of solid black in the leading edge clearly shows the blue shift. The pattern in the trailing edge is almost the same in every case, which shows that this part of the pulse is transmitted unshifted in wavelength.

As the length of plasma increases, a larger fraction of the pulse energy is converted to ionization, and the peak pulse intensity and the degree of ionization decrease across the plasma. This effect is almost negligible for a 25 λ_0 plasma, but for a 200 λ_0 plasma the degree of ionization decreases from 5.40 at the front to 4.64 at the rear boundary.

Another prediction of the homogeneous model is that the transmitted pulse spectrum should remain unchanged for a constant product of gas pressure and interaction length. Figure 5.9 compares several spectra for a 620 nm, 100 cycle, 10^{16} W/cm^2 pulse and a pressure-length product of 250 atm-λ_0. At low gas pressures, the shifted spectra are almost identical, but as the pressure increases, the maximum blue shift increases slightly and additional features are observed. This change at high pressure arises because the electron density is no longer small compared to the critical density (an assumption of the homogeneous model). For 620 nm light, the critical density is 2.9×10^{21} cm^{-3}, and in the case of the spectrum at 10 atm, the electron density is 1.4×10^{21} cm^{-3}, nearly half the critical density.

The transmitted pulse spectrum also depends on the duration of the incident pulse. Figure 5.10 shows the transmitted spectra for a 620 nm, 10^{16} W/cm^2 pulse of varying length and 50 λ_0 of 5 atm argon. The longest pulse, 200 cycles, corresponds to a FWHM of 150 fs. As the pulse becomes shorter the blue shift increases, because the intermediate ionization stages survive to higher intensities and are thus ionized at a faster rate. The main effect is simply an expansion of the shifted features towards

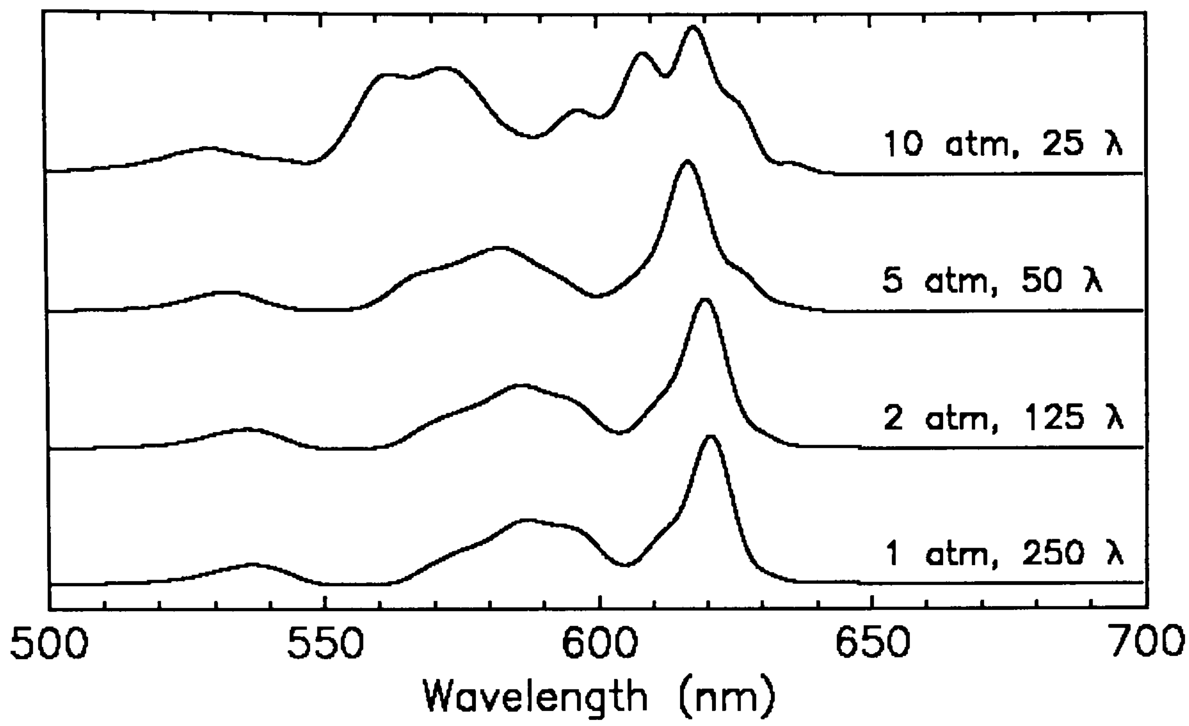

Figure 5.9: Comparison of transmitted spectra for a 620 nm, 100 cycle, 10^{16} W/cm^2 laser pulse and a constant pressure-length product of 250 atm-λ_0.

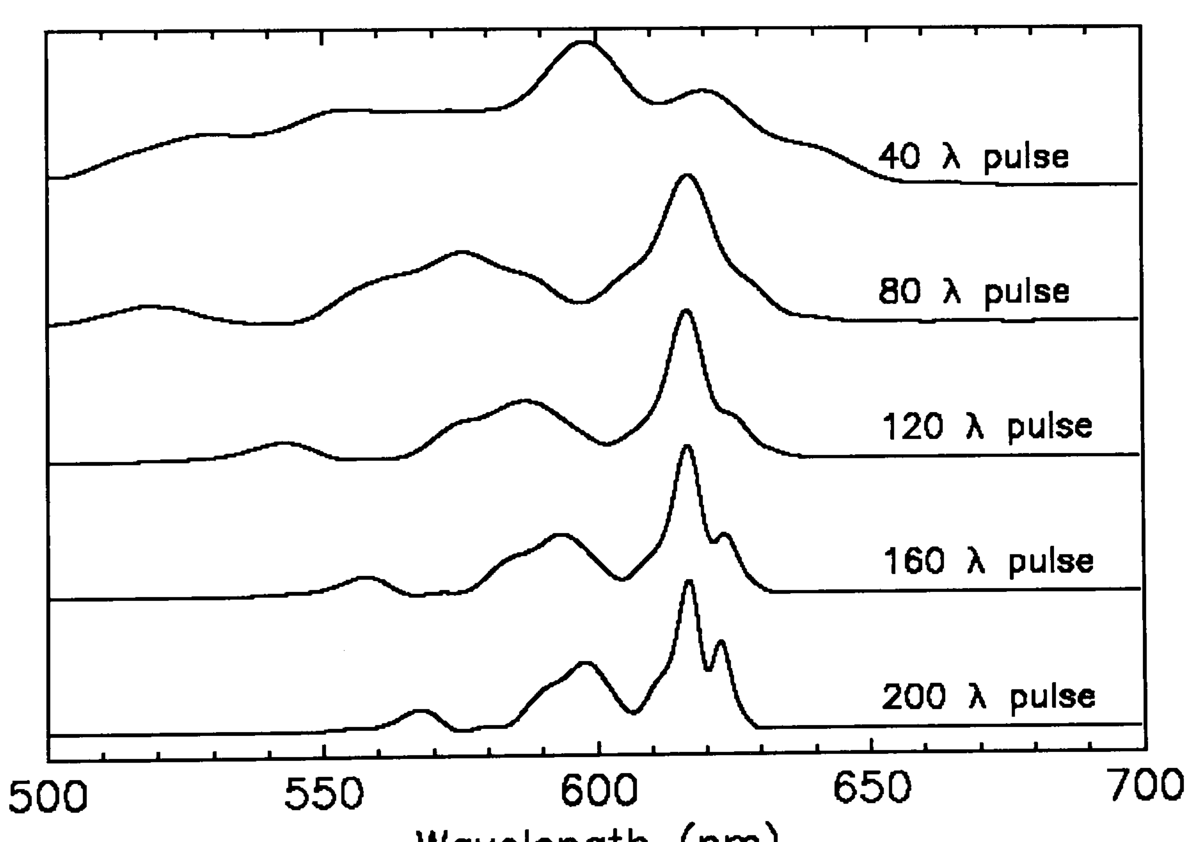

Figure 5.10: Effect of pulse duration on the transmitted spectrum, for a 620 nm, 10^{16} W/cm^2 laser pulse and 50 λ_0 of 5 atm argon.

shorter wavelengths, which becomes extreme for the shortest pulse duration shown.

5.4.4 Pump-Probe Spectra

It is possible to simulate a pump-probe experiment by modifying the propagation code to allow two pulses to simultaneously interact with the same length of plasma. In this case, one pulse (the pump) is of high intensity and causes ionization of the gas, and the second pulse (the probe) is of low intensity and merely serves to sample the time-dependent refractive index. This is analogous to the experimental situation of orthogonally-polarized pump and probe pulses [126].

Figure 5.11 shows the results of a pump-probe simulation, for a 620 nm, 100 cycle, 10^{16} W/cm^2 pump pulse and a weak probe pulse of the same wavelength and duration, propagating through a 50 λ_0 length of 5 atm argon gas. Spectra are shown for inter-pulse delays in the range –60 λ_0 to +30 λ_0, approximately –120 fs to +60 fs. A negative delay corresponds to the probe leading the pump, and a positive delay to the pump leading the probe.

It is apparent from the figure that the probe delay affects the amplitude of the various shifted spectral components but not the position. The maximum amount of blue-shifted structure occurs at a delay of –20 λ_0 (–40 fs), where the peak of the probe pulse corresponds approximately with the middle of the rising edge of the pump. If there were a simple correlation between the appearance of a particular ionization stage in the plasma and the creation of a spectrally-shifted peak, then it might be expected that the amplitudes of several shifted components would maximize at different times, as the probe moved across the leading edge of the pump. However, it appears that all the shifted components reach their maximum amplitude for approximately the same delay. This suggests that either all the ionization occurs within a narrow time window, which is unlikely, or several ionization stages contribute to the same shifted feature. Ideally, a set of pump-probe spectra would provide valuable information about the rates of ionization of different stages in the plasma. However, the amount of information which can be obtained is restricted once beam focusing is taken into account. It will be shown in a later section that the intensity variations across the beam and through the focus tend to blur much of the detail in the shifted spectrum.

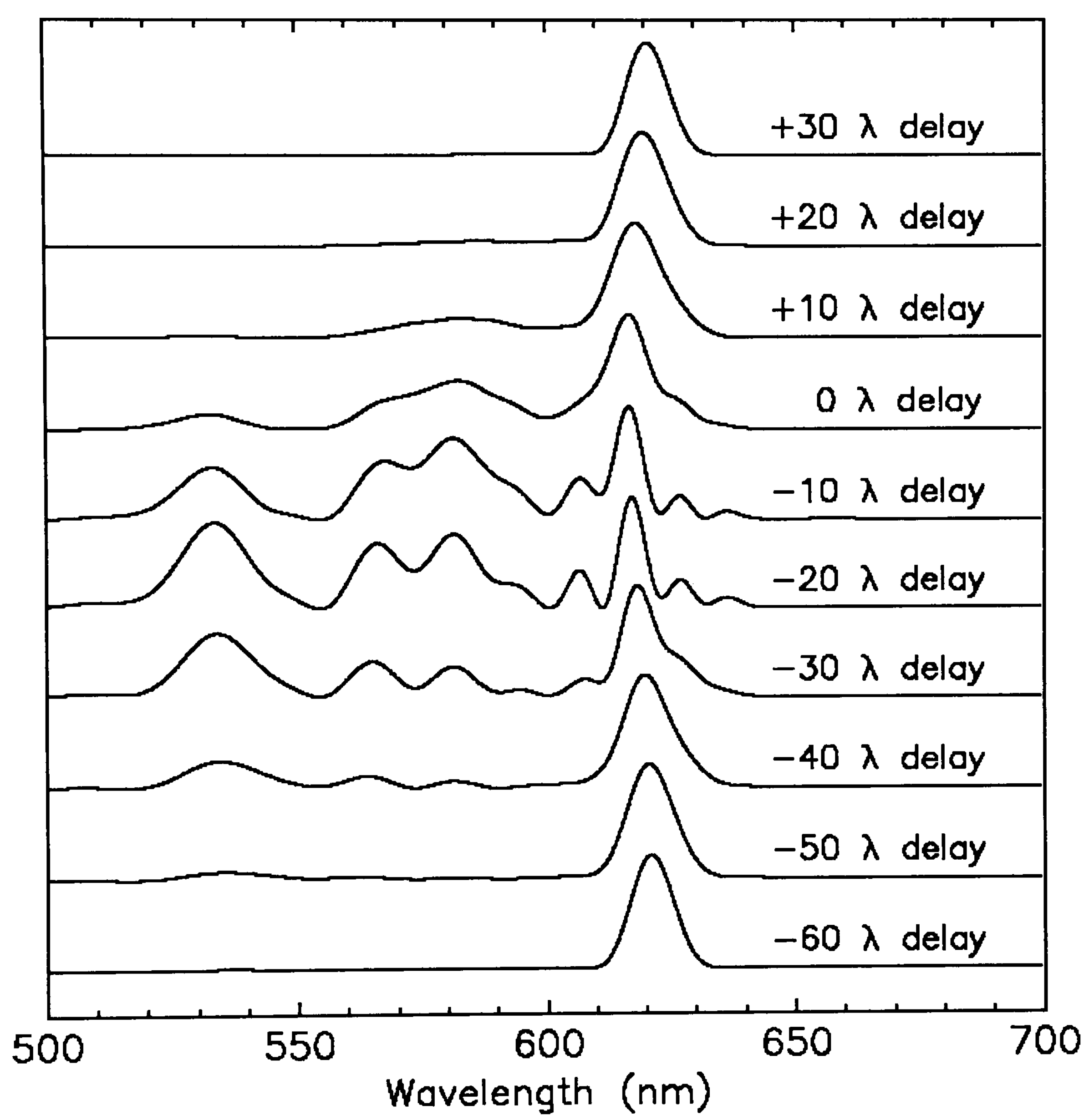

Figure 5.11: Transmitted spectra in pump-probe arrangement, for 620 nm, 100 cycle, 10^{16} W/cm^2 laser pulses and 50 λ_0 of 5 atm argon, with variable inter-pulse delay.

5.4.5 Collisional Ionization

Although the thermal energy of atmospheric-density field-ionized plasmas might be quite low, the electrons in the plasma can acquire a large coherent quiver energy, and in some cases this can lead to additional ionization through electron-ion collisions. The average quiver energy of a free electron is given by

$$\mathcal{E}_q = 2.3 \times 10^2 \left(\frac{I}{10^{16}\ \mathrm{W/cm^2}} \right) \left(\frac{\lambda_0}{500\ \mathrm{nm}} \right)^2 \ \mathrm{eV}\ . \tag{5.12}$$

Comparing this with typical ionization energies, such as those for argon and neon listed in Table 5.1, it is apparent that at high laser intensities the quiver energy can be sufficiently large to cause ionization even in highly-stripped species.

In general, the rate of collisional ionization can be written

$$\mathcal{R}_{coll} = n_e \int v\, f(v)\, \sigma(v)\, dv\ , \tag{5.13}$$

where $f(v)$ is the velocity distribution of the electrons, and $\sigma(v)$ is the velocity-dependent cross-section. The cross-section versus energy curves for all noble gas ions have a similar shape, and can be approximately fitted by a function of the form

$$\sigma(u) = A\, \frac{(u-1)^B}{u^C} \quad ; \quad u > 1\ , \tag{5.14}$$

where $u = \mathcal{E}/\mathcal{E}_i$ is the reduced energy. The constants A, B and C can be determined in each case by a least-squares fit of Eq. (5.14) to the actual cross-section curve. For the first eight ionization stages of argon, the calculated fitting constants are listed in Table 5.2, together with the peak cross-section and the energy at which this peak occurs. Data on the cross-sections have been taken from Ref. [131].

The propagation code has been further modified in order to investigate the effect of collisional ionization on the shifted pulse spectrum. Using the instantaneous quiver velocity (and assuming a stationary background of ions), the collisional ionization rate is determined at each time step from Eq. (5.13), and this is added to the tunnelling rate to find the total instantaneous ionization rate.

Figure 5.12 shows the difference between the degree of ionization in simulations

Table 5.2: Maximum cross-sections for the collisional ionization of the first eight ionization stages of argon, the energy at this peak value, and fitting constants for the cross-section curves.

ionization stage	cross-section peak (cm^2)	energy (eV)	fitting constants A (cm^2)	B	C
I	3.0×10^{-16}	70	1.7×10^{-15}	2.6	3.3
II	1.1×10^{-16}	95	4.8×10^{-16}	1.8	2.5
III	4.7×10^{-17}	120	1.9×10^{-16}	1.5	2.2
IV	2.0×10^{-17}	175	6.4×10^{-17}	1.1	1.8
V	1.0×10^{-17}	205	2.7×10^{-17}	1.0	1.5
VI	5.2×10^{-18}	300	1.8×10^{-17}	1.4	2.0
VII	2.7×10^{-18}	450	1.0×10^{-17}	1.6	2.2
VIII	1.5×10^{-18}	550	5.2×10^{-18}	1.6	2.2

with and without collisional ionization, for the case of a 620 nm, 100 cycle laser pulse propagating through a 50 λ_0 length of argon gas.

Collisions appear to raise the degree of ionization by an amount on the order of 0.1, although the increase becomes rapidly more significant for pressures $\gtrsim 5$ atm. For an intensity of 10^{16} W/cm^2 and a pressure of 5 atm, the degree of ionization is increased from 5.29 to 5.44, and this has a slight effect on the transmitted pulse spectrum, which can be seen in Fig. 5.13. The main peak has been further blue-shifted by $\sim$2 nm, and there is a small change in the other shifted features. Similar changes to the spectrum are seen for this pressure at different intensities. For pressures lower than 5 atm, almost no change to the spectrum is discernible, but for 10 atm the additional blue shift increases to $\sim$10 nm. If the same simulations were performed for neon, where the cross-sections are as much as a factor of 10 lower than for argon, collisional ionization would be expected to have little effect on the transmitted spectrum.

5.4.6 The Effect of Beam Focusing

The simulation results presented so far have been for a plane-wave pulse propagating through a fixed length of gas. This one-dimensional approximation, how-

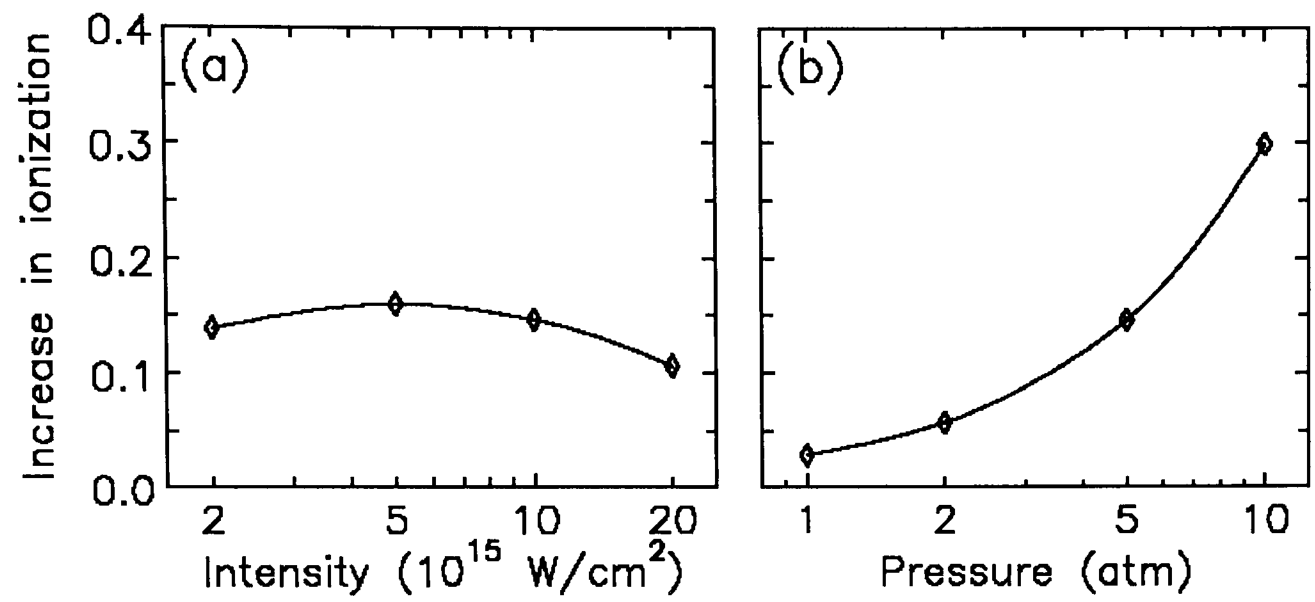

Figure 5.12: Additional ionization due to collisions for a 620 nm, 100 cycle laser pulse and 50 λ_0 of argon gas, (a) as a function of intensity for a pressure of 5 atm, and (b) as a function of pressure for an intensity of 10^{16} W/cm^2.

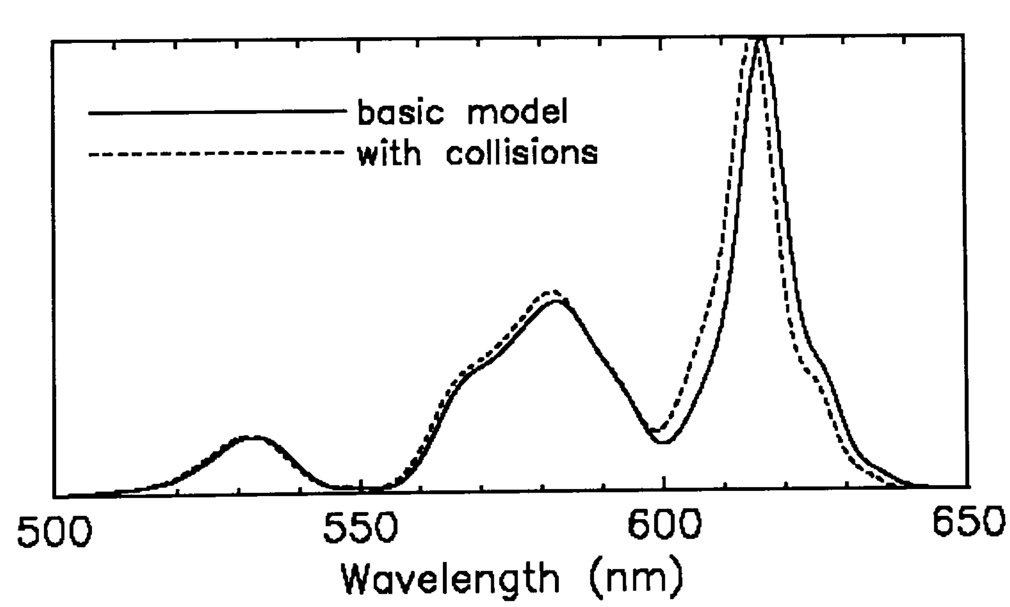

Figure 5.13: Comparison of transmitted spectra with and without collisional ionization, for a 620 nm, 100 cycle, 10^{16} W/cm^2 laser pulse and 50 λ_0 of 5 atm argon.

ever, does not closely match the real experimental conditions. In this section, the three-dimensional focusing geometry will be examined using the concept of Gaussian beams, and an attempt will be made to average a number of simulation results to obtain a more realistic spectrum.

A light beam propagating along an arbitrary axis can be approximately expanded into a sum of Hermite-Gaussian functions along that axis [132]. The lowest-order fundamental mode has a pure Gaussian distribution in both transverse directions and hence is radially symmetric. The intensity in such a Gaussian beam is given by

$$I = I_0 \, \frac{b_0^2}{b^2} \, \exp\left(\frac{-2r^2}{b^2}\right) , \tag{5.15}$$

where r is the radial coordinate and b is the beam radius, given by

$$b(z) = b_0 \left(1 + \frac{z^2 \lambda_0^2}{\pi^2 b_0^4}\right)^{1/2} . \tag{5.16}$$

Here z is the distance from the position of minimum beam radius (where the wavefront is a plane), λ_0 is the laser wavelength and b_0 is the minimum beam radius, also called the beam waist.

A Gaussian beam with diameter D and with a plane wavefront entering a thin convex lens of focal length f will be focused to a minimum radius of

$$b_0 = \frac{2\lambda_0 f}{\pi D} . \tag{5.17}$$

At the longitudinal position corresponding to the beam waist, the radial intensity distribution is given by

$$I = I_0 \, \exp\left(\frac{-2r^2}{b_0^2}\right) . \tag{5.18}$$

For a ray propagating along the axis, the longitudinal intensity variation is found from Eqs. (5.15) and (5.16) to have a Lorentzian form,

$$I = I_0 \left(1 + \frac{z^2 \lambda_0^2}{\pi^2 b_0^4}\right)^{-1} , \tag{5.19}$$

and the distance between the two points on the axis where the intensity is reduced to $I_0/2$, the confocal parameter, is given by

$$z_c = \frac{2\pi b_0^2}{\lambda_0} . \tag{5.20}$$

As the intensity of a Gaussian beam varies both radially and longitudinally, it is clear that attempting to apply a one-dimensional model to a three-dimensional situation is not a simple task. Averaging over the transverse intensity variation at the beam waist is not sufficient, because the beam radius varies as a function of distance along the axis. Also, and perhaps more seriously, a Gaussian beam analysis assumes that the light propagates through a homogeneous time-independent medium. In the case of an intense femtosecond pulse, ionization results in changes in the spatial properties of the beam, and the intensity distribution will not given correctly by Eq. (5.15) in any case. A higher-dimensional propagation code is really needed to address this problem, but including the complete ionization dynamics would be prohibitively expensive in terms of computer time.

In an attempt to at least approximate the effect of the beam focusing, the one-dimensional propagation model has been modified slightly to include a longitudinal intensity variation. The parts of the code relating to the pulse propagation remain unaltered, but the local intensity used in the ionization calculation is obtained from Eq. (5.19). The effective intensity for ionization is lowered at the edges of the plasma and peaks in the centre, thus imitating the effect of focusing in the longitudinal direction. The transverse intensity variation is included by averaging a number of spectra over a Gaussian radial distribution. If the intensity at the beam waist at a radial distance r_1 is I_1 and the intensity at r_2 is I_2, with $r_1 < r_2$, then from Eq. (5.18), the power passing through the annulus bounded by r_1 and r_2 is given by

$$P = \int_{r_1}^{r_2} I_0 \exp\left(\frac{-2r^2}{b_0^2}\right) 2\pi r \, dr = \frac{\pi b_0^2}{2} (I_1 - I_2) . \tag{5.21}$$

An averaged spectrum can be thus obtained from an equally-weighted sum,

$$f(\lambda) = \frac{1}{k} \sum_{i=1}^{k} f_i(\lambda) \ , \tag{5.22}$$

where the $f_i(\lambda)$ are calculated for peak intensities I_0/k, $2I_0/k$, $3I_0/k$, ... , I_0.

Longitudinally and transversely averaged spectra have been calculated assuming $f/4$ focusing of a Gaussian beam. The beam waist in this case is 1.58 μm and the confocal parameter is 25.2 μm. The transverse averaging across the beam profile is performed according to Eq. (5.22), with $k = 10$. Figure 5.14 shows the resultant spectra for a 620 nm, 130 cycle pulse (FWHM 100 fs) focused at $f/4$ in 5 atm argon and 5 atm neon. The results are plotted for three different peak intensities: 1.0, 2.0 and 4.0×10^{15} W/cm^2. For comparison, the experimental results of Downer *et al.* [125], obtained under the same focusing conditions with an estimated peak intensity of 10^{16} W/cm^2, are plotted on the same scales.

Overall, there is a poor fit of the simulation results to the experimental data. The simulated spectra show a large peak at or close to the fundamental wavelength, and a broadened shoulder which extends towards the blue. The experimental spectra, in contrast, show a significant blue shift of the main peak and roughly symmetrical broadening. The magnitude of the shift and the width of the broadened spectrum are considerably larger for argon than for neon.

In all of the simulated spectra in this chapter, a significant fraction of the pulse energy, in the trailing edge, is transmitted essentially unshifted in wavelength. This is a consequence of the field-induced ionization rates, which are extremely rapid above some critical appearance intensity. Ionization (and hence spectral shifts) can thus only occur during the leading edge of the pulse. Once the peak of the pulse has been reached, there is almost no additional ionization and no spectral shift. The reason why the experiment shows a large shift of the main peak, with very little energy remaining near the fundamental wavelength, is probably connected with spatial effects in the pulse propagation. Analogous to the spectral modifications caused by a time-dependent refractive index, spatial variation in the plasma will have a defocusing effect. Ionization in the leading edge of the pulse creates a lens-like structure, with a high electron density (refractive index $\eta < 1$) in the centre, and zero electron density ($\eta = 1$) at large radii. The trailing edge of the pulse will

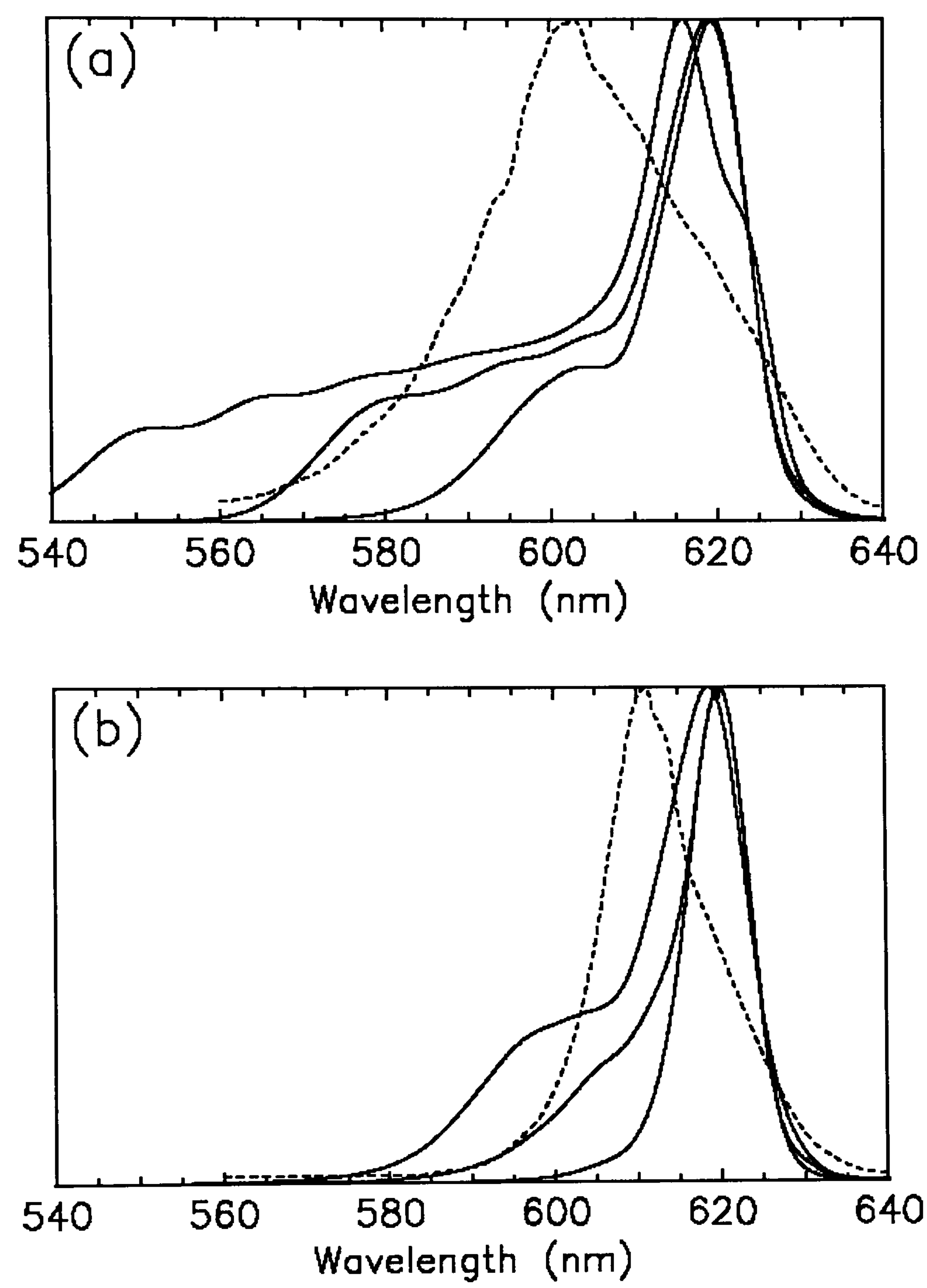

Figure 5.14: Transmitted pulse spectra averaged longitudinally and transversely, for $f/4$ focusing of a 620 nm, 100 fs laser pulse in (a) 5 atm argon and (b) 5 atm neon. Dotted lines represent the experimental data of Downer et al.; solid lines the simulation results, for intensities of 1.0, 2.0 and 4.0 $\times$ 10^{15} W/cm^2 (blue shift increases with intensity).

be refracted through this diverging plasma lens and, depending on the design of the experiment, may no longer fall within the acceptance angle of the collection optics.

This effect also partly explains another discrepancy between the theoretical and experimental spectra: the much lower peak intensity required in the model to match the maximum blue shift. The peak intensity in the experiment was estimated by measuring transmission through pinholes at low intensity, and by analysing the size of damage spots created on a solid target at high intensity. The creation of a plasma and the associated defocusing appears to decrease this peak intensity quite considerably. In addition, there is a degree of uncertainty in the absolute ionization rates calculated from the generalized tunnelling formula. Recent experiments by Augst *et al.* [102] have shown that the appearance intensities calculated from the tunnelling formula are always correct within a factor of two, but with a larger error for lower-Z elements.

There is agreement between the model and the experiment in at least one respect, and that is the significantly larger blue shift observed in the case of argon. In the model, this increased shift is due to the lower ionization potentials for argon compared to those for neon. Downer *et al.* have suggested that the increased blue shift is partly due to collisional ionization, but the simulated spectra in Sec. 5.4.5 showed only a small amount of additional broadening for a pressure of 5 atm.

Ultimately it is difficult to disentangle the various contributions, especially given the importance of spatial defocusing. A better theoretical fit would require a substantially more complicated model including a detailed knowledge of the experimental geometry.

5.5 Possible Applications

The spectral continuum produced by self-phase modulation at intensities below the threshold for plasma generation has already been used in time-resolved absorption spectroscopy, and future applications might include three-dimensional imaging and medical research [107]. The broadened spectrum produced by the formation of a plasma is one-sided and in general does not extend as far, but the fraction of the pulse energy which is shifted in wavelength can be very large. With an ultraviolet laser pulse (for example, KrF at 248 nm), the technique may prove to be a useful source of broadband VUV radiation.

One likely short-term application of plasma-induced spectral broadening is in the study of field-induced ionization rates. The spectrum of the transmitted pulse, especially in a pump-probe arrangement, is a sensitive indicator of the population dynamics in the plasma. The plasma conditions immediately after the laser pulse are also rather unusual, with a high degree of ionization but a relatively low average electron energy. Such a highly-ionized low-temperature gaseous plasma might potentially be used in a recombination x-ray laser. This topic will be investigated in the following chapter.

Chapter 6

Cold-Plasma Production by Field-Induced Ionization

Plasmas produced by optical field-induced ionization are fundamentally different from those in which the ionization is dominated by collisional processes. In particular, the average electron energy in a field-ionized plasma can be significantly lower than in a collisional plasma with the same degree of ionization. As a result, a field-ionized plasma should recombine rapidly following the laser pulse, and it has been suggested that this would make such a plasma ideal for implementing a recombination x-ray laser.

In this chapter, the plasma produced by an intense femtosecond laser pulse propagating through an atmospheric-density gas will be investigated, using the propagation-ionization model introduced previously. Initially, x-ray lasers will be briefly reviewed and the possible use of field-ionized plasmas in x-ray laser schemes will be discussed. An important parameter in determining the feasibility of these schemes is the final plasma temperature, and several mechanisms which can contribute to the temperature will be described. Simulation results for the plasma temperature under a range of conditions will be presented, and the relevance of these calculations to the proposed x-ray laser schemes will be discussed.

6.1 X-Ray Lasers

In recent years, laser-produced plasmas have been used as the gain medium for soft x-ray lasers operating in the wavelength range 4–30 nm [23]. Two distinct schemes have been developed, one based on collisional pumping and the other on recombination.

Collisionally-pumped x-ray lasers rely on selective excitation by electron-ion collisions during the incident laser pulse to generate a population inversion between excited states in highly-stripped medium-Z ions. Gain in a collisionally-pumped system was first observed on the 3p$\rightarrow$3s transition in Ne-like Se (Se^{24+}) at wavelengths of 20.63 and 20.96 nm by a group at the Lawrence Livermore National Laboratory in the United States [133], and the Ne-like scheme has subsequently been isoelectronically scaled as far as Mo^{32+} at 13.10 and 13.27 nm [134]. However, rapidly increasing pump energy requirements make further extrapolation of the Ne-like scheme difficult. A scheme with better potential for scaling to shorter wavelengths is the 4d$\rightarrow$4p transition in Ni-like ions. Gain in a Ni-like scheme was first observed in Eu^{35+} at a number of wavelengths as short as 6.58 nm [135], and this has been isoelectronically scaled to 4.48 nm in Ta^{45+} and 4.32 nm in W^{46+} [136]. In the collisionally-pumped x-ray laser experiments at Livermore, an exploding foil geometry is used, in which the target is irradiated from both sides with 500 ps, 532 nm laser pulses at a total intensity of $\sim 10^{14}$ W/cm^2 [137]. Slab or stripe targets, irradiated from one side only, have been successfully used by other groups [138, 139]. An efficiency of $\sim 10^{-6}$ has been measured in the Ne-like Se system at saturation, and double-pass operation using a multilayer dielectric mirror has also been demonstrated [25].

An alternative to collisional pumping is the recombination scheme, in which population inversion and gain is achieved during the recombination cascade which follows the end of the pump laser pulse. Amplification of spontaneous emission in a recombining plasma was first proposed by Gudzenko and Shelepin [140], and the theory has been subsequently developed by Peyraud and Peyraud [141], Jones and Ali [142], Green and Silfvast [143], Pert [144], Tallents [145] and Suckewer and Fishman [146]. A suitably high recombination rate can be achieved through the adiabatic expansion and cooling of a plasma formed from a fibre [26], foil [147] or slab target [148], or through the radiative cooling of a magnetically-confined plasma [149]. Gain occurs on the 3→2 transition in H-like ions, and the 5→3 and 4→3 transitions in Li-like ions. The population inversion is generated at the point in the cooling process where the collision limit is slightly above the upper lasing level. At this point, the upper level is still collisionally coupled to the levels above, but the lower state undergoes rapid radiative decay to the ground state. This is known as the regime of quasi-steady-state gain. It is also theoretically possible to achieve gain on ground-state transitions (2→1 in H-like ions, or 3→2 in Li-like ions) during the short time required for the radiative cascade to reach the lower levels of the ion, if the ground state is initially sufficiently depopulated. The duration of this transient gain is on the order of a radiative lifetime for the first excited state (~1 ps), much shorter than the duration of the quasi-steady-state gain, which is determined by the plasma expansion and cooling time (0.1–1 ns).

The most successful and versatile of the various geometries used in recombination x-ray laser experiments is the exploding fibre, which has been extensively investigated at the Rutherford Appleton Laboratory in the United Kingdom. Gain was first observed in H-like C (C^{5+}) at 18.2 nm, by irradiating a small-diameter (7 μm) fibre with 70 ps, 532 nm pulses at an intensity of $\sim 10^{12}$ W/cm^2 [150]. The H-like scheme has been isoelectronically scaled to F^{8+} at 8.1 nm [151], and, with a more powerful pump laser, to Na^{10+} at 5.42 nm and Mg^{11+} at 4.55 nm [152]. Gain has also been observed in Li-like Al (Al^{10+}) at 15.5 and 10.6 nm [153], and in Li-like Cl (Cl^{14+}) at 8.3 nm [154].

The recombination scheme has a number of advantages over collisional pumping: it is inherently more efficient (requires a lower electron temperature for a given x-ray laser wavelength); has slightly more favourable isoelectronic wavelength scaling ($\lambda \propto Z^{-2}$); and, being hydrogenic, should be easier to model theoretically. However, it also suffers from a number of problems. In order to achieve rapid cooling, the fibre diameter has to be smaller than most modern high-power laser systems can focus, and this leads to a poor energy-coupling efficiency. The gain region is a hollow pipe (~100 μm radius × 10–20 μm wall thickness) which is difficult to scale up in volume, and this reduces the likelihood of successful multipass operation. The Z-dependence of the initial plasma density ($n_e \propto Z^7$ for maximum gain) is a problem for isoelectronic scaling to shorter wavelengths [155]. It has yet to be demonstrated that refraction problems can be reduced to the point where the laser can be run in the saturated regime, and there is also a serious question concerning the treatment of radiation trapping in the theoretical modelling [156]. Overall, the potential benefits of the recombination scheme are still some way from being fully realised.

Plasmas produced by field-induced ionization have certain desirable properties for recombination x-ray laser schemes. The pulse duration produced by the latest generation of intense lasers is sufficiently short ($\lesssim$ 1 ps) to allow the possibility of transient gain on ground-state transitions and, more importantly, the average electron energy after the pump pulse can be low enough to allow rapid recombination to commence without the need for additional cooling. Together, these two characteristics may allow high gain to be achieved on shorter wavelength transitions than those currently accessible [29, 157, 158].

In a field-ionized plasma, the initial recombination rate is strongly dependent on the residual temperature, and this parameter is obviously of primary importance in assessing the feasibility of any new lasing scheme. Recent studies by Burnett and Enright [158] and Amendt *et al.* [159] have proposed recombination x-ray laser schemes in the transient gain regime which require a residual plasma temperature of less than about 50 eV. However, there is a relative lack of quantitative data concerning how such a plasma might be produced. In the remainder of this chapter an attempt is made to give a quantitative estimate of the final temperature for the case of an atmospheric-density highly-ionized neon plasma. This is directly relevant to the proposal by Amendt *et al.* for an x-ray laser in Li-like Ne at 9.8 nm.

6.2 Plasma Heating Mechanisms

In a collision-dominated laser-produced plasma, ionization occurs as a result of collisions between electron and ions. To produce a rapid ionization rate, the average electron energy must be significantly greater than the ionization potential for the atom or ion concerned. Thus (referring to Table 5.1, for example), the electron temperature needs to be on the order of several hundred electron-volts to produce highly-stripped ions. In field-induced ionization, by contrast, the strength of the optical field alone determines the ionization rate, and the average energy of the ionized electrons can be considerably less than the ionization potential. There are a number of separate mechanisms which are important in determining the electron energy in a field-ionized plasma, including above-threshold-ionization energy, collisional heating, space-charge effects and parametric instabilities. These will each be discussed below.

6.2.1 Above-Threshold-Ionization Energy

Electrons produced in the field-induced ionization process are emitted with excess kinetic energy which has come to be known as above-threshold-ionization (ATI) energy. The form of the ATI energy spectrum depends on the laser intensity, a convenient measure of which is the tunnelling parameter, γ, defined by

$$\gamma = (\mathcal{E}_i/2\mathcal{E}_q)^{1/2} \ . \tag{6.1}$$

Here $\mathcal{E}_i$ is the ionization potential and $\mathcal{E}_q$ is the quiver energy, given by

$$\mathcal{E}_q = \frac{e^2 E_0^2}{4 m_e \omega_0^2} \ . \tag{6.2}$$

At low laser intensities, for which $\gamma \gg 1$, the energy spectrum takes the form of a series of distinct peaks separated by the photon energy [160]. At higher laser intensities, in the tunnelling regime where $\gamma \ll 1$, these peaks disappear and are replaced by a relatively smooth distribution. Analytical calculations by Delone and Krainov [100] for linearly-polarized light predict an electron energy distribution of the form

$$f(\mathcal{E}) = f(0) \exp\left(-\frac{2\gamma^3 \mathcal{E}}{3\hbar\omega_0}\right) \ . \tag{6.3}$$

For typical values of γ, the average ATI energy is a small fraction of the quiver energy.

In the high-intensity limit, ATI energy has a simple classical explanation [29]. As already mentioned in the previous chapter, electrons which are ionized at a point in the laser cycle displaced from the peak acquire a dephasing energy, which appears as residual kinetic energy once the pulse has passed. This energy can be estimated on the basis of an elementary model. Assuming that the field is sinusoidal in time, $E = E_0 \sin \omega_0 t$, an electron ionized at time t_0 will have a velocity given by

$$v = \frac{eE_0}{m_e \omega_0} \left(\cos \omega_0 t - \cos \omega_0 t_0 \right) . \tag{6.4}$$

The average kinetic energy is then

$$\frac{1}{2} m_e \langle v^2 \rangle = \frac{e^2 E_0^2}{4 m_e \omega_0^2} \left(1 + 2 \cos^2 \omega_0 t_0 \right) . \tag{6.5}$$

The first term in this expression is the coherent quiver energy, $\mathcal{E}_q$, and the second term is the dephasing or ATI energy. Integrating over a laser cycle, the average ATI energy can be written

$$\langle \mathcal{E}_{ATI} \rangle = \frac{2\, \mathcal{E}_q \int \mathcal{R}(\phi) \cos^2 \phi \, d\phi}{\int \mathcal{R}(\phi) \, d\phi} , \tag{6.6}$$

where $\mathcal{R}(\phi)$ is the ionization rate, and ϕ is the phase of the field. For a high-intensity laser pulse, the ionization rate can be calculated using the generalized tunnelling formula discussed in Chapter 4,

$$\begin{aligned} \mathcal{R}_{st} = {} & \frac{\omega_{at}}{2} C_{n^*}^2 \frac{\mathcal{E}_i}{\mathcal{E}_h} \frac{(2l+1)(l+|m|)!}{2^{|m|}(|m|)!(l-|m|)!} \\ & \times \left[2 \left(\frac{\mathcal{E}_i}{\mathcal{E}_h} \right)^{3/2} \frac{E_{at}}{E} \right]^{2n^* - |m| - 1} \exp \left[-\frac{2}{3} \left(\frac{\mathcal{E}_i}{\mathcal{E}_h} \right)^{3/2} \frac{E_{at}}{E} \right] . \end{aligned} \tag{6.7}$$

Here $\mathcal{E}_i$ is the ionization potential for the atom or ion concerned, $\mathcal{E}_h$ is the ionization potential for hydrogen, ω_{at} and E_{at} are the atomic units for frequency and electric field, respectively, l and m are quantum numbers for the initial state, n^* is the effective principle quantum number and C_{n^*} is a constant of order unity [99].

To estimate the ATI energy in a realistic situation, the intensity at which a particular ionization stage is produced must be known. Figure 6.1(a) shows the

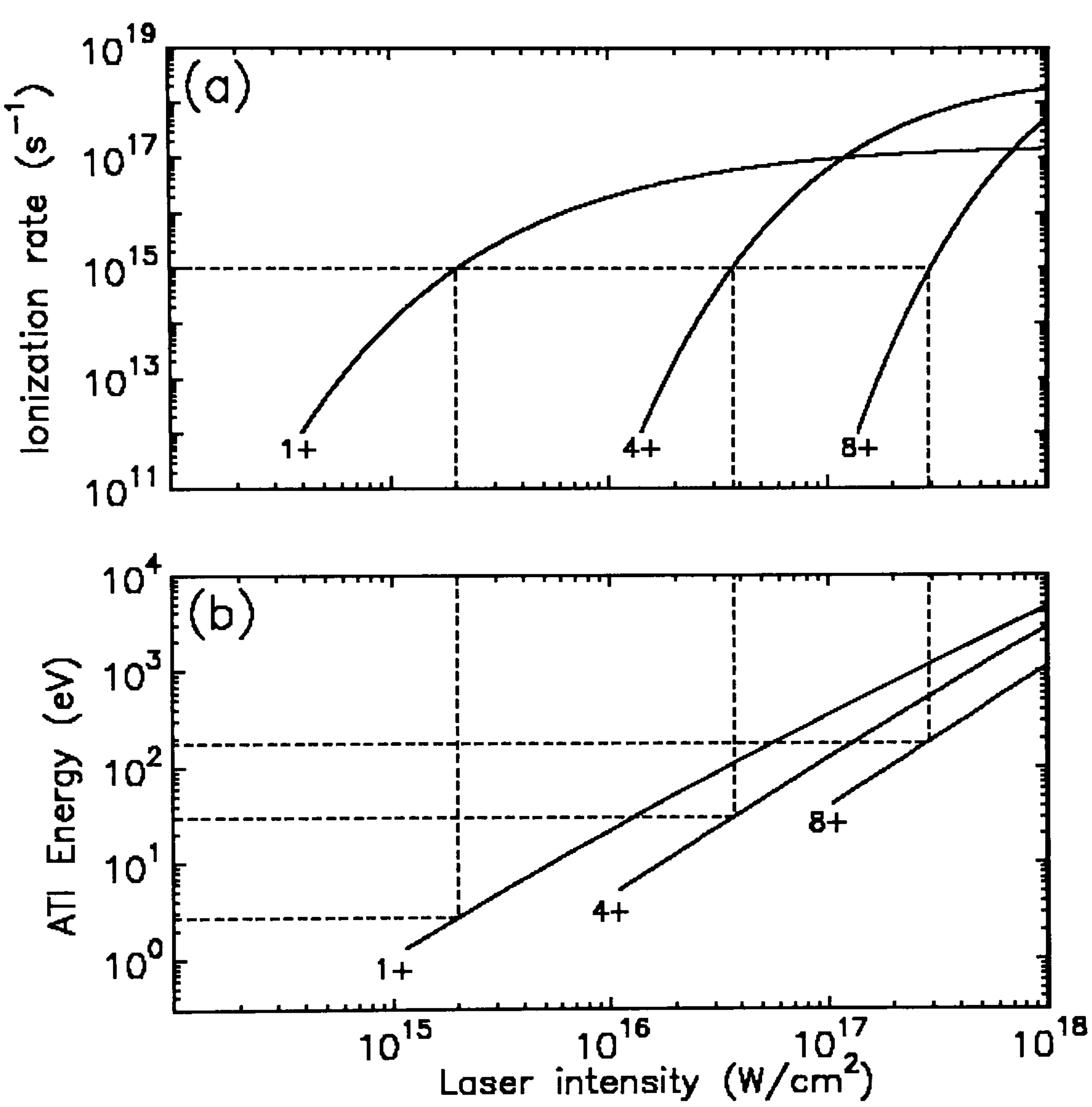

Figure 6.1: (a) Cycle-averaged tunnelling ionization rates for several ionization stages of neon; (b) ATI energy as a function of laser intensity.

Table 6.1: ATI energy of electrons from several ionization stages of neon, as a proportion of the ionization potential and as a proportion of the quiver energy at the appearance intensity, calculated for 248 *nm light.*

ionization stage	ionization potential (eV)	appearance intensity (W/cm^2)	quiver energy (eV)	ATI energy (eV)	prop. of quiver energy	prop. of ionization potential
Ne^{+}	21.6	2.0×10^{15}	11.6	2.7	0.23	0.13
Ne^{4+}	97.1	3.7×10^{16}	214	30	0.14	0.31
Ne^{8+}	239.1	2.9×10^{17}	1680	180	0.11	0.75

cycle-averaged tunnelling ionization rates for several ionization stages of neon, and marks the intensity where each rate reaches 10^{15} s^{-1}. This can be used as an approximate appearance intensity. In Fig. 6.1(b) the residual ATI energy from Eq. (6.6) is shown as a function of laser intensity. If the ATI energy depended only on the quiver energy, there would be a linear dependence on laser intensity. In fact, the slope of the curves is greater than linear, which means that at high intensities the average dephasing, $\langle \cos^2 \omega_0 t_0 \rangle$, also increases. Using both graphs, the ATI energy at the appearance intensity can be determined, and the results for the three ionization stages are summarized in Table 6.1. The ATI energy increases from 2.7 eV for Ne^{+} to 180 eV for Ne^{8+}, although the ratio of the ATI energy to the quiver energy decreases from 0.23 to 0.11. The ratio of the ATI energy to the ionization potential increases with the ionization stage, but always remains less than unity. The field-ionized plasma is thus always cooler than an equivalent collision-dominated plasma, but the difference becomes smaller as the degree of ionization increases. For a potential recombination x-ray laser scheme, it is obviously the electrons from the highest ionization stages which contribute most to the final plasma temperature.

All of the discussion in this section has concerned field-induced ionization for linearly-polarized light. If circularly-polarized light is used instead, then there is no point in the laser cycle where the electric field crosses through zero, and the average ATI energy increases to approximately twice the quiver energy [161].

6.2.2 Collisional Heating

In a sufficiently dilute plasma, the ATI energy would be the only contribution to the final temperature, but at atmospheric densities collisions play an important role. The effect of electron-ion collisions is to perturb the coherent oscillatory motion of the electrons in the laser field and convert a fraction of the quiver energy into random thermal motion.

Collisional absorption has already been discussed in Chapter 2. For a velocity-independent electron-ion collision frequency, ν_{ei}, the cycle-averaged power dissipation per electron is given by

$$P/n_e = 2\,\mathcal{E}_q\,\nu_{ei}\ , \tag{6.8}$$

where $\mathcal{E}_q = e^2E_0^2/4m_e\omega_0^2$ is the quiver energy.

For gaseous plasmas at a temperature of greater than a few eV (in the classical weakly-coupled regime), the Spitzer expression for the effective collision frequency is valid [33, 34]. Assuming a Maxwellian velocity distribution, this is given by

$$\nu_{ei} = \frac{4\sqrt{2\pi}}{3}\frac{Zn_e e^4\ln\Lambda}{(4\pi\epsilon_0)^2\,m_e^{1/2}(k_BT_e)^{3/2}}\ , \tag{6.9}$$

where Z is the degree of ionization, T_e is the electron temperature, and $\ln\Lambda$ is the Coulomb logarithm, defined in the usual way. At high laser intensities, a correction for the electron quiver motion needs to be included. A correction discussed by Schlessinger and Wright [40] involves multiplying Eq. (6.9) by the factor

$$F = \left(1 + v_q^2/3v_{th}^2\right)^{-3/2}\ , \tag{6.10}$$

where $v_{th} = (k_BT_e/m_e)^{1/2}$ is the characteristic thermal velocity and $v_q = eE_0/m_e\omega_0$ is the quiver velocity.

Using Eqs. (6.8), (6.9) and (6.10), the collisional heating rate under a given set of plasma conditions can be calculated. The heating rate is plotted in Fig. 6.2 as a function of laser intensity, for $n_e = 10^{20}$ cm^{-3}, $Z = 8$ and $\lambda_0 = 248$ nm. Curves are shown for three different electron temperatures: $k_BT_e = 10$, 30 and 100 eV. At low intensities the heating rate is linear in the laser intensity, and is a sensitive function of the plasma temperature. Above about 10^{16} W/cm^2 the heating rate begins to decrease, and in this region, where the quiver energy is large compared with the thermal energy, the heating rate is roughly independent of the plasma temperature. At a laser intensity of 10^{17} W/cm^2 the heating rate is ~800 eV/ps.

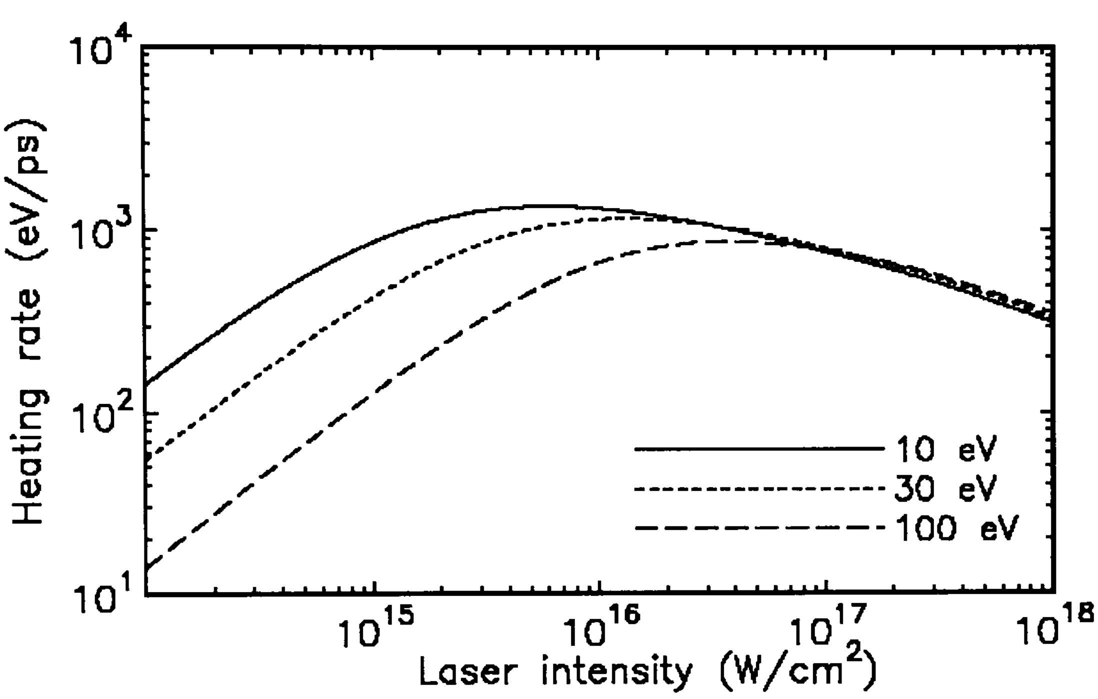

Figure 6.2: Collisional heating rate as a function of laser intensity, for $n_e = 10^{20}$ cm^{-3}, $Z = 8$ and $\lambda_0 = 248$ nm.

6.2.3 Stimulated Raman Scattering

An intense light wave propagating through a plasma can, under certain conditions, excite parametric instabilities in which the incident light wave is coupled to plasma oscillations [30]. The most important of these instabilities for the present case is stimulated Raman scattering, in which the incident light wave decays into a scattered light wave plus an electron plasma wave. The plasma wave is damped by collisions, which can lead to considerable additional heating of the electrons. The maximum growth rate of the Raman instability is approximately given by [159]

$$\Gamma \simeq \frac{v_q}{2c}(\omega_p \omega_0)^{1/2} , \tag{6.11}$$

where v_q is the quiver velocity and ω_p is the plasma frequency. For a typical set of parameters ($n_e = 10^{20}$ cm^{-3}, $\lambda_0 = 248$ nm and $I = 10^{17}$ W/cm^2), the growth time is around 10 fs.

Particle-in-cell computer simulations performed by Amendt *et al.* [159] have shown that the Raman instability produces a two-temperature electron energy distribution, with a fraction of the population in a high-temperature tail (~1–10 keV) and the remainder in a low-temperature background (~10–100 eV). The background temperature increases rapidly with both electron density and laser pulse duration.

6.2.4 Ponderomotive and Space-Charge Forces

A gradient in light intensity gives rise to a so-called ponderomotive force,

$$\mathbf{F} = -\frac{e^2}{4m_e\omega_0^2}\,\nabla E^2 \,, \tag{6.12}$$

which acts to push electrons away from regions of high intensity [30]. The ponderomotive force is opposed by a space-charge force, which resists the separation of the electron and ion populations. In a dilute plasma, where the space-charge forces are reduced, and for an intense, tight laser focus, the ponderomotive force is sufficient to almost completely expel the electrons from the central focal region. Particle-in-cell simulations performed by Penetrante and Bardsley [162] under these conditions have clearly shown the formation of such a structure. Following the laser pulse, electrons are drawn back into the central void by the space-charge force, resulting in intense plasma oscillations. The energy in these oscillations is dissipated in collisions, leading to additional electron heating. The plasma oscillations are resonantly enhanced when the laser pulse duration is equal to half the plasma oscillation period.

The particle-in-cell simulations have shown that in order for the ponderomotive force to dominate over space-charge forces, the focal spot size must be on the order of 1 μm, and the laser intensity (in W/cm^2) must be approximately one order of magnitude larger than the ion density (in cm^{-3}). For a laser intensity of 10^{18} W/cm^2, this requires the ion density to be less than 10^{17} cm^{-3}. At atmospheric density (2.5×10^{19} cm^{-3}), and with a more typical focal spot size (5–10 μm), this particular heating mechanism can be neglected.

In addition, there is some evidence from the particle-in-cell simulations that under certain circumstances the presence of space-charge forces can decrease the ATI energy of the electrons, presumably by modifying the quiver motion. This effect was noted over a range of ion densities from 10^{18}–10^{20} cm^{-3}, but the details of the focusing geometry were not specified.

6.3 Simulation Results

The propagation-ionization model, introduced in Chapter 5 to explain the spectral shifting and broadening of intense femtosecond laser pulses in gases, can also be used to estimate the final temperature of the plasma which is produced. The contributions arising from ATI and collisional heating can be calculated separately, but it is not possible to include space-charge and plasma instability effects. In this section, results are presented for the temperature of a neon plasma over a wide range of conditions relevant to the proposed x-ray laser scheme in Li-like Ne.

The model has already been discussed in some detail, and here only the modifications required to accurately predict the plasma temperature will be described. It should be noted that the model is non-relativistic in its treatment of electron motion, and the condition that the quiver velocity be much less than the speed of light sets an upper limit on the laser intensity,

$$I \ll 2.2 \times 10^{19} \left(\frac{248 \text{ nm}}{\lambda_0}\right)^2 \text{ W/cm}^2 . \tag{6.13}$$

The average ATI energy as a function of distance, $\mathcal{E}_{ATI}(x)$, is calculated directly from the electron distribution function,

$$\mathcal{E}_{ATI}(x) = \frac{\int \frac{1}{2} m_e v^2 f(x,v)\, dv}{\int f(x,v)\, dv} . \tag{6.14}$$

A fine velocity mesh is required to obtain sufficient accuracy, typically $\Delta v = v_q/100$, where v_q is the quiver velocity at the peak of the laser pulse. The electron energy distribution is not initially Maxwellian, and although electron-electron collisions would eventually thermalize the population, the equilibration rate, $1/\tau_{ee}$, is not necessarily rapid compared with the duration of the pulse [48]. For $n_e = 10^{20}$ cm^{-3} and $k_BT_e = 20$ eV, the equilibration time $\tau_{ee} \simeq 40$ fs, and this characteristic time scales as $\tau_{ee} \propto (k_BT_e)^{3/2}n_e^{-1}$. However, even if the distribution is not Maxwellian, an effective ATI temperature can be defined by $k_BT_{ATI} = \frac{2}{3}\langle\mathcal{E}_{ATI}\rangle$.

Collisional heating is incorporated into the code by modifying the equation of motion for the electron distribution function to include a friction term. Thus, the average velocity, $\bar{v}$, evolves according to

$$\frac{d\bar{v}}{dt} + \nu_{ei}\bar{v} = -\frac{eE}{m_e} \,, \tag{6.15}$$

where ν_{ei} is the electron-ion collision frequency. The effective friction force due to collisions is given by $m_e\nu_{ei}v$, and the rate of energy absorption per electron as a function of distance is

$$P(x) = \frac{\displaystyle\int m_e\nu_{ei}v^2 f(x,v)\,dv}{\displaystyle\int f(x,v)\,dv} \,. \tag{6.16}$$

Integrating $P(x)$ with respect to time throughout the pulse gives the total energy absorption due to collisional heating.

Determining the collision frequency is complicated because the propagation-ionization model calculates the instantaneous electron motion in the laser field, and there is no clearly-defined cycle-averaged quiver velocity. In the part of the laser cycle where the instantaneous velocity is much less than the thermal velocity, the uncorrected Spitzer expression, Eq. (6.9), can be used. At the opposite extreme, where the instantaneous velocity is much greater than the thermal velocity, the Spitzer expression for a straight-line velocity [33, 34],

$$\nu_{ei} = \frac{8\pi Z n_e e^4 \ln\Lambda}{(4\pi\epsilon_0)^2 m_e^2 v^3} \,, \tag{6.17}$$

should be used instead. Over the complete laser cycle, an expression is required which interpolates between these two limiting forms. This can be obtained from Eq. (6.17), using an effective velocity,

$$v_{eff} = \left(v^2 + \kappa v_{th}^2\right)^{1/2} \ , \tag{6.18}$$

where v is the instantaneous quiver velocity and $v_{th} = (k_B T_e/m_e)^{1/2}$ is the thermal velocity. Choosing $\kappa = (9\pi^2/4)^{1/6}$ makes this expression correct in both limits, $v \ll v_{th}$ and $v \gg v_{th}$, and provides an interpolated value in the region between. A minimum temperature must be assumed for the Spitzer expression to be valid, and this is typically taken as 5 eV. As long as the final temperature is significantly greater than the imposed minimum, the actual choice is not critical.

For the results in the following sections, the laser pulse is only propagated through a short length of gas ($20\,\lambda_0 \simeq 5$ μm for 248 nm light). Over such a short distance, the plasma properties are almost constant, and the temperatures are plotted simply as averages across the plasma. Pulse durations are given as FWHM for a sine-squared field envelope. A typical simulation run for a 100 fs, 248 nm laser pulse required approximately 50 minutes of CPU time on a Convex C220 vector processor.

6.3.1 Dependence on Laser Intensity

Figure 6.3 shows the plasma temperature and final degree of ionization as functions of laser intensity, for a 100 fs, 248 nm laser pulse and a neon atom density of 2.5×10^{18} atoms/cm^3. The critical intensity required for the production of a Ne^{8+} plasma is $\sim 2.5 \times 10^{17}$ W/cm^2, and further calculations, not shown here, have confirmed that this intensity is independent of the plasma density. At intensities below critical, the dependence of the ATI and collisional temperatures on intensity is difficult to analyse, as there is the added complication of a varying degree of ionization, but above this point the behaviour is somewhat easier to interpret.

The ATI temperature increases slowly, approximately as $I^{0.1}$, above the critical intensity. If ionization of a particular stage always occurred at some fixed appearance intensity, then the ATI temperature would be independent of the peak pulse intensity, and the fact that it has a small positive slope indicates that this is not quite the case. In a femtosecond laser pulse, the intensity rise-time is comparable with the ionization rates, and increasing the peak intensity means that each of the

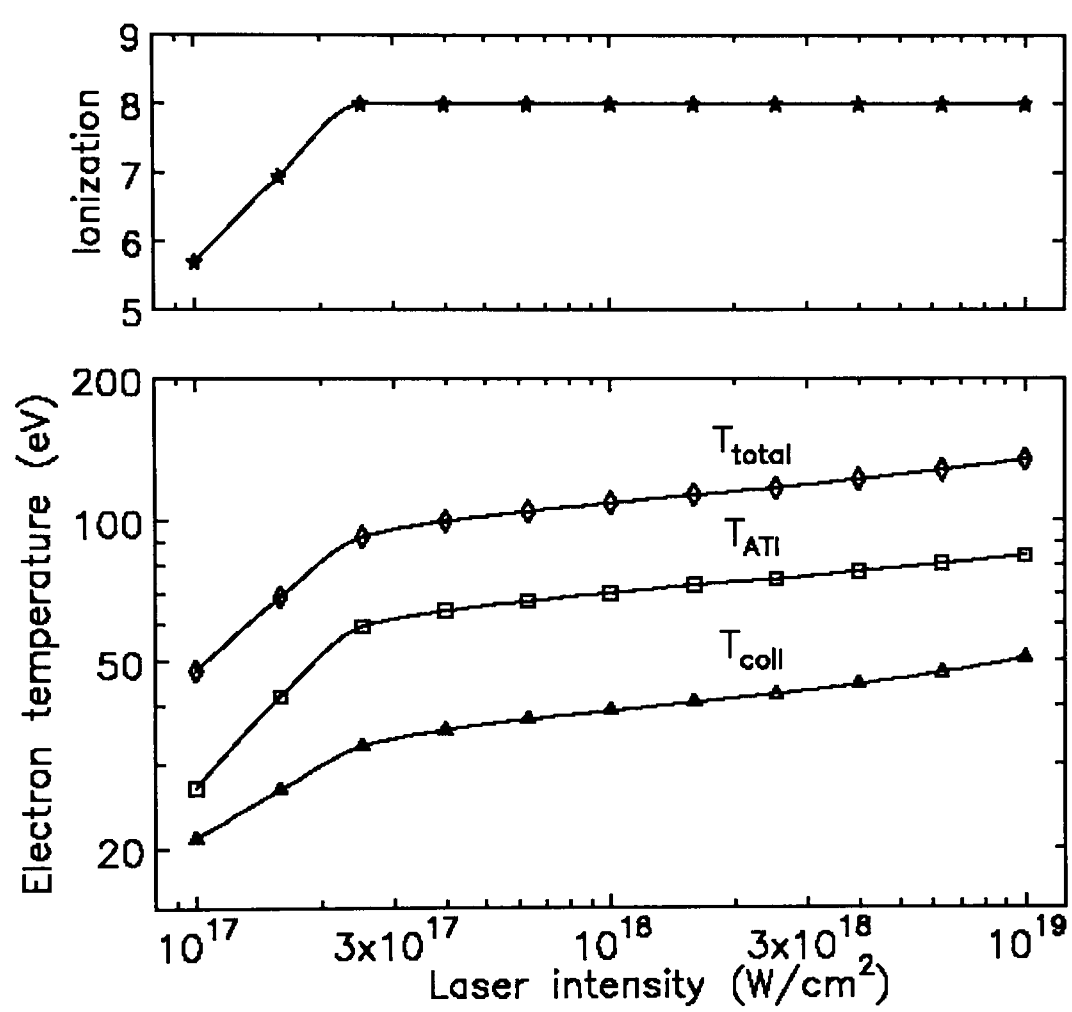

Figure 6.3: Plasma temperature and final degree of ionization as functions of laser intensity, for a 100 *fs,* 248 *nm laser pulse and a Ne atom density of* 2.5×10^{18} cm^{-3}.

ionization stages survives to a slightly higher intermediate intensity. This increases the quiver energy and hence raises the ATI temperature. As the quiver energy is much larger than the thermal energy, the electron-ion collision frequency would be expected to decrease as $I^{-3/2}$, and the collisional heating rate should then decrease as $I^{-1/2}$. In fact, over the intensity range shown here, the collisional temperature has a small positive slope. This is probably because at higher intensities the electron density rises to its maximum value earlier in the pulse, which increases the total collisional heating and more than compensates for the decrease in the collision frequency.

6.3.2 Dependence on Plasma Density

At 2.5×10^{17} W/cm^2, the minimum intensity required for the production of a Ne^{8+} plasma, Fig. 6.4 shows the variation in plasma temperature with density, for a 100 fs, 248 nm laser pulse.

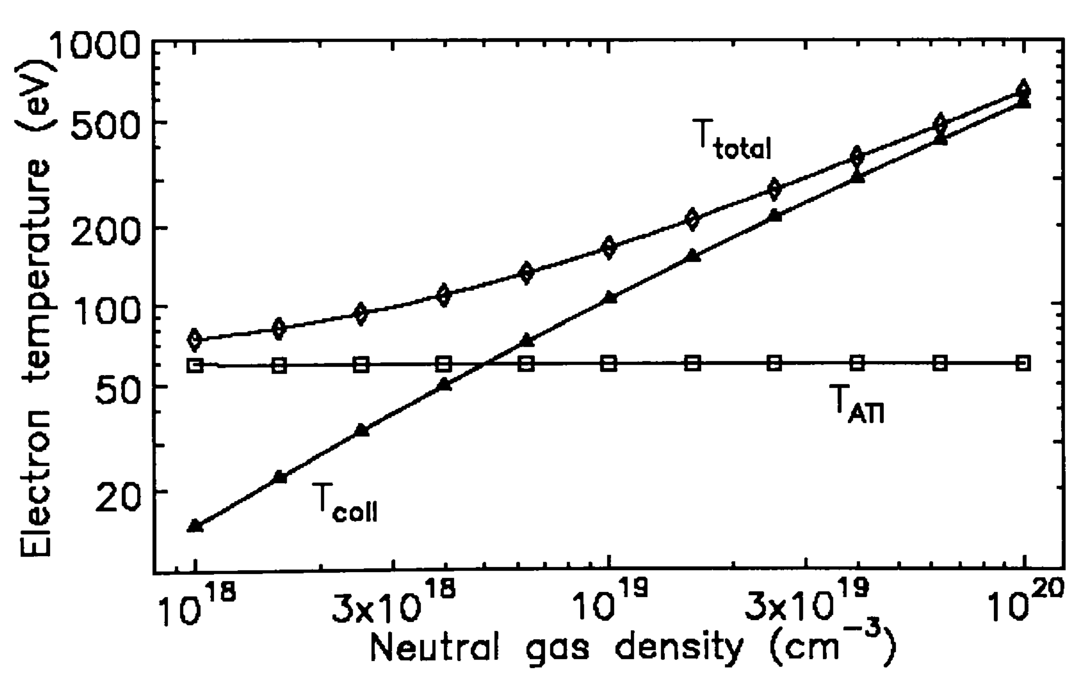

Figure 6.4: Plasma temperature as a function of density, for a 100 fs, 248 nm, 2.5×10^{17} W/cm^2 laser pulse.

The ATI temperature, as expected, is independent of the plasma density. The collisional temperature increases approximately linearly with density, in accordance with the density dependence of the collision frequency. There is a slight deviation below an exact linear dependence at high densities, which is probably due to rapid heating early in the pulse. It was seen earlier that for intensities $\lesssim 10^{16}$ W/cm^2 the collisional absorption rate is a sensitive function of the plasma temperature.

6.3.3 Dependence on Laser Pulse Duration

For a 248 nm laser pulse at an intensity of 2.5×10^{17} W/cm^2 and a neon atom density of 2.5×10^{18} cm^{-3}, Fig. 6.5 shows the dependence of the plasma temperature on the pulse duration.

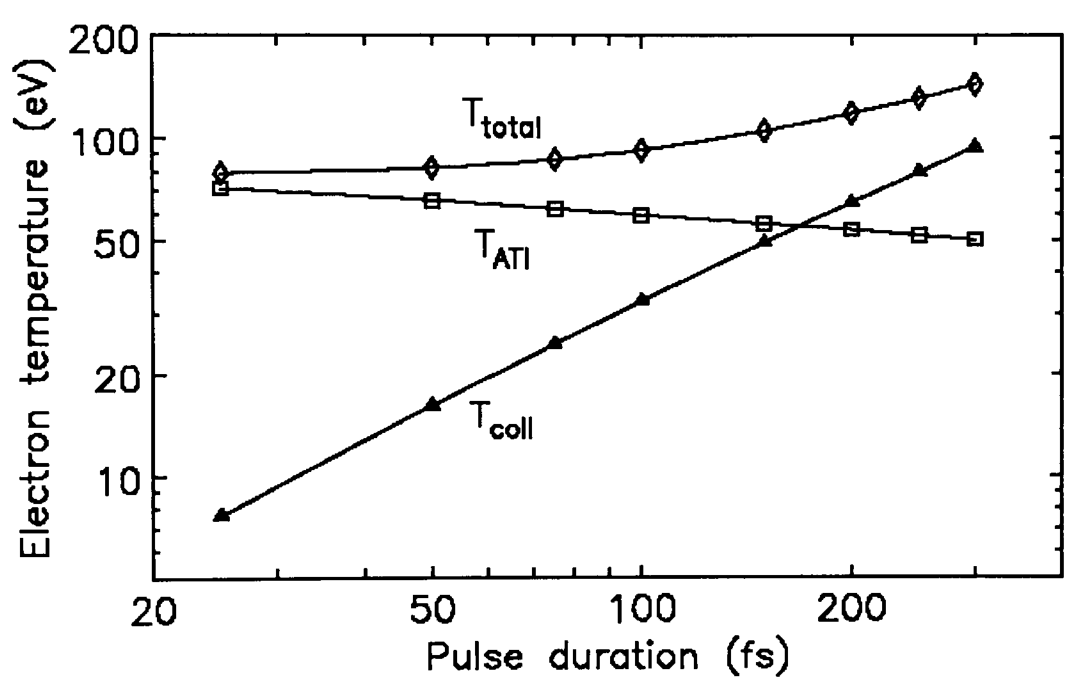

Figure 6.5: Plasma temperature as a function of laser pulse duration, for a 248 nm, 2.5×10^{17} W/cm^2 laser pulse and a Ne atom density of 2.5×10^{18} cm^{-3}.

The ATI temperature is determined by the intensity at which the various intermediate stages are ionized. If the field-induced ionization rates were infinitely fast above some threshold intensity, then complete ionization of a particular stage would always occur at a fixed appearance intensity, and the ATI temperature would be independent of the pulse duration. This would apply in the long-pulse limit, $\tau \gg 100$ fs. However, in the present case, especially for $\tau < 100$ fs, the ionization rates cannot be considered to be infinitely fast. The populations of the various ionization stages do not have sufficient time to come to equilibrium, and as the pulse becomes shorter, intermediate ionization stages survive to higher intensities. The ATI temperature thus increases slightly as the pulse duration is reduced. For the shortest pulses, the final stage is not even completely ionized. The collisional temperature increases almost exactly linearly with increasing pulse duration, and as the total plasma temperature is dominated by the collisional component, shorter pulses reduce the total temperature.

6.3.4 Dependence on Laser Wavelength

The plasma temperature as a function of laser wavelength is shown in Fig. 6.6, for a 100 fs laser pulse at an intensity of 2.5×10^{17} W/cm^2 and a neon atom density of 2.5×10^{18} cm^{-3}.

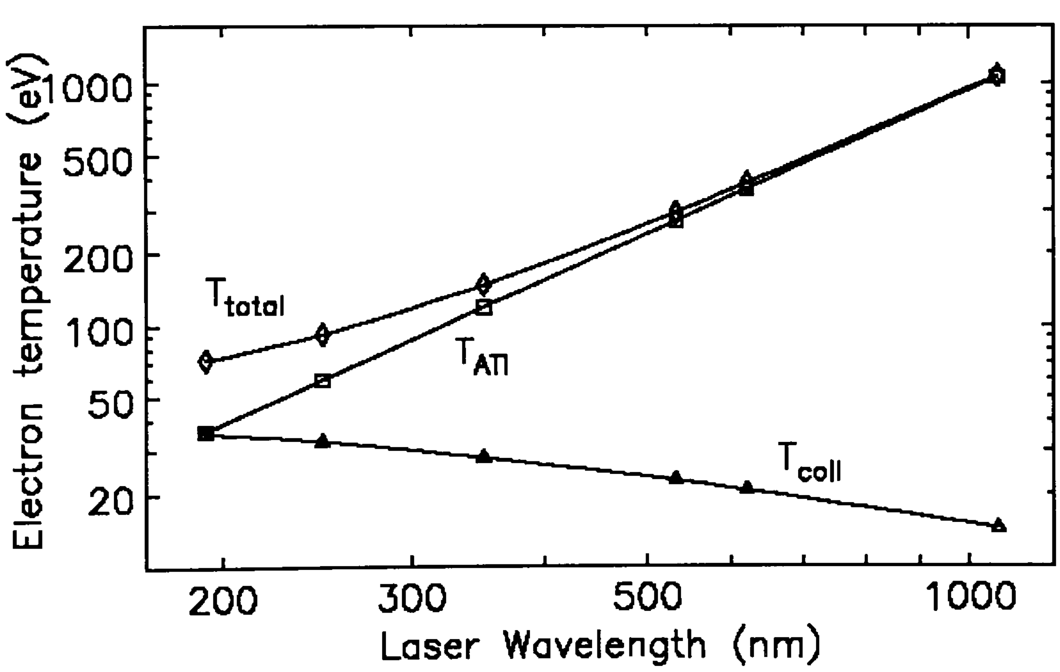

Figure 6.6: Plasma temperature as a function of laser wavelength, for a 100 fs, 2.5×10^{17} W/cm^2 laser pulse and a Ne atom density of 2.5×10^{18} cm^{-3}.

The ATI temperature increases almost exactly as λ_0^2, proportional to the increase in the quiver energy. The collisional temperature decreases slowly with increasing laser wavelength. In the high-intensity limit, where $\nu_{ei} \propto \mathcal{E}_q^{-3/2}$, the collisional absorption rate would be expected to decrease as λ_0^{-1}. The proportionality here is closer to $\lambda_0^{-1/2}$, and this difference is probably caused by collisional heating near the ends of the laser pulse, where the high-intensity limit does not apply. Overall, the reduction in the ATI temperature at shorter wavelengths is more significant than the increase in the collisional temperature, and the total plasma temperature decreases.

6.4 Relevance to Recombination X-Ray Lasers

The results obtained from the propagation-ionization model for a Li-like Ne plasma can be summarized as follows:

- An intensity of $\sim 2.5 \times 10^{17}$ W/cm^2 is required to produce a plasma consisting of Ne^{8+} ions, independent of the density, and the use of a higher intensity simply raises the plasma temperature.
- The collisional temperature increases approximately linearly with the density. For a 100 fs, 248 nm laser pulse, a collisional temperature of $\lesssim 50$ eV can only be achieved by reducing the neon atom density below 4×10^{18} cm^{-3}.
- The ATI temperature is independent of the density. For a 100 fs, 248 nm laser pulse at the minimum intensity required to produce a Ne^{8+} plasma, the ATI temperature is approximately 60 eV.
- Shorter pulses and shorter laser wavelengths will reduce the total plasma temperature.

A number of additional points should be considered before drawing any conclusions from these results. In the calculation of collisional heating, the electron distribution was assumed to take the form of a background Maxwellian oscillating in the laser field. Modifications to the Maxwellian may have the effect of reducing the absorption rate, particularly around the intensity where the quiver velocity and the thermal velocity are approximately equal [42]. However, for the peak intensities considered here, the effect of this reduction is expected to be small.

The ATI energy was calculated without including space-charge effects. It has been suggested by Penetrante and Bardsley [162] in a recent study of field-ionized plasmas that the presence of space-charge forces can modify the electron motion in such a way as to significantly reduce the ATI energy. Space-charge effects must depend in some way on the focal spot size, but in this study the exact conditions required to observe the reduction in ATI energy were not clearly specified. It would be possible to introduce space-charge in a phenomenological way into the present model (by including a restoring force in the electron equation of motion, for example), but the only way to obtain a quantitative measure of the effect would be to repeat, perhaps more carefully, the earlier particle-in-cell simulations.

Stimulated Raman scattering is a potentially serious source of additional heating in field-ionized plasmas. The electron energy produced by this mechanism is strongly-dependent both on plasma density and on laser pulse length. For a 100 fs, 248 nm pulse and an electron density of 10^{20} cm^{-3}, Amendt *et al.* [159] have calculated that parametric heating increases the plasma temperature by only about 5 eV. However, this effect increases significantly for longer pulses and higher densities.

The proposed recombination x-ray laser scheme in Li-like Ne at 9.8 nm requires an electron density of $\gtrsim 10^{20}$ cm^{-3} and a plasma temperature of $\lesssim 50$ eV for large gain and high energy efficiency [159]. For a 100 fs, 248 nm laser pulse at an intensity of 2.5×10^{17} W/cm^2 and an electron density of 10^{20} cm^{-3}, the propagation-ionization model predicts a plasma temperature of 185 eV, of which approximately 60 eV is ATI energy and 125 eV is due to collisional heating. The gain in such a scheme is an extremely sensitive function of temperature, and unless some way is found to significantly reduce both the ATI and the collisional contributions, this result shows that the scheme is barely feasible.

Even if a transient-gain scheme is somewhat optimistic, it is possible that field-ionized plasmas could lead to improvements on x-ray laser schemes in the quasi-steady-state regime. One proposal, by Burnett and Enright [158], is to form a pre-ionized plasma with a relatively low-intensity pulse and to allow this plasma to expand and cool. This step minimizes the ATI energy of the electrons from the lower ionization stages. A small filament is then ionized to the required ionization stage by a high-intensity pulse. The ATI energy of the final electrons is quite large, but electron thermal conduction into the background plasma is expected to rapidly cool the highly-ionized filament before significant hydrodynamic motion can take place, resulting in rapid recombination. The predicted gain in such a system far exceeds that obtained to date in exploding fibres cooled by adiabatic expansion.

To obtain gain in the transient regime, Burnett and Enright have also suggested removing the final electrons using circularly-polarized rather than linearly-polarized light. In this case, the residual ATI energy would be extremely large, on the order of twice the quiver energy (10–20 keV for 1 μm light at $\sim 10^{18}$ W/cm^2). The equilibration time for such high-energy electrons is considerably longer than the laser pulse, and this would effectively decouple them from the low-temperature background population, at least on the time scale of the gain duration. The use of a longer laser wavelength would also reduce the collisional heating rate, but even so, the maximum gain would probably be limited by collisional heating to a relatively low value [158].

A crucial question for any recombination x-ray laser scheme based on field-induced ionization is whether a long filament of highly-ionized plasma can actually be produced. In the transient-gain regime, where the gain duration is on the order of 1 ps, a travelling-wave pump geometry is necessary. Transverse pumping with a moving line focus, which has been used previously in optically-pumped VUV lasers [163], is not practical because of the very low fraction of pump energy which would be absorbed in a gaseous target. For the case of a 100 fs, 248 nm laser pulse at an intensity of 2.5×10^{17} W/cm^2 and an electron density of 10^{20} cm^{-3}, only 4.6×10^{-5} of the pump energy is converted to ionization over a distance of 5 μm. To achieve high efficiency, a large fraction of the pump energy must be converted into ionization, and this can only be achieved using longitudinal pumping, in which the x-ray gain is along the same axis as the focused pump pulse. The length of ionized plasma, L, which would completely consume the energy in a laser pulse of intensity I and duration τ is approximately given by

$$L \simeq IZ\tau / n_e \mathcal{E}_{tot} \ , \tag{6.19}$$

where n_i is the ion density, and $\mathcal{E}_{tot}$ is the total energy required to strip to the desired ionization stage. For $I = 2.5 \times 10^{17}$ W/cm^2, $Z = 8$, $\tau = 100$ fs, $n_e = 10^{20}$ cm^{-3} and

$\mathcal{E}_{tot} = 953.7$ eV (appropriate to Ne^{8+}), this length is approximately 13 cm.

In their detailed proposal, Amendt *et al.* calculated an energy efficiency (x-ray laser energy to pump laser energy) of 10^{-6} for an electron density of 10^{20} cm^{-3}, a plasma temperature of 40 eV and a Gaussian focal spot radius of 30 μm. This spot radius corresponds to a confocal parameter of 6.5 cm. Focusing a high-intensity laser pulse through a rapidly ionizing medium over such a long distance is by no means a trivial task. Refraction and defocusing caused by the rapid ionization would tend to disrupt the propagation of a Gaussian beam over distances much shorter than the several centimetres required. It may be that a specially-tailored geometry, such as a plasma waveguide, is the solution to this problem. However, the spatial behaviour of an intense laser pulse propagating through a gas is currently poorly understood. A number of studies have been published recently concerning self-channelling of laser pulses and the formation of plasma waveguides [164, 165, 166, 167, 168], but considerably more work, both theoretical and experimental, is needed to resolve this issue.

Chapter 7

Conclusions and Suggestions for Further Work

In this thesis, a number of topics have been discussed concerning laser absorption in plasmas created by intense ($\gtrsim 10^{15}$ W/cm^2) femtosecond ($\lesssim 1$ ps) laser pulses.

The work in Chapter 2 and Chapter 3 dealt largely with absorption in solid-density plasmas. High-intensity modifications to collisional absorption were discussed in Chapter 2, including a detailed calculation of absorption due to the excitation of collective modes. This effect was found to be significant only in the combined case of a low degree of ionization, high electron temperature and ultrahigh laser intensity. Above the intensity for which the quiver velocity equals the thermal velocity, the collisional absorption rate decreases, and the static-profile reflectivity model in Chapter 3 showed how this nonlinearity would affect the reflectivity of a steep-profile solid-density plasma, such as that produced by an intense femtosecond laser pulse. The largest increase in reflectivity was found for s-polarized light and for a density profile scale length of $L/\lambda_0 \sim 1$. The nonlinearity has a lesser effect on the plasma reflectivity for p-polarized light or for a very short scale length, $L/\lambda_0 \ll 1$.

These results are particularly relevant to experiments on incoherent soft x-ray generation from laser-produced plasmas. The saturation of absorption at high intensities is potentially a serious problem, if intense femtosecond laser pulses are used in attempts to produce short-duration high-energy x-ray emission. The results presented here suggest that absorption at high intensities can be maximized by using p-polarized light at a nonzero angle of incidence and by using the shortest possible laser pulses to restrict the plasma expansion. It is quite likely that other nonlinear effects, for example, density-profile steepening, will also influence the high-intensity reflectivity. Published experimental data on the polarization, angular and pulse-length dependence of plasma reflectivity at intensities much above 10^{15} W/cm^2 is very limited. Special target geometries may also prove advantageous in the high-intensity regime, and Murnane *et al.* [169] have recently shown that a surface grating structure can lead to a considerable increase in absorption.

Optical-field-induced ionization was introduced in Chapter 4, and it was shown that this mechanism could dominate over conventional collisional ionization in a low-density plasma. The remainder of the thesis was devoted to effects in gaseous plasmas formed by field-induced ionization.

Chapter 5 outlined a propagation-ionization model which was used to predict spectral shifts and broadening in an intense femtosecond laser pulse propagating through a monatomic gas. The agreement with the published experimental results of Downer *et al.* was not particularly good, but problems associated with the focusing geometry make exact comparisons difficult. Spectral broadening caused by field-induced ionization may be useful in providing a broadband spectroscopic source, especially in the VUV. The broadening is also a sensitive probe of ionization rates in the plasma, and could be used to test various models for field-induced ionization. There is a considerable amount of work still to be done in this area, in particular, the relationship between field-induced and collisional ionization at high pressures, and the more general problem of intense pulse propagation in a rapidly-ionizing medium. Self-focusing, although fairly well understood in the long-pulse regime, appears to be of a somewhat different nature for femtosecond pulses. An extension of the propagation model into higher dimensions might help in the investigation of this unusual behaviour.

By far the most enticing of the possible uses for a field-ionized plasma is in a recombination x-ray laser. The feasibility of such a scheme, at least in the transient-gain regime, relies on being able to create a highly-ionized plasma with a very low residual temperature, such that the initial recombination rate is extremely rapid. In Chapter 6, the propagation-ionization model was used to estimate the final plasma temperature after the passage of an intense femtosecond laser pulse through an atmospheric-density gas. The residual temperature under a range of conditions was compared to that required by a recombination x-ray laser scheme in Li-like Ne proposed by Amendt *et al.* [159], and it was concluded that the operation of this scheme would be marginal at best. Other proposed schemes involving double-pulse pumping and quasi-steady-state gain may, however, still prove to be viable. It is virtually impossible to include all the major plasma heating effects (ATI, collisions, space-charge and parametric instabilities) in a single model, and this makes absolute quantitative predictions difficult. The model described here includes only ATI and collisional heating, and further investigation using a a particle-in-cell code might help to clarify the role of space charge, which Penetrante and Bardsley [162] claim has a dominant effect. In addition, a higher-dimensional propagation model is needed to determine whether it is possible to produce a highly-ionized but tightly-confined plasma column over a relatively long distance. Some initial experiments in this area are badly needed, both to give an indication of the achievable temperatures and to investigate the possible formation of plasma waveguide structures.

References

[1] T. P. Hughes, *Plasmas and Laser Light* (Adam Hilger, Bristol, 1975).

[2] J. J. Duderstadt and G. A. Moses, *Inertial Confinement Fusion* (Wiley-Interscience, New York, 1982).

[3] M. H. Key, *Lasers Generate Plasma Power*, Phys. World **4(8)**, 52–56 (1991).

[4] M. M. Murnane and R. W. Falcone, *High-Power Femtosecond Dye-Laser System*, J. Opt. Soc. Am. B **5**, 1573–1575 (1988).

[5] S. Szatmári and F. P. Schäfer, *Simplified Laser System for the Generation of 60 fs Pulses at 248 nm*, Opt. Commun. **68**, 196–202 (1988).

[6] S. Szatmári, G. Kühnle, J. Jasny, and F. P. Schäfer, *KrF Laser System with Corrected Pulse Front and Compressed Pulse Duration*, Appl. Phys. B **49**, 239–244 (1989).

[7] R. Fedosejevs, R. Ottmann, R. Sigel, G. Kühnle, S. Szatmári, and F. P. Schäfer, *Absorption of Subpicosecond Ultraviolet Laser Pulses in High-Density Plasma*, Appl. Phys. B **50**, 79–99 (1990).

[8] M. Watanabe, A. Endoh, N. Sarukura, and S. Watanabe, *Subpicosecond UV Pulse Generation for a Multiterawatt KrF Laser*, Appl. Phys. B **48**, 417–420 (1989).

[9] A. Endoh, M. Watanabe, N. Sarukura, and S. Watanabe, *Multiterawatt Subpicosecond KrF Laser*, Opt. Lett. **14**, 353–355 (1989).

[10] J. P. Roberts, A. J. Taylor, P. H. Y. Lee, and R. B. Gibson, *High-Irradiance 248-nm Laser System*, Opt. Lett. **13**, 734–736 (1988).

[11] J. P. Roberts, S. E. Harper, T. R. Gosnell, and A. J. Taylor, *Generation of 50-μJ Subpicosecond Pulses at 248 nm*, Opt. Commun. **83**, 231–234 (1991).

[12] W. Tighe, C. H. Nam, J. Robinson, and S. Suckewer, *High Power Picosecond Laser System at 248 nm*, Rev. Sci. Instrum. **59**, 2235–2240 (1988).

[13] C. H. Nam, W. Tighe, E. Valeo, and S. Suckewer, *The Effect of Prepulse on X-Ray Laser Development Using a Powerful Subpicosecond KrF* Laser*, Appl. Phys. B **50**, 275–285 (1990).

[14] D. Strickland and G. Mourou, *Compression of Amplified Chirped Optical Pulses*, Opt. Commun. **56**, 219–221 (1985).

[15] P. Maine, D. Strickland, P. Bado, M. Pessot, and G. Mourou, *Generation of Ultrahigh Peak Power Pulses by Chirped Pulse Amplification*, IEEE J. Quantum Electron. **24**, 398–403 (1988).

[16] F. G. Patterson, R. Gonzales, and M. D. Perry, *Compact 10-TW, 800-fs Nd:glass Laser*, Opt. Lett. **16**, 1107–1109 (1991).

[17] F. G. Patterson and M. D. Perry, *Design and Performance of a Multiterawatt, Subpicosecond Neodymium:glass Laser*, J. Opt. Soc. Am. **8**, 2384–2391 (1991).

[18] C. Sauteret, D. Husson, G. Thiell, S. Seznec, S. Gary, A. Migus, and G. Mourou, *Generation of 20-TW Pulses of Picosecond Duration using Chirped-Pulse Amplification in a Nd:glass Power Chain*, Opt. Lett. **16**, 238–240 (1991).

[19] K. Yamakawa, H. Shiraga, Y. Kato, and C. P. J. Barty, *Prepulse-Free 30-TW, 1-ps Nd:glass Laser*, Opt. Lett. **16**, 1593–1595 (1991).

[20] J. Squier, F. Salin, G. Mourou, and D. Harter, *100-fs Pulse Generation and Amplification in Ti:Al_2O_3*, Opt. Lett. **16**, 324–326 (1991).

[21] J. D. Kmetec, J. J. Macklin, and J. F. Young, *0.5-TW, 125-fs Ti:sapphire Laser*, Opt. Lett. **16**, 1001–1003 (1991).

[22] A. Sullivan, H. Hamster, H. C. Kapteyn, S. Gordon, W. White, H. Nathel, R. J. Blair, and R. W. Falcone, *Multiterawatt, 100-fs Laser*, Opt. Lett. **16**, 1406–1408 (1991).

[23] R. C. Elton, *X-Ray Lasers* (Academic, Boston, 1990).

[24] W. T. Silfvast and O. R. Wood II, *Photoionization Lasers Pumped by Broadband Soft-X-Ray Flux from Laser-Produced Plasmas*, J. Opt. Soc. Am. B **4**, 609–618 (1987).

[25] D. Matthews, M. Rosen, S. Brown, N. Ceglio, D. Eder, A. Hawryluk, C. Keane, R. London, B. MacGowan, S. Maxon, D. Nilson, J. Scofield, and J. Trebes, *X-Ray Laser Research at the Lawrence Livermore National Laboratory Nova Laser Facility*, J. Opt. Soc. Am. B **4**, 575–587 (1987).

[26] C. L. S. Lewis, R. Corbett, D. O'Neill, C. Regan, S. Saadat, C. Chenais-Popovics, T. Tomie, J. Edwards, G. P. Kiehn, R. Smith, O. Willi, A. Carillon, H. Guennou, P. Jaegle, G. Jamelot, A. Klisnick, A. Sureau, M. Grande, C. Hooker, M. H. Key, S. J. Rose, I. N. Ross, P. T. Rumsby, G. J. Pert, and S. A. Ramsden, *Status of Soft X-Ray Laser Research at the Rutherford-Appleton Laboratory*, Plasma Phys. **30**, 35–44 (1988).

[27] M. M. Murnane, H. C. Kapteyn, and R. W. Falcone, *Generation and Application of Ultrafast X-Ray Sources*, IEEE J. Quantum Electron. **25**, 2417–2422 (1989).

[28] J. H. Glownia, J. Misewich, and P. P. Sorokin, *Ultrafast Ultraviolet Pump-Probe Apparatus*, J. Opt. Soc. Am. B **3**, 1573–1579 (1986).

[29] N. H. Burnett and P. B. Corkum, *Cold-Plasma Production for Recombination Extreme-Ultraviolet Lasers by Optical-Field-Induced Ionization*, J. Opt. Soc. Am. B **6**, 1195–1199 (1989).

[30] W. L. Kruer, *The Physics of Laser Plasma Interactions* (Addison-Wesley, Redwood City, CA, 1988).

[31] M. B. Hooper, ed., *Laser-Plasma Interactions 4*, Proc. 35th Scottish Universities Summer School in Physics (SUSSP, Edinburgh, 1989); and earlier volumes in this series.

[32] S. C. Rae and K. Burnett, *Nonlinear Absorption of Intense Laser Light by Collective Plasma Excitations*, Phys. Fluids B **2**, 1015–1020 (1990).

[33] L. Spitzer Jr., *Physics of Fully Ionized Gases*, 2nd Edn. (Interscience, New York, 1962), Chap. 5.

[34] I. P. Shkarofsky, T. W. Johnston, and M. P. Bachynski, *The Particle Kinetics of Plasmas* (Addison-Wesley, Reading, MA, 1966), Chap. 7.

[35] Y. T. Lee and R. M. More, *An Electron Conductivity Model for Dense Plasmas*, Phys. Fluids **27**, 1273–1286 (1984).

[36] S. Rand, *Inverse Bremsstrahlung with High-Intensity Radiation Fields*, Phys. Rev. **136**, B231–237 (1965).

[37] V. P. Silin, *Nonlinear High-Frequency Plasma Conductivity*, Zh. Eksp. Teor. Fiz. **47**, 2254–2265 (1964) [Sov. Phys. JETP **20**, 1510–1516 (1965)].

[38] F. V. Bunkin and M. V. Fedorov, *Bremsstrahlung in a Strong Radiation Field*, Zh. Eksp. Teor. Fiz. **49**, 1215–1221 (1965) [Sov. Phys. JETP **22**, 844–847 (1966)].

[39] G. J. Pert, *Inverse Bremsstrahlung Absorption in Large Radiation Fields during Binary Collisions—Classical Theory*, J. Phys. A **5**, 506–515 (1972); *Inverse Bremsstrahlung Absorption in Large Radiation Fields during Binary Collisions—Born Approximation I. Elastic Collisions*, J. Phys. A **5**, 1221–1232 (1972); *Inverse Bremsstrahlung Absorption in Large Radiation Fields during Binary Collisions—the Classical Theory as an Asymptotic Limit of the Born Approximation*, J. Phys. B **8**, 3069–3077 (1975); *Inverse Bremsstrahlung Absorption in Large Radiation Fields during Binary Collisions—Classical Theory II. Integrated Rate Coefficients for Coulomb Collisions*, J. Phys. A **9**, 463–471 (1976); *Inverse Bremsstrahlung Absorption in Large Radiation Fields*

during Binary Collisions—Classical Theory II(b). Summed Rate Coefficients for Coulomb Collisions, J. Phys. A **9**, 1797–1800 (1976).

[40] L. Schlessinger and J. Wright, *Inverse-Bremsstrahlung Absorption Rate in an Intense Laser Field*, Phys. Rev. A **20**, 1934–1945 (1979).

[41] R. D. Jones and K. Lee, *Kinetic Theory, Transport, and Hydrodynamics of a High-Z Plasma in the Presence of an Intense Laser Field*, Phys. Fluids **25**, 2307–2323 (1982).

[42] A. B. Langdon, *Nonlinear Inverse Bremsstrahlung and Heated-Electron Distributions*, Phys. Rev. Lett. **44**, 575–579 (1980).

[43] P. Mulser, K. Niu, and R. C. Arnold, *Collision Frequency in Ion-Beam-Plasma Interaction Under Strong Drift Conditions*, Nucl. Instrum. Meth. **A278**, 89–92 (1989).

[44] S. Ichimaru, *Basic Principles of Plasma Physics: A Statistical Approach* (W. A. Benjamin, Reading, MA, 1973), Chap. 4.

[45] B. D. Fried and S. D. Conte, *The Plasma Dispersion Function* (Academic, New York, 1961).

[46] N. D. Mermin, *Lindhard Dielectric Function in the Relaxation-Time Approximation*, Phys. Rev. B **1**, 2362–2363 (1970).

[47] K. Utsumi and S. Ichimaru, *Dielectric Formulation of Strongly Coupled Electron Liquid at Metallic Densities: Longitudinal Response*, Phys. Rev. B **22**, 1522–1533 (1980).

[48] R. A. Cairns, *Plasma Physics* (Blackie, Glasgow, 1985), Chap. 3.

[49] W. H. Press, B. P. Flannery, S. A. Teukolsky, and W. T. Vetterling, *Numerical Recipes: The Art of Scientific Computing* (Cambridge University Press, 1986).

[50] S. Ichimaru, S. Mitake, S. Tanaka, and X.-Z. Yan, *Theory of Interparticle Correlations in Dense, High-Temperature Plasmas. I. General Formalism*, Phys. Rev. A **32**, 1768–1774 (1985).

[51] S. C. Rae and K. Burnett, *Reflectivity of Steep-Gradient Plasmas in Intense Subpicosecond Laser Pulses*, Phys. Rev. A **44**, 3835–3840 (1991).

[52] R. Jacobsson, *Light Reflection from Films of Continuously Varying Refractive Index*, in *Progress in Optics V*, E. Wolf, ed. (North-Holland, Amsterdam, 1966), pp. 249–286.

[53] M. Born and E. Wolf, *Principles of Optics*, 4th Edn. (Pergamon, Oxford, 1970).

[54] N. G. Denisov, *On a Singularity of the Field of an Electromagnetic Wave Propagated in an Inhomogeneous Plasma*, Zh. Eksp. Teor. Fiz. **31**, 609–619 (1956) [Sov. Phys. JETP **4**, 544–553 (1957)].

[55] V. L. Ginzburg, *The Propagation of Electromagnetic Waves in Plasmas* (Pergamon, Oxford, 1964), Chap. 4.

[56] K. Försterling and H.-O. Wüster, *(Über dir Entstehung von Oberwellen in der Ionosphäre (On the Generation of Higher Harmonics in the Ionosphere)*, J. Atmos. Terr. Phys. **2**, 22–31 (1951).

[57] J. M. Dawson, *Nonlinear Electron Oscillations in a Cold Plasma*, Phys. Rev. **113**, 383–387 (1959).

[58] T. P. Coffey, *Breaking of Large Amplitude Plasma Oscillations*, Phys. Fluids **14**, 1402–1406 (1971).

[59] P. Koch and J. Albritton, *Electron and Ion Heating Through Resonant Plasma Oscillations*, Phys. Rev. Lett. **32**, 1420–1423 (1974).

[60] D. W. Forslund, J. M. Kindel, K. Lee, E. L. Lindman, and R. L. Morse, *Theory and Simulation of Resonant Absorption in a Hot Plasma*, Phys. Rev. A **11**, 679–683 (1975).

[61] K. G. Estabrook, E. J. Valeo, and W. L. Kruer, *Two-Dimensional Relativistic Simulations of Resonance Absorption*, Phys. Fluids **18**, 1151–1159 (1975).

[62] J. S. DeGroot and J. E. Tull, *Heated Electron Distributions from Resonant Absorption*, Phys. Fluids **18**, 672–678 (1975).

[63] D. W. Forslund, J. M. Kindel, and K. Lee, *Theory of Hot-Electron Spectra at High Laser Intensity*, Phys. Rev. Lett. **39**, 284–288 (1977).

[64] K. Estabrook and W. L. Kruer, *Properties of Resonantly Heated Electron Distributions*, Phys. Rev. Lett. **40**, 42–45 (1978).

[65] J. R. Albritton and A. B. Langdon, *Profile Modification and Hot-Electron Temperature from Resonant Absorption at Modest Intensity*, Phys. Rev. Lett. **45**, 1794–1797 (1980).

[66] J. P. Freidberg, R. W. Mitchell, R. L. Morse, and L. I. Rudsinski, *Resonant Absorption of Laser Light by Plasma Targets*, Phys. Rev. Lett. **28**, 795–799 (1972).

[67] J. Lekner, *Theory of Reflection of Electromagnetic and Particle Waves* (Martinus Nijhoff, Dordrecht, 1987), Chap. 2.

[68] D. W. Forslund, J. M. Kindel, K. Lee, and E. L. Lindman, *Absorption of Laser Light on Self-Consistent Plasma Density Profiles*, Phys. Rev. Lett. **36**, 35–38 (1976).

[69] H. M. Milchberg, R. R. Freeman, S. C. Davey, and R. M. More, *Resistivity of a Simple Metal from Room Temperature to* 10^6 *K*, Phys. Rev. Lett. **61**, 2364–2367 (1988).

[70] H. M. Milchberg and R. R. Freeman, *Light Absorption in Ultrashort Scale Length Plasmas*, J. Opt. Soc. Am. B **6**, 1351–1355 (1989).

[71] J. C. Kieffer, P. Audebert, M. Chaker, J. P. Matte, H. Pépin, T. W. Johnston, P. Maine, D. Meyerhofer, J. Delettrez, D. Strickland, P. Bado, and G. Mourou, *Short-Pulse Laser Absorption in Very Steep Plasma Density Gradients*, Phys. Rev. Lett. **62**, 760–763 (1989).

[72] J.-C. Kieffer, J.-P. Matte, S. Bélair, M. Chaker, P. Audebert, H. Pépin, P. Maine, D. Strickland, P. Bado, and G. Mourou, *Absorption of an Ultrashort Laser Pulse in Very Steep Plasma Density Gradients*, IEEE J. Quantum Electron. **25**, 2640–2647 (1989).

[73] R. Fedosejevs, R. Ottmann, R. Sigel, G. Kühnle, S. Szatmari, and F. P. Schäfer, *Absorption of Femtosecond Laser Pulses in High-Density Plasma*, Phys. Rev. Lett. **64**, 1250–1253 (1990).

[74] N. B. Delone and V. P. Krainov, *Atoms in Strong Light Fields* (Springer, Berlin, 1985).

[75] S. L. Chin and P. Lambropoulos, eds., *Multiphoton Ionization of Atoms* (Academic, New York, 1984).

[76] F. H. M. Faisal, *Theory of Multiphoton Processes* (Plenum, New York, 1987).

[77] P. Lambropoulos, *Mechanisms for Multiple Ionization of Atoms by Strong Pulsed Lasers*, Phys. Rev. Lett. **55**, 2141–2144 (1985); *Multiple Excitation and Ionization of Atoms by Strong Pulsed Lasers*, Comments At. Mol. Phys. **20**, 199–216 (1987); P. Lambropoulos and X. Tang, *Multiple Excitation and Ionization of Atoms by Strong Lasers*, J. Opt. Soc. Am. B **4**, 821–832 (1987).

[78] A. l'Huillier, L. A. Lompre, G. Mainfray, and C. Manus, *Multiply Charged Ions Induced by Multiphoton Absorption in Rare Gases at 0.53 μm*, Phys. Rev. A **27**, 2503–2512 (1983).

[79] E. Karule, *Multiphoton Ionization of Atomic Hydrogen*, in *Multiphoton Processes*, J. H. Eberly and P. Lambropoulos, eds. (Wiley, New York, 1978).

[80] M. D. Perry, A. Szoke, O. L. Landen, and E. M. Campbell, *Nonresonant Multiphoton Ionization of Noble Gases: Theory and Experiment*, Phys. Rev. Lett. **60**, 1270–1273 (1988); M. D. Perry, O. L. Landen, A. Szöke, and E. M. Campbell, *Multiphoton Ionization of the Noble Gases by an Intense 10^{14}-W/cm^2 Dye Laser*, Phys. Rev. A **37**, 747–760 (1988).

[81] O. L. Landen, M. D. Perry, and E. M. Campbell, *Resonant Multiphoton Ionization of Krypton by Intense uv Laser Radiation*, Phys. Rev. Lett. **59**, 2258–2261 (1987).

[82] M. D. Perry, A. Szoke, and K. C. Kulander, *Resonantly Enhanced Above-Threshold Ionization of Helium*, Phys. Rev. Lett. **63**, 1058–1061 (1989).

[83] L. V. Keldysh, *Ionization in the Field of a Strong Electromagnetic Wave*, Zh. Eksp. Teor. Fiz. **47**, 1945–1957 (1964) [Sov. Phys. JETP **20**, 1307–1314 (1965)].

[84] A. Maquet, S.-I Chu, and W. P. Reinhardt, *Stark Ionization in dc and ac Fields: An L^2 Complex-Coordinate Approach*, Phys. Rev. A **27**, 2946–2970 (1983); S.-I Chu and J. Cooper, *Threshold Shift and Above-Threshold Multiphoton Ionization of Atomic Hydrogen in Intense Laser Fields*, Phys. Rev. A **32**, 2769–2775 (1985); S.-I Chu and R. Y. Yin, *Classical and Quantal Nonperturbative Treatments of Multiphoton and Above-Threshold Ionization*, J. Opt. Soc. Am. B **4**, 720–725 (1987).

[85] R. M. Potvliege and R. Shakeshaft, *Multiphoton Processes in an Intense Laser Field: Harmonic Generation and Total Ionization Rates for Atomic Hydrogen*, Phys. Rev. A **40**, 3061–3079 (1989); *Multiphoton Processes in an Intense Laser Field. II. Partial Rates and Angular Distributions for Ionization of Atomic Hydrogen at 532 nm*, Phys. Rev. A **41**, 1609–1619 (1990); M. Dörr, R. M. Potvliege, and R. Shakeshaft, *Multiphoton Processes in an Intense Laser Field. III. Resonant Ionization of Hydrogen by Subpicosecond Pulses*, Phys. Rev. A **41**, 558–561 (1990).

[86] K. C. Kulander, *Time-Dependent Hartree-Fock Theory of Multiphoton Ionization: Helium*, Phys. Rev. A **36**, 2726–2738 (1987); *Time-Dependent Theory of Multiphoton Ionization of Xenon*, Phys. Rev. A **38**, 778–787 (1988).

[87] K. J. LaGattuta, *Laser Effects in Photoionization: Numerical Solution for a One-Dimensional δ Potential*, Phys. Rev. A **40**, 683–695 (1989); *Laser Effects in Photoionization. II. Numerical Solution of Coupled Equations for Atomic Hydrogen*, Phys. Rev. A **41**, 5110–5116 (1990); *Laser Effects in Photoionization: Numerical Solution of Coupled Equations for a Three-Dimensional Coulomb Potential*, J. Opt. Soc. Am. B **7**, 639–646 (1990).

[88] K. C. Kulander, *Multiphoton Ionization of Hydrogen: A Time-Dependent Theory*, Phys. Rev. A **35**, 445–447 (1987).

[89] J. Javanainen, J. H. Eberly, and Q. Su, *Numerical Simulations of Multiphoton Ionization and Above-Threshold Electron Spectra*, Phys. Rev. A **38**, 3430–3446 (1988).

[90] V. C. Reed and K. Burnett, *Ionization of Atoms in Intense Laser Pulses using the Kramers-Henneberger Transformation*, Phys. Rev. A **42**, 3152–3155 (1990).

[91] L. D. Landau and E. M. Lifshitz, *Quantum Mechanics*, Vol. 3 of *Course of Theoretical Physics* (Pergamon, London, 1958), p. 257.

[92] L. A. Collins and A. L. Merts, *Model Calculations for an Atom Interacting with an Intense, Time-Dependent Electric Field*, Phys. Rev. A **37**, 2415–2431 (1988).

[93] J. Javanainen and J. H. Eberly, *Comparison of Keldysh Models with Numerical Experiments on Above-Threshold Ionization*, Phys. Rev. A **39**, 458–461 (1989).

[94] P. W. Milonni and J. R. Ackerhalt, *Keldysh Approximation, A^2, and Strong-Field Ionization*, Phys. Rev. A **39**, 1139–1148 (1989).

[95] F. H. M. Faisal, *Multiple Absorption of Laser Photons by Atoms*, J. Phys. B **6**, L89–92 (1973).

[96] H. R. Reiss, *Effect of an Intense Electromagnetic Field on a Weakly Bound System*, Phys. Rev. A **22**, 1786–1813 (1980); *Complete Keldysh Theory and its Limiting Cases*, Phys. Rev. A **42**, 1476–1486 (1990).

[97] W. Becker, R. R. Schlicher, and M. O. Scully, *Final-State Effects in Above-Threshold Ionisation*, J. Phys. B **19**, L785–792 (1986).

[98] A. M. Perelomov, V. S. Popov, and M. V. Terent'ev, *Ionization of Atoms in an Alternating Electric Field*, Zh. Eksp. Teor. Fiz. **50**, 1393–1409 (1966) [Sov. Phys. JETP **23**, 924–934 (1966)].

[99] M. V. Ammosov, N. B. Delone, and V. P. Kraĭnov, *Tunnel Ionization of Complex Atoms and of Atomic Ions in an Alternating Electromagnetic Field*, Zh. Eksp. Teor. Fiz. **91**, 2008–2013 (1986) [Sov. Phys. JETP **64**, 1191–1194 (1987)].

[100] N. B. Delone and V. P. Krainov, *Energy and Angular Electron Spectra for the Tunnel Ionization of Atoms by Strong Low-Frequency Radiation*, J. Opt. Soc. Am. B **8**, 1207–1211 (1991).

[101] S. Augst, D. Strickland, D. D. Meyerhofer, S. L. Chin, and J. H. Eberly, *Tunneling Ionization of Noble Gases in a High-Intensity Laser Field*, Phys. Rev. Lett. **63**, 2212–2215 (1989); errata **66**, 1247 (1991).

[102] S. Augst, D. D. Meyerhofer, D. Strickland, and S. L. Chin, *Laser Ionization of Noble Gases by Coulomb-Barrier Suppression*, J. Opt. Soc. Am. B **8**, 858–867 (1991).

[103] R. K. Peterkop, *Theory of Ionization of Atoms by Electron Impact* (Colorado Associated University Press, Boulder, 1977).

[104] M. Gryziński, *Classical Theory of Atomic Collisions. I. Theory of Inelastic Collisions*, Phys. Rev. **138**, A336–358 (1965).

[105] D. Colombant and G. F. Tonon, *X-Ray Emission in Laser-Produced Plasmas*, J. Appl. Phys. **44**, 3524–3537 (1973); G. Tonon and M. Rabeau, *Plasma Characteristics with TEA-CO_2 Laser and Wavelength Scaling Law*, Plasma Phys. **15**, 871–882 (1973).

[106] W. M. Wood, G. Focht, and M. C. Downer, *Tight Focusing and Blue Shifting of Millijoule Femtosecond Pulses from a Conical Axicon Amplifier*, Opt. Lett. **13**, 984–986 (1988).

[107] R. R. Alfano, ed., *The Supercontinuum Laser Source* (Springer, Berlin, 1989).

[108] R. R. Alfano and S. L. Shapiro, *Observation of Self-Phase Modulation and Small-Scale Filaments in Crystals and Glasses*, Phys. Rev. Lett. **24**, 592–594 (1970); *Emission in the Region 4000 to 7000 Å via Four-Photon Coupling in Glass*, Phys. Rev. Lett. **24**, 584–587 (1970); *Direct Distortion of Electronic Clouds of Rare-Gas Atoms in Intense Electric Fields*, Phys. Rev. Lett. **24**, 1217–1220 (1970).

[109] R. L. Fork, C. V. Shank, C. Hirlimann, and R. Yen, *Femtosecond White-Light Continuum Pulses*, Opt. Lett. **8**, 1–3 (1983).

[110] G. Yang and Y. R. Shen, *Spectral Broadening of Ultrashort Pulses in a Nonlinear Medium*, Opt. Lett. **9**, 510–512 (1984).

[111] J. T. Manassah, M. A. Mustafa, R. R. Alfano, and P. P. Ho, *Spectral Extent and Pulse Shape of the Supercontinuum for Ultrashort Laser Pulse*, IEEE J. Quantum Electron. **22**, 197–204 (1986).

[112] R. H. Stolen and C. Lin, *Self-Phase-Modulation in Silica Optical Fibres*, Phys. Rev. A **17**, 1448–1453 (1978).

[113] A. Penzkofer, A. Laubereau, and W. Kaiser, *Stimulated Short-Wave Radiation due to Single-Frequency Resonances of* $\chi^{(3)}$, Phys. Rev. Lett. **31**, 863–866 (1973); A. Penzkofer, *Parametrically Generated Spectra and Optical Breakdown in H_2O and NaCl*, Opt. Commun. **11**, 265–269 (1974); A. Penzkofer, A. Seilmeier, and W. Kaiser, *Parametric Four-Photon Generation of Picosecond Light at High Conversion Efficiency*, Opt. Commun. **14**, 363–367 (1975).

[114] W. L. Smith, P. Liu, and N. Bloembergen, *Superbroadening in H_2O and D_2O by Self-Focused Picosecond Pulses from a YAlG:Nd Laser*, Phys. Rev. A **15** 2396–2403 (1977).

[115] P. B. Corkum, C. Rolland, and T. Srinivasan-Rao, *Supercontinuum Generation in Gases*, Phys. Rev. Lett. **57**, 2268–2271 (1986).

[116] P. B. Corkum and C. Rolland, *Femtosecond Continua Produced in Gases*, IEEE J. Quantum Electron. **25**, 2634–2639 (1989).

[117] T. R. Gosnell, A. J. Taylor, and D. P. Greene, *Supercontinuum Generation at 248 nm using High-Pressure Gases*, Opt. Lett. **15**, 130–132 (1990)

[118] D. Strickland and P. B. Corkum, *Resistance of Short Pulses to Self-Focusing*, in *Short-Wavelength Coherent Radiation: Generation and Applications*, Technical Digest Series (Optical Society of America, Washington DC, 1991), pp. 36–37.

[119] M. V. Fedorov, M. Yu. Ivanov, and P. B. Lerner, *Interaction of Atoms with Supershort Laser Pulses and the Generation of the Supercontinuum*, J. Phys. B **23**, 2505–2520 (1990).

[120] N. Bloembergen, *The Influence of Electron Plasma Formation on Superbroadening in Light Filaments*, Opt. Commun. **8**, 285–288 (1973).

[121] E. Yablonovitch, *Spectral Broadening in the Light Transmitted through a Rapidly Growing Plasma*, Phys. Rev. Lett. **31**, 877-879 (1973).

[122] E. Yablonovitch, *Self-Phase Modulation of Light in a Laser-Breakdown Plasma*, Phys. Rev. Lett. **32**, 1101–1104 (1974).

[123] E. Yablonovitch, *Self-Phase Modulation and Short-Pulse Generation from Laser-Breakdown Plasmas*, Phys. Rev. A **10**, 1888–1895 (1974).

[124] M. C. Downer, G. Focht, D. H. Reitze, W. M. Wood and T. R. Zhang, *Blue Shifting of Intense Femtosecond Pulses in Gas Breakdown and Solid State Plasmas*, in *Ultrafast Phenomena VI*, T. Yajima, K. Yoshihara, C. B. Harris, and S. Shionoya, eds. (Springer, Berlin, 1988), pp. 128–131.

[125] M. C. Downer, J. I. Trisnadi, W. M. Wood, and W. C. Banyai, *Spectral Shifting of Femtosecond Pulses in Atmospheric Density Plasmas*, in *Spectral Line Shapes VI*, L. Frommhold and J. W. Keto, eds. (American Institute of Physics, New York, 1990), pp. 107–126.

[126] M. C. Downer, W. M. Wood, and J. I. Trisnadi, *Comment on "Energy Conservation in the Picosecond and Subpicosecond Photoelectric Effect"*, Phys. Rev. Lett. **65**, 2832 (1990).

[127] M. C. Downer, W. C. Banyai, W. M. Wood, D. C. Anacker, and J. L. Erskine, *Interaction of Super-Intense Light Fields with Atoms and Surfaces*, Proc. SPIE **1209**, 166–174 (1990).

[128] W. M. Wood and M. C. Downer, *Spectral Blueshifts of Femtosecond Pulses in Atmospheric Density Kr and Xe Plasmas*, in *Short Wavelength Coherent Radiation: Generation and Applications*, Technical Digest Series (Optical Society of America, Washington DC, 1991), pp. 41–43.

[129] R. D. Cowan, *The Theory of Atomic Structure and Spectra* (University of California Press, Berkeley, 1981), pp. 12–15.

[130] G. D. Smith, *Numerical Solution of Partial Differential Equations: Finite Difference Methods*, 3rd Edn. (Clarendon Press, Oxford, 1985).

[131] H. Tawara and T. Kato, *Total and Partial Cross Sections of Atoms and Ions by Electron Impact*, At. Data Nucl. Data Tables **36**, 167–353 (1987).

[132] O. Svelto, *Principles of Lasers*, 3rd Edn. (Plenum, New York, 1989), Chap. 4.

[133] D. L. Matthews, P. L. Hagelstein, M. D. Rosen, M. J. Eckart, N. M. Ceglio, A. U. Hazi, H. Medecki, B. J. MacGowan, J. E. Trebes, B. L. Whitten, E. M. Campbell, C. W. Hatcher, A. M. Hawryluk, R. L. Kauffman, L. D. Pleasance, G. Ramback, J. H. Scofield, G. Stone, and T. A. Weaver, *Demonstration of a Soft X-Ray Amplifier*, Phys. Rev. Lett. **54**, 110–113 (1985).

[134] B. J. MacGowan, M. D. Rosen, M. J. Eckart, P. L. Hagelstein, D. L. Matthews, D. G. Nilson, T. W. Phillips, J. H. Scofield, G. Shimkaveg, J. E. Trebes, R. S. Walling, B. L. Whitten, and J. G. Woodworth, *Observation of Soft X-Ray Amplification in Neonlike Molybdenum*, J. Appl. Phys. **61**, 5243–5248 (1987).

[135] B. J. MacGowan, S. Maxon, P. L. Hagelstein, C. J. Keane, R. A. London, D. L. Matthews, M. D. Rosen, J. H. Scofield, and D. A. Whelan, *Demonstration of Soft-X-Ray Amplification in Nickel-like Ions*, Phys. Rev. Lett. **59**, 2157–2160 (1987).

[136] B. J. MacGowan, S. Maxon, L. B. Da Silva, D. J. Fields, C. J. Keane, D. L. Matthews, A. L. Osterheld, J. H. Scofield, G. Shimkaveg, and G. F. Stone, *Demonstration of X-Ray Amplifiers near the Carbon K Edge*, Phys. Rev. Lett. **65**, 420–423 (1990).

[137] M. D. Rosen, P. L. Hagelstein, D. L. Matthews, E. M. Campbell, A. U. Hazi, B. L. Whitten, B. MacGowan, R. E. Turner, R. W. Lee, G. Charatis, G. E. Busch, C. L. Shepard, and P. D. Rockett, *Exploding-Foil Technique for Achieving a Soft X-Ray Laser*, Phys. Rev. Lett. **54**, 106–109 (1985).

[138] T. N. Lee, E. A. McLean, and R. C. Elton, *Soft X-Ray Lasing in Neonlike Germanium and Copper Plasmas*, Phys. Rev. Lett. **59**, 1185–1188 (1987).

[139] D. M. O'Neill, C. L. S. Lewis, D. Neely, J. Uhomoibhi, M. H. Key, A. MacPhee, G. J. Tallents, S. A. Ramsden, A. Rogoyski, E. A. McLean, and G. J. Pert, *Characterisation of Soft X-Ray Amplification Observed in Ne-like Germanium*, Opt. Commun. **75**, 406–412 (1990).

[140] L. I. Gudzenko and L. A. Shelepin, *Negative Absorption in a Nonequilibrium Hydrogen Plasma*, Zh. Eksp. Teor. Fiz. **45**, 1445–1449 (1963) [Sov. Phys. JETP **18**, 998–1000 (1964)]; *Radiation Enhancement in a Recombining Plasma*, Dokl. Akad. Nauk SSSR **160**, 1296–1299 (1965) [Sov. Phys. Dokl. **10**, 147–149 (1965)].

[141] J. Peyraud and N. Peyraud, *Population Inversion in Laser Plasmas*, J. Appl. Phys. **43**, 2993–2996 (1972).

[142] W. W. Jones and A. W. Ali, *Theory of Short-Wavelength Lasers from Recombining Plasmas*, Appl. Phys. Lett. **26**, 450–451 (1975); *Recombination Lasers from Cooled Hydrogenlike Plasmas*, J. Appl. Phys. **48**, 3118–3119 (1977); *On the Population Inversion in Hydrogen-like Plasmas*, J. Phys. B **11**, L87–91 (1978).

[143] J. M. Green and W. T. Silfvast, *Population Inversions with Respect to the Ground Level of an Ion or Atom by the Rapid Cooling of a Plasma*, Appl. Phys. Lett. **28**, 253–255 (1976).

[144] G. J. Pert, *Model Calculations of XUV Gain in Rapidly Expanding Cylindrical Plasmas*, J. Phys. B **9**, 3301–3315 (1976); *Model Calculations of XUV Gain in Rapidly Expanding Cylindrical Plasmas II*, J. Phys. B **12**, 2067–2079 (1979); *Recombination Lasers in the XUV Spectral Region*, Plasma Phys. **27**, 1427–1438 (1985); *Model Calculations of Extreme-Ultraviolet Gain in Rapidly Expanding Cylindrical Carbon Plasmas*, J. Opt. Soc. Am. B **4**, 602–608 (1987).

[145] G. J. Tallents, *Population Inversions for Soft X-Ray Transitions Computed for Rapidly Cooling Plasmas*, J. Phys. B **10**, 1769–1780 (1977).

[146] S. Suckewer and H. Fishman, *Conditions for Soft X-Ray Lasing Action in a Confined Plasma Column*, J. Appl. Phys, **51**, 1922–1931 (1980).

[147] D. L. Matthews, E. M. Campbell, K. Estabrook, W. Hatcher, R. L. Kauffman, R. W. Lee, and C. L. Wang, *Observation of Enhanced Emission of the O VIII Hα Line in a Recombining Laser-Produced Plasma*, Appl. Phys. Lett. **45**, 226–228 (1984).

[148] P. Jaeglé, G. Jamelot, A. Carillon, A. Klisnick, A. Sureau, and H. Guennou, *Soft-X-Ray Amplification by Lithiumlike Ions in Recombining Hot Plasmas*, J. Opt. Soc. Am. B **4**, 563–574 (1987).

[149] S. Suckewer, C. H. Skinner, H. Milchberg, C. Keane, and D. Voorhees, *Amplification of Stimulated Soft-X-Ray Emission in a Confined Plasma Column*, Phys. Rev. Lett. **55**, 1753–1756 (1985).

[150] C. Chenais-Popovics, R. Corbett, C. J. Hooker, M. H. Key, G. P. Kiehn, C. L. S. Lewis, G. J. Pert, C. Regan, S. J. Rose, S. Sadaat, R. Smith, T. Tomie, and O. Willi, *Laser Amplification at 18.2 nm in Recombining Plasma from a Laser-Irradiated Carbon Fiber*, Phys. Rev. Lett. **59**, 2161–2164 (1987).

[151] M. Grande, M. H. Key, G. Kiehn, C. L. S. Lewis, G. J. Pert, S. A. Ramsden, C. Regan, S. J. Rose, R. Smith, T. Tomie, and O. Willi, *Measurement and Detailed Analysis of Single Pass Gain at 81 Å in a Recombining Laser Produced Fluorine Plasma*, Opt. Commun. **74**, 309–312 (1990).

[152] Y. Kato, E. Miura, T. Tachi, H. Shiraga, H, Nishimura, H. Daido, M. Yamanaka, T. Jitsuno, M. Tagaki, P. R. Herman, H. Takabe, S. Nakai, C. Yamanaka, M. H. Key, G. J. Tallents, S. J. Rose, and P. T. Rumsby, *Observation of Gain at 54.2 Å on Balmer-Alpha Transition of Hydrogenic Sodium*, Appl. Phys. B **50**, 247–256 (1990).

[153] A. Carillon, M. J. Edwards, M. Grande, M. J. de C. Henshaw, P. Jaegle, G. Jamelot, M. H. Key, G. P. Kiehn, A. Klisnick, C. L. S. Lewis, D. O'Neill, G. J. Pert, S. A. Ramsden, C. M. E. Regan, S. J. Rose, R. Smith, and O. Willi, *Soft X-Ray Amplification in Aluminium Recombining Plasma Produced from a Thin Coated Fibre*, J. Phys B **23**, 147–163 (1990).

[154] G. P. Kiehn, J. Edwards, R. A. Smith, O. Willi, C. L. S. Lewis, D. O'Neill, C. Regan, G. Pert, S. Ramsden, M. Grande, M. H, Key, S. J. Rose, A. Carillon,

H. Guennou, P. Jaegle, G. Jamelot, A. Klisnick, and A. Sureau, *X-Ray Laser Research at the Rutherford Laboratory*, Proc. SPIE **831**, 270–274 (1987).

[155] R. A. Smith, V. Barrow, J. Edwards, G. Kiehn, and O. Willi, *High Density Plasmas for Recombination X-Ray Lasers*, Appl. Phys. B **50**, 187–192 (1990).

[156] G. J. Pert and S. J. Rose, *Detailed Simulation of Recombination XUV Laser Experiments*, Appl. Phys. B **50**, 307–311 (1990).

[157] M. Steyer, F. P. Schäfer, S. Szatmári, and G. Kühnle, *Feasibility of a Laboratory X-Ray Laser Pumped by Ultrashort UV Laser Pulses*, Appl. Phys. B **50**, 265–273 (1990).

[158] N. H. Burnett and G. D. Enright, *Population Inversion in the Recombination of Optically-Ionized Plasmas*, IEEE J. Quantum Electron. **26**, 1797–1808 (1990).

[159] P. Amendt, D. C. Eder, and S. C. Wilks, *X-Ray Lasing by Optical-Field-Induced Ionization*, Phys. Rev. Lett. **66**, 2589–2592 (1991).

[160] P. Kruit, J. Kimman, H. G. Muller, and M. J. van der Wiel, *Electron Spectra from Multiphoton Ionization of Xenon at 1064, 532, and 355 nm*, Phys. Rev. A **28**, 248–255 (1983).

[161] P. B. Corkum, N. H. Burnett, and F. Brunel, *Above-Threshold Ionization in the Long-Wavelength Limit*, Phys. Rev. Lett. **62**, 1259–1262 (1989).

[162] B. M. Penetrante and J. N. Bardsley, *Residual Energy in Plasmas Produced by Intense Subpicosecond Lasers*, Phys. Rev. A **43**, 3100–3113 (1991).

[163] C. P. J. Barty, D. A. King, G. Y. Yin, K. H. Hahn, J. E. Field, J. F. Young, and S. E. Harris, *12.8-eV Laser in Neutral Cesium*, Phys. Rev. Lett. **61**, 2201–2204 (1988).

[164] G. Z. Sun, E. Ott, Y. C. Lee, and P. Guzdar, *Self-Focusing of Short Intense Pulses in Plasmas*, Phys. Fluids **30**, 526–532 (1987).

[165] W. B. Mori, C. Joshi, J. M. Dawson, D. W. Forslund, and J. M. Kindel, *Evolution of Self-Focusing of Intense Electromagnetic Waves in Plasma*, Phys. Rev. Lett. **60**, 1298–1301 (1988).

[166] J. C. Solem, T. S. Luk, K. Boyer, and C. K. Rhodes, *Prospects for X-Ray Amplification with Charge-Displacement Self-Channeling*, IEEE J. Quantum Electron. **25**, 2423–2430 (1989).

[167] T. Kurki-Suonio, P. J. Morrison, and T. Tajima, *Self-Focusing of an Optical Beam in a Plasma*, Phys. Rev. A **40**, 3230–3239 (1989).

[168] P. Sprangle, E. Esarey, and A. Ting, *Nonlinear Interaction of Intense Laser Pulses in Plasmas*, Phys. Rev. A **41**, 4463–4469 (1990).

[169] M. Murnane, H. Kapteyn, J. Bokor, W. Mansfield, R. Gnall, E. Glytsis, T. Gaylord, and R. Falcone, *Efficient Coupling of High-Intensity Sub-Picosecond Laser Pulses into Solid Grating Targets*, in *Short-Wavelength Coherent Radiation: Generation and Applications*, Technical Digest Series (Optical Society of America, Washington DC, 1991), pp. 116–117.